

Phase controlled synthesis and characterization of noble metal nanomaterials

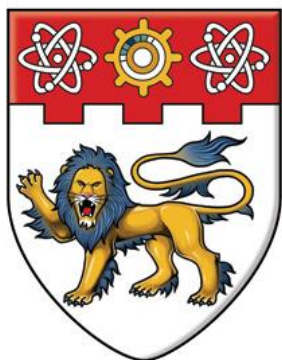
Fan, Zhanxi

2015

Fan, Z. (2015). Phase controlled synthesis and characterization of noble metal nanomaterials. Doctoral thesis, Nanyang Technological University, Singapore.

<https://hdl.handle.net/10356/65655>

<https://doi.org/10.32657/10356/65655>



NANYANG
TECHNOLOGICAL
UNIVERSITY

**PHASE CONTROLLED SYNTHESIS AND
CHARACTERIZATION OF NOBLE METAL
NANOMATERIALS**

FAN ZHANXI

SCHOOL OF MATERIALS SCIENCE AND ENGINEERING

2015

**PHASE CONTROLLED SYNTHESIS AND
CHARACTERIZATION OF NOBLE METAL NANOMATERIALS**
FAN ZHANXI

2015

**PHASE CONTROLLED SYNTHESIS AND
CHARACTERIZATION OF NOBLE METAL
NANOMATERIALS**

FAN ZHANXI

SCHOOL OF MATERIALS SCIENCE AND ENGINEERING

A thesis submitted to the Nanyang Technological University in
partial fulfillment of the requirement for the degree of

Doctor of Philosophy

2015

ACKNOWLEDGEMENT

First and foremost, I would like to express my heartfelt appreciation and thanks to my supervisor, Prof. Zhang Hua, for his brilliant guidance, insightful advices, great encouragement and continuous support during the past four years of my PhD study.

I also want to deeply thank Dr. Huang Xiao, Dr. Bosman Michel, Prof. Yang Peidong, Assoc. Prof. Han Yu, Asst. Prof. Li Shuzhou, Assoc. Prof. Gan Chee Lip, Dr. Liu Qing, Dr. Zhu Yihan, Dr. Shi Wenxiong, Dr. Wu Lin, Dr. Yu Yi, Dr. Zeng Zhiyuan, Dr. Qi Xiaoying, Dr. Hong Xun, Dr. Li Bing, Mr. Huang Ding and Mr. Wang Qingxiao for their self-giving help and meaningful suggestions on my research.

I would like to thank all my group members and friends: Dr. Yin Zongyou, Dr. Lu Gang, Dr. Li Hai, Dr. Wu Xuejun, Dr. He Qiyuan, Dr. Du Yaping, Dr. Liu Juqing, Dr. Luo Zhimin, Dr. Cao Xiehong, Dr. Zheng Bing, Ms. Wu Jumiati, Mr. Tan Chaoliang, Mr. Chen Junze, Mr. Liu Zhengdong, Mr. Li Yang, Mr. Zhang Xiao, Mr. Chen Bo, Mr. Yang Jian, Ms. Huang Ying, Mr. Ma Qinglang, Mr. Lai Zhuangchai.

Last but not the least, I am especially grateful to my devoted wife, Ms. Wang Lingling, for her selfless love, continuous support and encouragement.

This thesis is dedicated to my parents, Mr. Fan Baozhu and Ms. Cui Zhi, for giving me life and raising me up.

TABLE OF CONTENTS

ACKNOWLEDGEMENT	I
TABLE OF CONTENTS	II
ABSTRACT.....	VII
LIST OF FIGURES	X
LIST OF ABBREVIATIONS	XXV
CHAPTER 1 INTRODUCTION.....	1
1.1 BACKGROUND.....	1
1.2 LITERATURE REVIEW	3
1.2.1 Introduction to Noble Metal Nanomaterials	3
1.2.2 Phase Controlled Synthesis of Noble Metal Nanomaterials	9
1.2.3 The Influence of Crystal Phase on Noble Metal Nanomaterials.....	17
1.2.5 Short Summary	23
CHAPTER 2 AIMS AND MOTIVATION.....	24
2.1 OBJECTIVES AND SCOPE.....	24
2.2 HYPOTHESIS.....	25
CHAPTER 3 EXPERIMENTAL DETAILS.....	27
3.1 CHEMICALS AND MATERIALS.....	27
3.2 LIGAND EXCHANGE MEDIATED SYNTHESIS OF FACE-CENTERED CUBIC AU SQUARE SHEETS	28
3.2.1 Synthesis of Graphene Oxide	28

3.2.2 Synthesis of Hexagonal Close-Packed Au Square Sheets on GO Sheets	28
3.2.3 Ligand Exchange on Hexagonal Close-Packed Au Square Sheets.....	29
3.2.4 Fabrication of Cross-Section Samples of Face-Centered Cubic Au Square Sheets	29
3.2.5 Localized Surface Plasmon Resonance Study of Individual Face-Centered Cubic Au Square Sheets	30
3.3 METAL COATING ASSISTED SYNTHESIS OF NOVEL BIMETALLIC NANOSHEETS	31
3.3.1 Synthesis of Face-Centered Cubic Au@Ag Square Sheets	31
3.3.2 Synthesis of Hexagonal Close-Packed/Face-Centered Cubic Au@Ag Square Sheets	31
3.3.3 Synthesis of Face-Centered Cubic Au@Pt Nanosheets.....	32
3.3.4 Synthesis of Face-Centered Cubic Au@Pd Nanosheets.....	32
3.3.5 Fabrication of Cross-Section Samples of Face-Centered Cubic Au@Ag Square Sheets	33
3.3.6 Fabrication of Cross-Section Samples of Hexagonal Close-Packed/Face-Centered Cubic Au@Ag Square Sheets	33
3.3.7 Fabrication of Cross-Section Samples of Face-Centered Cubic Au@Pt Rhombic Nanosheets	34
3.3.8 Localized Surface Plasmon Resonance Study of Individual Face-Centered Cubic Au@Ag Square Sheets	34
3.4 COLLOIDAL SYNTHESIS OF 4H HEXAGONAL AU NANORIBBONS.....	35
3.4.1 Synthesis of 4H Au Nanoribbons	35
3.4.2 Ligand Exchange on 4H Au Nanoribbons	35

3.4.3 Synthesis of Polytypic 4H/Face-Centered Cubic Au@Ag Nanoribbons	36
3.4.4 Synthesis of Polytypic 4H/Face-Centered Cubic Au@Pd Nanoribbons	36
3.4.5 Synthesis of Polytypic 4H/Face-Centered Cubic Au@Pt Nanoribbons	37
3.4.6 Localized Surface Plasmon Resonance Study of Individual 4H Au Nanoribbons	37
3.4.7 Density Functional Theory Computational Details	38
3.4.8 Finite-Element-Method Simulation	38
3.5 CHARACTERIZATIONS	39
3.5.1 Transmission Electron Microscopy	39
3.5.2 Aberration-Corrected Transmission Electron Microscopy	40
3.5.3 X-Ray Diffraction	40
3.5.4 Atomic Force Microscopy	41
3.5.5 X-ray Photoelectron Spectroscopy	41
CHAPTER 4 RESULTS AND DISCUSSIONS	42
4.1 LIGAND EXCHANGE MEDIATED SYNTHESIS OF FACE-CENTERED CUBIC AU SQUARE SHEETS	42
4.1.1 Introduction	42
4.1.2 Synthesis and Characterization of Face-Centered Cubic Au Square Sheets	44
4.1.3 Effect of Ligand Concentration	51
4.1.4 Effect of Various Kinds of Thiol Molecules	53
4.1.5 Monochromated Electron Energy Loss Spectroscopy Measurement of Individual Face-Centered Cubic Au Square Sheets	55
4.1.6 Short Summary	57

4.2 METAL COATING ASSISTED SYNTHESIS OF NOVEL BIMETALLIC NANOSHEETS	58
4.2.1 Introduction	58
4.2.2 Synthesis and Characterization of Face-Centered Cubic Au@Ag Square Sheets	60
4.2.3 Synthesis and Characterization of Polytypic Hexagonal Close-Packed/Face-Centered Cubic Au@Ag Square Sheets	67
4.2.4 Role of Surfactant in the Synthesis of Au@Ag Square Sheets	73
4.2.5 Synthesis and Characterization of Face-Centered Cubic Au@Pt Nanosheets	76
4.2.6 Synthesis and Characterization of Face-Centered Cubic Au@Pd Nanosheets	87
4.1.7 Monochromated Electron Energy Loss Spectroscopy Measurement of Individual Face-Centered Cubic Au@Ag Square Sheets	91
4.2.8 Short Summary	92
4.3 COLLOIDAL SYNTHESIS OF 4H HEXAGONAL AU NANORIBBONS	94
4.3.1 Introduction	94
4.3.2 Synthesis and Characterization of 4H Au Nanoribbons	96
4.3.3 Ligand Exchange Induced Phase Transformation of 4H Au Nanoribbons	106
4.3.4 Monochromated Electron Energy Loss Spectroscopy Measurement of Individual 4H Au Nanoribbons	109
4.3.5 Synthesis of Polytypic 4H/Face-Centered Cubic Bimetallic Nanoribbons	112
4.3.6 Short Summary	118

CHAPTER 5 CONCLUSIONS AND RECOMMENDATIONS	119
5.1 CONCLUSIONS	119
5.2 RECOMMENDATIONS FOR FUTURE WORK	121
REFERENCES.....	124
LIST OF PUBLICATIONS	141

ABSTRACT

Noble metal nanomaterials have received extensive research interest owing to their unique physical and chemical properties, and various important applications like energy conversion and storage, surface enhanced Raman scattering (SERS), electronics, bioimaging and biosensing, information storage, photo- and electro-catalysis. Recently, it was found that the physical and chemical properties of noble metal nanomaterials can be greatly influenced by their crystal structures. Therefore, it is of paramount importance to develop new method/strategy for the efficient and facile synthesis of new noble metal nanomaterials with controlled crystal phase. To realize this objective, the following researches have been conducted.

Firstly, a ligand exchange method has been established for the shape and phase controlled synthesis of novel Au nanomaterials. By simply mixing the freshly prepared octadecanethiol (ODT) solutions with hexagonal close-packed (*hcp*) Au square sheet (AuSS), a unique *hcp*-to-face-centered cubic (*fcc*) phase transition is observed under ambient conditions, leading the formation of (100)_F-oriented *fcc* AuSSs. It is worthy to point out that the phase change of inorganic nanomaterials is usually realized at extreme conditions, such as high pressure and high temperature. Importantly, during the process of ligand exchange mediated synthesis, the crystallinity degree of the as-prepared *fcc* AuSSs can be well modulated by changing the concentration of ODT molecules. Besides ODT, many other kinds of thiol molecules can also result in the formation of *fcc* AuSSs from the *hcp* AuSSs. Remarkably, monochromated electron energy loss spectroscopy (EELS) of individual *fcc* AuSSs reveals a strong localized surface plasmon resonance (LSPR) absorption in the infrared range.

Secondly, the metal coating approach has been used for the synthesis of ultrathin noble bimetallic nanosheets (thickness < 5 nm) with controlled shape, structure and composition. Via the solution deposition of Ag onto *hcp* AuSSs in the absence of oleylamine, (100)_f oriented *fcc* Au@Ag square sheet has been prepared. In contrast, polytypic *hcp/fcc* Au@Ag square sheet with an orientation of (110)_h/(101)_f is synthesized via the epitaxial growth Ag on *hcp* AuSSs in the presence of oleylamine. Besides, the synthesis of ultrathin *fcc* Au@Pt rhombic nanosheets has been realized via the epitaxial seeded growth of Pt on the *hcp* AuSSs at ambient conditions. Importantly, the as-prepared *fcc* Au@Pt rhombic nanosheets show an unusual orientation of (101)_f. Significantly, by changing Pt to Pd, (101)_f oriented *fcc* Au@Pd rhombic nanosheets can also be obtained from the *hcp* AuSSs. Interestingly, a tiny amount of (100)_f oriented *fcc* Au@Pd and Au@Pt square nanosheets are found to be coexisting with the as-prepared Au@Pd and Au@Pt rhombic nanosheets, respectively. Moreover, monochromated EELS of individual *fcc* Au@Ag square sheets reveals a strong LSPR absorption in the infrared range.

Thirdly, the high-yield colloidal synthesis of Au nanoribbons (NRBs) with the 4H hexagonal crystal structure, a novel polytype of Au, has been demonstrated. Note that Au usually crystallizes in the common *fcc* phase. The as-prepared Au NRBs have a thickness of 2.0–6.0 nm, width of 15.0–61.0 nm and length of 0.5–6.0 μm. Interestingly, the Au NRB undergoes a phase change from the initial 4H to *fcc* structures after ligand exchange under ambient conditions. Monochromated EELS of individual 4H Au NRBs reveals a strong LSPR absorption in a wide range of infrared region. Importantly, the epitaxial growth of other noble metals, e.g. Ag, Pt and Pd, on 4H Au NRBs can induce the structure transformation of Au

NRBs from 4H to polytypic 4H/*fcc* structures, resulting in the production of noble bimetallic 4H/*fcc* Au@Ag, Au@Pd and Au@Pt core-shell nanostructures, respectively. The unprecedented synthesis of 4H Au NRBs and their derivative nanostructures will provide new opportunities for the phase-controlled synthesis of new advanced nanomaterials which may have a wide range of promising applications.

LIST OF FIGURES

- Figure 1-1.** Transmission electron microscopy (TEM) images of the Au nanorods with an aspect ratio of (a) 2 ± 1 (average size, 37×19 nm), (b) 4.2 ± 1 (average size, 50×12 nm) and (c) 6 ± 2 (average size, 50×8 nm). (d) The corresponding normalized extinction spectra, from left to right, of the Au nanorods shown in (a-c), respectively. Copyright 2009, Nature Publishing Group.3
- Figure 1-2.** Schematic illustration for the (a) surface plasmon polariton and (b) localized surface plasmon resonance. Copyright 2007, Annual Reviews.5
- Figure 1-3.** (a) The typical TEM image of a Pt tetrahedron. Inset: a (001)-oriented model of the Pt tetrahedron. (b) The corresponding selected area electron diffraction (SAED) pattern of the Pt tetrahedron shown in (a), which is collected from the zone axis of [001]. (c) High-resolution TEM (HRTEM) image of the marked region in (a). (d) Atomic structure model of a Pt(730) plane, which is rich of stepped atoms and consisted of (310) and (210) subfacets. (e) HRTEM image taken from another Pt tetrahedron to demonstrate the atomic surface steps in the areas consisted of (310) and (210) subfacets. Copyright 2007, American Association for the Advancement of Science.8
- Figure 1-4.** (a) XRD patterns of (I) the as-prepared 4 nm FePt NPs, and (II-V) a series of FePt NPs annealed under N_2 gas for 30 min at a temperature of 450 °C, 500 °C, 550 °C and 600 °C, respectively. Copyright 2000, American Association for the Advancement of Science. (b,c) The crystal unit cells of *fcc* and *fcc* FePt NPs, respectively. Copyright 2010, American Chemical Society.9
- Figure 1-5.** (a) The simulated X-ray diffraction (XRD) patterns of *fcc* and *fcc* structures, and their phase transformation process under high pressure. Inset: the

crystal structures of both *fcc* and *fct* phases. The *c/a* ratio of *fct* phase was set as 0.88 ($\ll 0.968$) in order to achieve a higher contrast. (b) Typical TEM image of the as-prepared Pd nanocubes. (c) Typical XRD patterns of the obtained Pd nanocubes from 0.3 GPa to 24.8 GPa. Copyright 2008, American Chemical Society. 11

Figure 1-6. (a) XRD patterns of Ag NPs with different average sizes of 14 nm, 20 nm and 35 nm, respectively. (b,c) SAED patterns taken from individual Ag nanoparticles with zone axes of $[110]_{3C}$ and $[1\bar{1}01]_{4H}$, respectively. Copyright 2001, American Physical Society. 12

Figure 1-7. (a) Typical HRTEM image of a 4H Ag nanowire. Insets: the bottom-left inset shows the corresponding SAED pattern of the 4H Ag nanowire shown in (a); the top-right inset demonstrates the zoom-in image of the marked region in (a), which is overlaid with some green dots to indicate the atomic projection of 4H Ag nanowire paralleling to $[\bar{2}113]$. (b) The simulated cross section of a typical 4H Ag nanowire with the Wulff's construction and broken-bond rule, in which the surface of Ag nanowire is marked by a red arrow and enclosed by $\{10\bar{1}1\}$ and $\{0001\}$ planes, and the surface energy plot is marked by a black arrow. Copyright 2006, American Chemical Society. 14

Figure 1-8. (a) Typical HRTEM image of a *fcc* Ru NP. Inset: schematic illustration of the decahedral structure. (b) Typical HRTEM image of a *hcp* Ru NP. Inset: schematic illustration of the *hcp* lattice observed along the $[100]$ direction. Copyright 2013, American Chemical Society. 14

Figure 1-9. (a) Schematic illustration for the synthesis of *hcp* AuSSs on GO sheets. (b) Typical TEM image of the obtained *hcp* AuSSs. Inset: crystallography models of the *hcp* AuSSs. (c) HRTEM image of a typical *hcp* AuSS. (d,e) Typical SAED

patterns of an <i>hcp</i> AuSS taken from the $[110]_h$ and $[320]_h$ zone axes, respectively. Copyright 2011, Nature Publishing Group.	16
Figure 1-10. (a) The composition change of <i>fcc</i> and <i>fcc</i> FePt NPs in 0.5 M H_2SO_4 solution at different times. Copyright 2010, American Chemical Society. (b) The Ultraviolet-visible (UV-vis) reflectance spectra of 3C and 4H Ag films. Inset: Photographs of the 3C and 4H Ag films. Copyright 2014, IOP Publishing Ltd. (c) The size-dependent temperature for 50% conversion of CO to CO_2 for the <i>fcc</i> and <i>hcp</i> Ru NPs. Copyright 2013, American Chemical Society. (d) The change of Hooge parameter χ_H ($f = 1$ Hz) with temperature for the <i>fcc</i> (open circles) and <i>hcp</i> (filled circles) Ag nanowires. Copyright 2008, American Institute of Physics.	18
Figure 1-11. (a) Typical HAADF-STEM image of a concave Au nanorod ²² . (b) The average monochromated EELS spectrum of the Au nanorod after removing the zero-loss peak. (c,d) The corresponding EELS maps of surface plasmon resonance intensity of the Au nanorod at 1.70 eV ($\lambda = 730$ nm) and 2.40 eV ($\lambda = 517$ nm), respectively. Copyright 2007, IOP Publishing Ltd.	20
Figure 1-12. (a) The normalized monochromated EELS spectra and corresponding high-angle annular dark-field STEM (HAADF-STEM) images of Ag NPs with different sizes from 1.7 nm to 11 nm. (b) The plot of particle diameter of Ag NPs versus surface plasmon resonance energy. Inset: the plot of particle diameter of Ag NPs versus the bulk plasmon resonance energy. Copyright 2012, Nature Publishing Group.	21
Figure 4-1. (a) TEM image of <i>hcp</i> AuSSs prepared on GO sheets. (b) SAED pattern of an <i>hcp</i> AuSS collected along $[110]_h$ zone axis. (c) HRTEM image of an <i>hcp</i> AuSS.	44

Figure 4-2. (a) TEM image of a folded <i>hcp</i> AuSS. (b) AFM image and height profile (inset) of an <i>hcp</i> AuSS.	45
Figure 4-3. (a) EDS investigation of AuSSs deposited on a copper grid after the oleylamine-to-ODT ligand exchange. (b) STEM image and corresponding element mappings of an AuSS after ligand exchange.	46
Figure 4-4. XPS spectra of AuSSs on GO sheets (a) before and (b) after ligand exchange from oleylamine to ODT.	47
Figure 4-5. (a,b) TEM images of <i>fcc</i> AuSSs on GO sheets. (c,d) SAED patterns taken along (c) $[100]_f$ and (d) $[310]_f$ zone axes of an <i>fcc</i> AuSS in (b). (e,f) HRTEM images of <i>fcc</i> AuSSs. (g) HAADF-STEM image demonstrating cross-section of an <i>fcc</i> AuSS. Inset: schematic illustration for the preparation method and view direction of the cross-section sample. (h,i) Aberration-corrected HAADF-STEM images showing the cross-section of the <i>fcc</i> AuSS in (g).	48
Figure 4-6. AFM image and step investigation of an <i>fcc</i> AuSS.	49
Figure 4-7. Schematic illustration for phase change of <i>hcp</i> AuSSs induced by ligand exchange of oleylamine with ODT molecules. Both top and side views are shown.	50
Figure 4-8. TEM images and SAED patterns of Au nanostructures prepared via ligand exchange with ODT at different concentrations for 5 min: (a,b) 2 mM, (c,d) 5 mM, and (e,f) 10 mM.	51
Figure 4-9. TEM images and SAED patterns of Au nanostructures prepared via ligand exchange with ODT at different concentrations for 5 min: (a,b) 20 mM, (c,d) 50 mM, (e,f) 100 mM, and (g,h) 200 mM.	52
Figure 4-10. (a,c,e,g) TEM images and (b,d,f,h) SAED patterns of AuSSs after the oleylamine-to-ODT ligand exchange at different concentrations of AuSSs: (a,b)	

1000 μL AuSS solution (Au atom concentration: 4.6 mM) mixed with 1000 μL ODT solution (50 mM), (c,d) 200 μL AuSS solution (Au atom concentration: 23 mM) mixed with 200 μL ODT solution (50 mM), (e,f) 100 μL AuSS solution (Au atom concentration: 46 mM) mixed with 100 μL ODT solution (50 mM); (g,h) 25 μL AuSS solution (Au atom concentration: 92 mM) mixed with 25 μL ODT solution (50 mM).53

Figure 4-11. Chemical structures of n-alkane thiols (in red color): 1-octadecanethiol (ODT), 1-dodecanethiol (DDT), 1-octanethiol (OT) and 1-propanethiol (PT); hydrophilic thiols (in green color): 11-mercapto-1-undecanol (MUDO), 6-mercapto-1-hexanol (MHO), 11-mercaptoundecanoic acid (MUDA) and 3-mercaptopropionic acid (MPA); aromatic thiol (in purple color): benzeneethanethiol (BET); dithiol (in blue color): 1,6-hexanedithiol (HdT).....54

Figure 4-12. TEM images and SAED patterns of *fcc* AuSSs prepared after the oleylamine-to-thiol ligand exchange with different thiol molecules (the concentration of thiols is 50 mM): (a) DDT, (b) OT, (c) PT, (d) MUDO; (e) MHO, (f) MUDA, (g) MPA; (h) BET; (i) HdT.55

Figure 4-13. (a) Schematic illustration for monochromated EELS characterization of a single *fcc* AuSS on GO sheet. (b) EELS spectra collected from an individual AuSS on GO sheet (excited next to edge and corner of an *fcc* AuSS and GO sheet. Inset: STEM image of the selected AuSS on GO sheet (scale bar, 20 nm), in which positions of the focused electron beam are indicated.56

Figure 4-14. (a) TEM image of *fcc* Au@Ag square sheets on GO sheets by using ascorbic acid as reductant. (b,c) SAED patterns taken along (b) $[100]_f$ and (c) $[310]_f$ zone axes of an *fcc* Au@Ag square sheet. (d,e) HRTEM images of an *fcc* Au@Ag square sheet. Insets in (d,e): fast Fourier transform (FFT) patterns of the

HRTEM images in (d) and (e). (f) HAADF-STEM image and (g,h) STEM-EDS element mappings of an <i>fcc</i> Au@Ag square sheet. (i) Aberration-corrected HAADF-STEM image and STEM-EDS element mapping showing the cross section of an <i>fcc</i> Au@Ag square sheet.	60
Figure 4-15. (a) TEM image and (b) SAED pattern of an <i>fcc</i> Au@Ag square sheet on GO by using NaBH ₄ as reductant. (c) HRTEM image and (d) FFT pattern of obtained <i>fcc</i> Au@Ag square sheets.	61
Figure 4-16. STEM-EDS spectrum of <i>fcc</i> Au@Ag square sheets. The average atomic ratio between Au and Ag is estimated to be 1: 1.4.	61
Figure 4-17. (a,c) HAADF-STEM images and (b,d) STEM-EDS line scanning analyses of obtained <i>fcc</i> Au@Ag square sheets.	62
Figure 4-18. High-resolution XPS spectra of (a) Au 4f, (b) Ag 3d, and (c) N 1s in obtained <i>fcc</i> Au@Ag square sheets.	63
Figure 4-19. (a) Bright-field and (b) dark-field STEM images of the cross section of an <i>fcc</i> Au@Ag square sheet. (c) STEM-EDS line scanning profile of the cross section shown in (a). (d) STEM image and (e,f) STEM-EDS element mappings of the cross-section sample of an <i>fcc</i> Au@Ag square sheet.	63
Figure 4-20. (a) TEM image, (b) HRTEM image and (c) FFT pattern of a cross-section sample of an <i>fcc</i> Au@Ag square sheet.	64
Figure 4-21. TEM images of a folded (a) <i>hcp</i> AuSS and (b) <i>fcc</i> Au@Ag square sheet. The Moiré pattern observed in (b) are induced by the folding of <i>fcc</i> Au@Ag square sheet.	64
Figure 4-22. (a) TEM image and (b) SAED pattern of an irregular-shaped <i>fcc</i> Au@Ag sheet. (c,d) HRTEM images of the marked regions in (a). (e) HAADF-	

STEM image and (f,g) STEM-EDS element mapping of an irregular-shaped <i>fcc</i> Au@Ag sheet.....	65
Figure 4-23. STEM-EDS spectrum of irregular-shaped <i>fcc</i> Au@Ag sheets. The average atomic ratio between Au and Ag is estimated to be 1: 0.3.	66
Figure 4-24. (a) TEM image of <i>hcp/fcc</i> Au@Ag square sheets on GO sheet. (b) SAED pattern and (c,d) HRTEM images of an <i>hcp/fcc</i> Au@Ag square sheet. (e,g) Aberration-corrected HAADF-STEM images and (f,h) FFT patterns of the cross sections of the <i>hcp/fcc</i> Au@Ag square sheets collected along $[1\bar{1}0]_h/[\bar{1}\bar{2}1]_f$ and $[001]_h/[\bar{1}11]_f$ zone axes, respectively.....	67
Figure 4-25. STEM-EDS spectrum of <i>hcp/fcc</i> Au@Ag square sheets. The average atomic ratio between Au and Ag is estimated to be 1: 1.5.	68
Figure 4-26. (a) HAADF-STEM image and (b,c) STEM-EDS element mapping of an <i>hcp/fcc</i> Au@Ag square sheet.	68
Figure 4-27. (a,c) HAADF-STEM images and (b,d) STEM-EDS line scanning analyses of <i>hcp/fcc</i> Au@Ag square sheets.	69
Figure 4-28. Aberration-corrected (a) bright-field and (b) dark-field STEM images of a cross section of <i>hcp/fcc</i> Au@Ag square sheets cut along $[001]_h/[\bar{1}11]_f$ directions. (c) FFT pattern of the region marked in (b). (d) HAADF-STEM image and (e-g) STEM-EDS element mappings of a cross section of <i>hcp/fcc</i> Au@Ag square sheets. (h) HAADF-STEM image of the cross section of an <i>hcp/fcc</i> Au@Ag square sheet (Inset: EELS mapping of Ag).....	70
Figure 4-29. High-resolution XPS spectra of (a) Au 4f, (b) Ag 3d, and (c) N 1s in obtained <i>hcp/fcc</i> Au@Ag square sheets.	70

Figure 4-30. (a) Low-magnification and (b-c) high-resolution TEM images of a cross-section of obtained <i>hcp/fcc</i> Au@Ag square sheets cut along $[001]_h/[111]_f$ directions. (d) FFT pattern of HRTEM image shown in (c).	71
Figure 4-31. (a) TEM image and (b) SAED pattern of an <i>hcp/fcc</i> Au@Ag square sheet. (c) The dark-field TEM image acquired with $(1\bar{1}0)_h$ diffraction spot indicated in (b).	72
Figure 4-32. Schematic illustration on the preparation of cross sections of <i>hcp/fcc</i> Au@Ag square sheets.	72
Figure 4-33. Schematic illustration for the Ag coating on <i>hcp</i> AuSSs (a) with ascorbic acid as reductant in the absence of oleylamine, and (b) with oleylamine as reductant and capping agent.	73
Figure 4-34. (a) TEM image and (b) SAED pattern along $[110]_h/[101]_f$ zone axes of an <i>hcp/fcc</i> Au@Ag square sheet, which was synthesized via using octylamine as reductant and capping agent. (c) HRTEM image of obtained <i>hcp/fcc</i> Au@Ag square sheets.	74
Figure 4-35. (a) TEM image and (b) SAED pattern along $[100]_f$ zone axis of an <i>fcc</i> Au@Ag square sheet, which was obtained by using dioctylamine as reductant and capping agent. (c) HRTEM image of obtained <i>fcc</i> Au@Ag square sheets.	75
Figure 4-36. (a) TEM image and (b) SAED pattern of a $(101)_f$ -orientated <i>fcc</i> Au@Pt rhombic nanosheet. (c,d) HRTEM images of an <i>fcc</i> Au@Pt rhombic nanosheet collected from the center and edge areas, respectively. Insets in (c,d): FFT patterns of the HRTEM images in (c,d). (e) HAADF-STEM image and (f,g) STEM-EDS element mappings of a $(101)_f$ -oriented <i>fcc</i> Au@Pt rhombic nanosheet.	76

Figure 4-37. (a,c,e,g) TEM images and (b,d,f,h) SAED patterns of obtained <i>fcc</i> Au@Pt rhombic nanosheets.....	77
Figure 4-38. TEM images of a folded (a) <i>hcp</i> AuSS, (b) <i>fcc</i> Au@Pt rhombic nanosheet, and (c) <i>fcc</i> Au@Pd rhombic nanosheet.	77
Figure 4-39. (a) TEM image and (b) SAED pattern of an <i>fcc</i> Au@Pt rhombic nanosheet. (c) Dark-field TEM image taken with $(1\bar{1}\bar{1})_f$ diffraction spot as marked in (b).....	78
Figure 4-40. STEM-EDS spectrum of obtained <i>fcc</i> Au@Pt rhombic nanosheets. The average atomic ratio between Au and Pt is 1: 1.	78
Figure 4-41. (a) HAADF-STEM image and (b) STEM-EDS line scanning analysis of obtained <i>fcc</i> Au@Pt rhombic nanosheets.	79
Figure 4-42. (a) Schematic illustration for fabrication of cross sections of <i>fcc</i> Au@Pt rhombic nanosheets. The green dashed lines show the cutting direction with FIB. (b) The HAADF-STEM image of obtained cross section of an <i>fcc</i> Au@Pt rhombic nanosheet. The regions in the two red rectangles indicate the alignment marks produced in the process for preparation of cross sections of <i>fcc</i> Au@Pt rhombic nanosheets.....	79
Figure 4-43. (a) Low-magnification and (b) aberration-corrected HAADF-STEM images of cross section of an <i>fcc</i> Au@Pt rhombic nanosheet. (c) FFT pattern of HAADF-STEM image in (b). (d) HAADF-STEM image of cross section of the <i>fcc</i> Au@Pt rhombic nanosheet. (e) STEM-EDS element mapping of Au (in red color) and Pt (in green color), and the overlapped image. (f) STEM-EDS line scanning plots of the selected areas indicated by rectangle and line in (d), respectively.	80

Figure 4-44. (a) HAADF-STEM image of a cross section of an <i>fcc</i> Au@Pt rhombic nanosheet. (b,c) Selected-point STEM-EDS spectra taken from the regions marked by red and green dots in (a), respectively.	81
Figure 4-45. (a) TEM image and (b) SAED pattern of an <i>fcc</i> Au@Pt square nanosheet. (c) HRTEM image of an <i>fcc</i> Au@Pt square nanosheet. Inset in (c): FFT pattern of HRTEM image shown in (c).	82
Figure 4-46. (a) HAADF-STEM image and (b,c) STEM-EDS element mappings of an <i>fcc</i> Au@Pt square nanosheet.	83
Figure 4-47. STEM-EDS spectrum of <i>fcc</i> Au@Pt square nanosheets. The average atomic ratio between Au and Pt is 1.0: 0.7.	83
Figure 4-48. The scheme illustrating the synthesis of (101) _f oriented <i>fcc</i> Au@Pt rhombic nanosheets with twin structures (indicated by dashed red line) from (110) _h oriented <i>hcp</i> AuSSs (top panel), along with the formation of a tiny amount of (100) _f oriented <i>fcc</i> Au@Pt square nanosheets (bottom panel).	84
Figure 4-49. (a) TEM image and (b) SAED pattern of a (101) _f -orientated <i>fcc</i> Au@Pd rhombic nanosheet. (c,d) HRTEM images of an <i>fcc</i> Au@Pd rhombic nanosheet collected from center and edge areas, respectively. Insets in (c,d): FFT patterns of the HRTEM images in (c,d). (e) HAADF-STEM image and (f,g) STEM-EDS element mappings of a (101) _f -oriented <i>fcc</i> Au@Pd rhombic nanosheet.	87
Figure 4-50. (a) (a,c,e,g) TEM images and (b,d,f,h) SAED patterns of obtained <i>fcc</i> Au@Pd rhombic nanosheets.	88
Figure 4-51. (a) TEM image and (b) SAED pattern of an <i>fcc</i> Au@Pd rhombic nanosheet. (c) Dark-field TEM image taken with (11 $\bar{1}$) _f diffraction spot as marked in (b).	88

Figure 4-52. STEM-EDS spectrum of <i>fcc</i> Au@Pd rhombic nanosheets. The average atomic ratio between Au and Pt is 1.0: 0.8.....	89
Figure 4-53. (a) HAADF-STEM image and (b) STEM-EDS line scanning analysis of an <i>fcc</i> Au@Pd rhombic nanosheet.	89
Figure 4-54. (a) TEM image, (b) SAED pattern, and (c) HRTEM image of an <i>fcc</i> Au@Pd square nanosheet. (d) HAADF-STEM image and (e,f) STEM-EDS element mappings of an <i>fcc</i> Au@Pd square nanosheet.	90
Figure 4-55. STEM-EDS spectrum of <i>fcc</i> Au@Pd square nanosheets. The average atomic ratio between Au and Pt is 1.0: 0.9.	91
Figure 4-56. EELS spectra collected from an individual Au@Ag square sheet on the GO sheet (excited next to edge and corner of an <i>fcc</i> Au@Ag square sheet and the GO sheet. Inset: STEM image of a selected Au@Ag square sheet on the GO sheet (scale bar, 20 nm), in which positions of focused electron beam are indicated.	92
Figure 4-57. (a) TEM image of 4H Au NRBs. (b,c) TEM image and SAED pattern collected along $[110]_{4H}$ zone axis of an Au NRB. (d,e) Aberration-corrected HRTEM images collected from the center (d) and edge (e) regions of an Au NRB, respectively. (f) Schematic illustration for the unit cell of 4H Au. (g) Crystallographic models showing the top (top panel) and side (bottom panel) views of a 4H Au NRB.	96
Figure 4-58. (a) TEM and (b) HAADF-STEM images of obtained 4H Au NRBs.	97
Figure 4-59. TEM images of two folded 4H Au NRBs, showing a thickness of 2.5 nm (a) and 4.0 nm (b), respectively.	97

Figure 4-60. (a) AFM image and (b) height analysis of a 4H Au NRB deposited on the Si/SiO ₂ substrate.	98
Figure 4-61. STEM-EDS spectrum of obtained 4H Au NRBs.	98
Figure 4-62. XPS spectra of 4H Au NRBs, demonstrating the core level peaks of (a) Au 4f, (b) N 1s, (c) Cl 2p and (d) C 1s.	99
Figure 4-63. (a) Low-magnification and (b) high-magnification TEM images of as-prepared Au NPs together with tiny amount of Au NWs obtained in the absence of 1,2-dichloropropane. (c) SAED pattern and (d) HRTEM image of obtained Au NPs.	100
Figure 4-64. XRD pattern of 4H Au NRBs collected in the (a) $\theta/2\theta$ and (b) 2θ modes.	102
Figure 4-65. The simulated HRTEM image of 4H Au NRBs. The HRTEM image simulation was executed using the multislice method as implemented in the MacTempas software.	102
Figure 4-66. (a) At the reaction time of 4 h, ultrathin Au NWs (1.4–2.0 nm in diameter) were formed. The Au NWs gradually grew over time to form Au NRBs with the widths of (b) 2.8–5.2 nm at 8 h, (c) 8.0–20.0 nm at 12 h and (d) 15.0–61.0 nm at 16 h.	103
Figure 4-67. (a) At the reaction time of 4 h, the 2H phase and stacking faults were found in obtained ultrathin Au NWs. (b) The 4H phase appeared at the reaction time of 8 h. Inset: the FFT pattern of the selected 4H domain in (b). (c) Au NRBs with 4H phase were obtained at the reaction time of 12 h. Inset: FFT pattern of the HRTEM image in (c).	103

- Figure 4-68.** TEM image of a ribbon-like polymer structure, probably formed from the assembly of (oleylamine)AuCl complex molecules via aurophilic interaction. 105
- Figure 4-69.** (a) TEM image of an Au NRB after ligand exchange. (b) SAED pattern of selected region by dashed rectangle in (a). (c) SAED pattern of $[013]_f$ zone axis was collected by tilting the Au NRB around $[200]_f$ zone axis for about 18.2° with respect to $[001]_f$ zone axis. (d-f) HRTEM images collected from the center (d), edge (e), and end (f) regions of the marked region in (a), respectively. (g) Schematic illustration for ligand-induced phase transition of an Au NRB. 107
- Figure 4-70.** (a) STEM-EDS spectrum of Au NRBs after ligand exchange. (b) HAADF-STEM image, and (c,d) STEM-EDS element mappings of an Au NRB after ligand exchange. 108
- Figure 4-71.** Schematic illustration for ligand exchange-induced phase change of Au NRB from 4H to *fcc* structures. 109
- Figure 4-72.** (a) Schematic illustration for monochromated EELS characterization of a single 4H Au NRB. The focused electron beam is located a few nanometers away from the Au NRB to excite and measure its LSPR. (b) Monochromated EELS spectra taken from individual Au NRBs excited at the different positions marked in (g). (c,d) DFT-calculated dielectric function of a 4H Au thin film with the limitation of 4 nm in the y direction. (e) Simulated EELS spectra of a 4H Au NRB based on the dielectric function in (c) and (d) using the FEM with an electron beam. Inset: the theoretical model of a single Au NRB, in which the excitation positions are indicated. (f) Simulated EELS spectra of an *fcc* Au NRB with dielectric function taken from Palik at the identical excitation positions as that in

(e). (g,h) HAADF-STEM image of a single Au NRB and its EELS mappings at different energy losses.	110
Figure 4-73. (a,b) TEM images of an Au@Ag NRB. (c) SAED pattern of an Au@Ag NRB collected along $[110]_{4H}/[101]_f$ zone axes. (d,e) HRTEM images of an Au@Ag NRB collected from the center (d) and edge (e) regions, respectively. (f,g) TEM images of an Au@Pd NRB. (h) SAED pattern of an Au@Pd NRB taken along $[110]_{4H}/[101]_f$ zone axes. (i,j) HRTEM images of an Au@Pd NRB taken from its center (i) and edge (j) areas, respectively.	112
Figure 4-74. STEM-EDS spectrum of 4H/fcc Au@Ag NRBs with an average Au/Ag atomic ratio of 1.0/1.7.	113
Figure 4-75. (a) HAADF-STEM image, and (b,c) STEM-EDS element mappings of a polytypic 4H/fcc Au@Ag NRB.	113
Figure 4-76. (a) HAADF-STEM image, and (b) STEM-EDS line scanning profile of a polytypic 4H/fcc Au@Ag NRB.	114
Figure 4-77. (a) TEM image and (b) SAED pattern of a polytypic 4H/fcc Au@Ag NRB. (c) The dark-field TEM image taken with $(1\bar{1}0)_{4H}$ diffraction spot indicated in (b).	115
Figure 4-78. STEM-EDS spectrum of polytypic 4H/fcc Au@Pd NRBs with an average Au/Pd atomic ratio of 1.0/1.2.	115
Figure 4-79. (a) HAADF-STEM image and (b,c) STEM-EDS element mappings of a polytypic 4H/fcc Au@Pd NRB.	115
Figure 4-80. (a) HAADF-STEM image and (b) STEM-EDS line scanning profile of a polytypic 4H/fcc Au@Pd NRB.	116

Figure 4-81. (a,b) TEM images and (c) SAED pattern of a polytypic 4H/ <i>fcc</i> Au@Pt NRB. (d) HAADF-STEM image and (e,f) STEM-EDS element mappings of a polytypic 4H/ <i>fcc</i> Au@Pt NRB.	117
Figure 4-82. STEM-EDS spectrum of polytypic 4H/ <i>fcc</i> Au@Pt NRBs with an average Au/Pt atomic ratio of 1.0/0.9.	117
Figure 4-83. (a) HAADF-STEM image, and (b) STEM-EDS line scanning profile of a polytypic 4H/ <i>fcc</i> Au@Pt NRB.	118

LIST OF ABBREVIATIONS

Surface enhanced Raman scattering	SERS
Octadecanethiol	ODT
Hexagonal close-packed	<i>hcp</i>
Au square sheet	AuSS
Face-centered cubic	<i>fcc</i>
Electron energy loss spectroscopy	EELS
Localized surface plasmon resonance	LSPR
Nanoribbon	NRB
Infrared	IR
Direct current	DC
Anodized aluminium oxide	AAO
Graphene oxide	GO
Face-centered tetragonal	<i>fct</i>
Nanoparticle	NP
Near-infrared	NIR
Surface plasmon resonance	SPR
Transmission electron microscopy	TEM
Selected area electron diffraction	SAED
High-resolution transmission electron microscopy	HRTEM
X-ray diffraction	XRD
Alternating current	AC
Poly(N-vinyl-2-pyrrolidone)	PVP
Ethylene glycol	EG

Triethylene glycol	TEG
Ultraviolet-visible	UV-vis
Oxygen reduction reaction	ORR
Formic acid oxidation reaction	FAOR
Scanning transmission electron microscopy	STEM
High-angle annular dark field	HAADF
Atomic force microscopy	AFM
X-ray photoelectron spectroscopy	XPS
Focused-ion beam	FIB
Scanning electron microscopy	SEM
Finite-element-method	FEM
Energy-dispersive X-ray spectroscopy	EDS
Nanocrystal	NC
Two-dimensional	2D
Nanowire	NW
Density functional theory	DFT

CHAPTER 1 INTRODUCTION

1.1 Background

Noble metal nanomaterials have attracted great attention due to their unique physical and chemical properties, and various important applications in surface enhanced Raman scattering (SERS), electrocatalysis, clean energy, infrared (IR) photothermal therapy, bioimaging and biosensing, etc¹⁻⁸. It has been widely recognized that the size, shape, composition, architecture and crystal structure of noble metal nanomaterials can greatly affect their functional properties^{2,9,10}. To date, noble metal nanomaterials with a well-defined size, shape, composition and architecture have been achieved^{2,11,12}. However, the crystal structure modulation of noble metal nanomaterials is still a big challenge.

In addition, almost all of the previously reported noble metal nanomaterials, especially those made of Au, Ag, Pd or Pt, crystallize in the common face-centered cubic (*fcc*) phase. The controlled synthesis of noble metal nanomaterials with new crystal structures remains great underdevelopment. As the functional properties of noble metal nanomaterials are closely related to their crystal structures^{13,14}, it is also of high importance to synthesize new crystal structures that may bring about improved/novel properties.

Many synthetic methods have been established to realize the phase control of noble metal nanomaterials so far. Examples include the thermal annealing method⁹, compression method¹⁵, direct current (DC) magnetron sputtering method¹⁶, porous anodized aluminum oxide (AAO) templated electrochemical deposition method¹⁷, polyol method¹⁸ and graphene oxide (GO) templated synthesis¹⁹. Among the

aforementioned methods, the thermal annealing and AAO templated electrochemical deposition methods have been mostly developed to achieve the phase controlled synthesis of noble metal nanomaterials. For instance, face-centered tetragonal (*fct*) FePt nanoparticles (NPs) could be obtained by annealing the preformed *fcc* FePt NPs at a temperature of 600 °C for 30 min⁹. By using porous anodized aluminum oxide (AAO) as a template, 4H Ag nanowires with a diameter of about 30 nm could be obtained with electrochemical deposition¹⁷. However, the thermal annealing method requires high temperature, and the AAO templated electrochemical deposition method involves multiple steps.

All in all, owing to the limitations of the existing synthetic methods, it is urgent and important to develop facile and low-cost wet chemical methods for the phase controlled synthesis of noble metal nanomaterials under mild conditions in order to further explore their valuable properties and applications, especially for the ultrathin noble metal nanomaterials.

Besides, for the optical property investigation of individual noble metal nanomaterials, the conventional optical spectroscopy cannot be used because of their low spatial resolution. Recently, monochromated electron energy loss spectroscopy (EELS) with both high spatial and high spectrum resolutions has been developed²⁰⁻²², which makes it possible to study the localized surface plasmon resonance (LSPR) absorption of individual noble metal nanomaterials.

1.2 Literature Review

1.2.1 Introduction to Noble Metal Nanomaterials

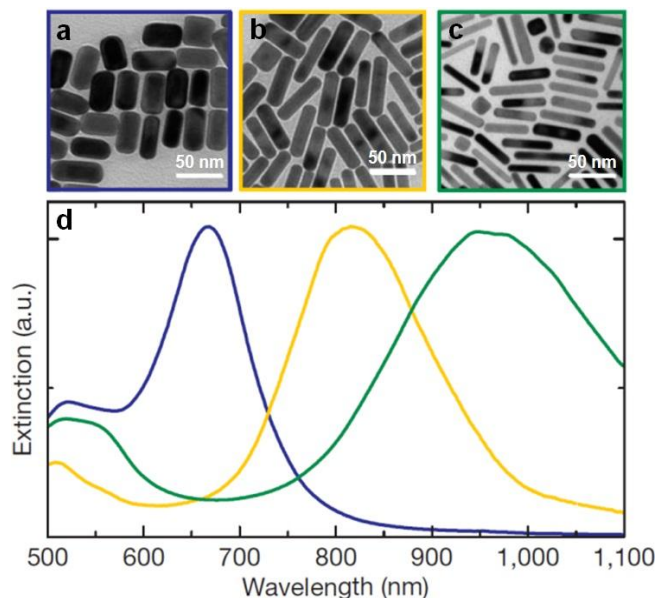


Figure 1-1. Transmission electron microscopy (TEM) images of the Au nanorods with an aspect ratio of (a) 2 ± 1 (average size, 37×19 nm), (b) 4.2 ± 1 (average size, 50×12 nm) and (c) 6 ± 2 (average size, 50×8 nm)²⁵. (d) The corresponding normalized extinction spectra, from left to right, of the Au nanorods shown in (a-c), respectively²⁵. Copyright 2009, Nature Publishing Group.

Nanomaterials, with at least one dimension between 1 nm and 100 nm, have received tremendous research interest during the past two decades^{2,23}. These nanoscale materials demonstrate quite different physical and chemical properties compared to their bulk counterparts, which is mainly caused by the well-known size-dependent effects²⁴. On the one hand, the surface area-to-volume ratio becomes very large when the size of a material is down to the nanometer scale, i.e. the scalable effect. On the other hand, by decreasing of the size of a material to the

nanometer range, the shell in systems with delocalized electrons is completed, resulting in a discontinuous behavior of quantum effect.

Among different kinds of nanomaterials, noble metal nanomaterials, including gold (Au), silver (Ag), palladium (Pd), platinum (Pt), rhodium (Rh), iridium (Ir), osmium (Os) and ruthenium (Ru), have been widely investigated and used for a range of important applications, such as surface enhanced Raman scattering (SERS), infrared (IR) photothermal therapy, biosensing, bioimaging and catalysis^{2,5,8,26}. The chemical and physical properties of noble metal nanomaterials are mostly controlled by their sizes, shapes, compositions, architectures and crystal structures^{2,24}. For instance, the light absorption of Au nanorods can be largely tuned from the visible region to the near-infrared (NIR) region by simply adjusting their aspect ratio of length to width (Figure 1-1)²⁵.

The light absorption of noble metal nanomaterials is derived from the coherent oscillation of surface conduction electrons excited by the electromagnetic radiation, which is well known as the localized surface plasmon resonance (LSPR)²⁷. Metals, especially noble metals, that own a small positive imaginary and negative real dielectric constant can support a surface plasmon resonance (SPR), in which the plasmons propagate in both x and y directions along the metal-dielectric interface, and decay quickly in the z direction (Figure 1-2a)²⁷. When the size of noble metals is reduced to the nanoscale that is smaller than the incident light wavelength, the plasmon will locally oscillate around the noble metal NPs with a frequency known as the LSPR (Figure 1-2b)²⁷. Theoretical and experimental studies have revealed that the LSPR of noble metal nanomaterials can be greatly affected by their size, shape, composition, inter-NP coupling, crystal structure as well as the local dielectric environment²⁸.

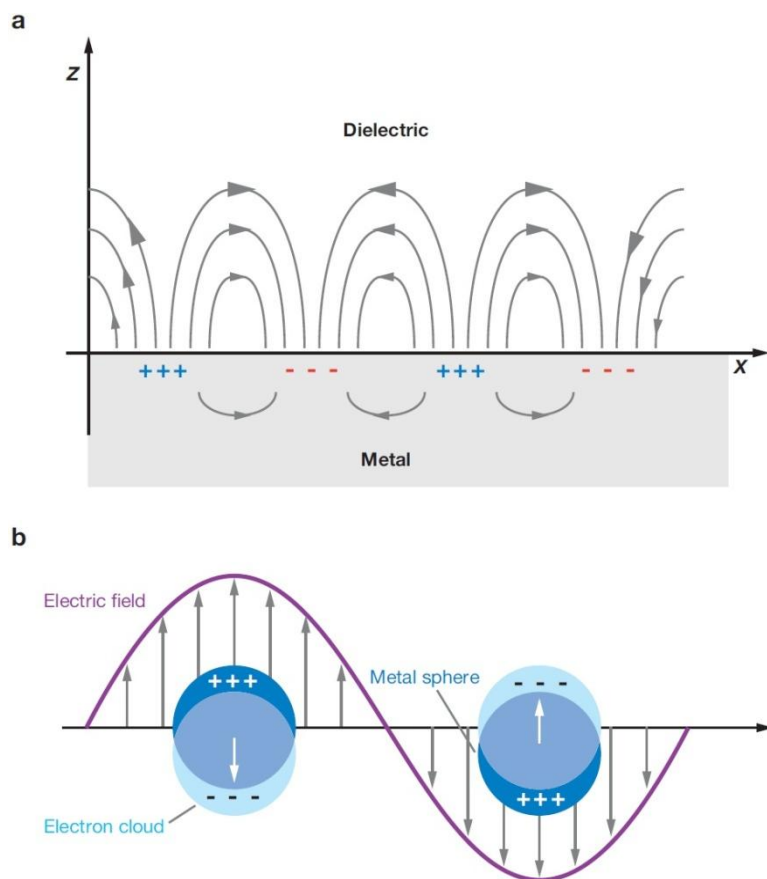


Figure 1-2. Schematic illustration for the (a) surface plasmon polariton and (b) localized surface plasmon resonance²⁷. Copyright 2007, Annual Reviews.

The unique optical properties of noble metal nanomaterials have enabled a wide range of important applications^{8,29-31}. For instance, Au and Ag NP arrays, in which the strong plasmonic coupling between adjacent NPs can result in the formation of Raman “hot spot”, have been used as efficient SERS substrates for the detection of small molecules⁴. Noble metal nanoplates with sharp edges and corners that show particularly strong electromagnetic field could also be applied as the SERS substrates³²⁻³⁴. Due to the extremely strong LSPR absorption of noble metal nanomaterials (e.g. Au nanocages, Au and Pd nanosheets) in the IR region, they can effectively increase the temperature of the local environments under IR light illumination^{6,35-37}. Therefore, these kinds of noble metal nanomaterials have been

involved in the photothermal therapy to kill cancer cells. Besides, as the LSPR absorption of noble metal nanomaterials is extremely sensitive to the dielectric constant variation of local environments³⁸, the noble metal nanomaterials, especially those possess a strong plasmonic absorption in the long wavelength region (such as the NIR region), could be used in the biosensing^{3,39,40}. Take Au nanoplates as a typical example, it has been reported that the LSPR absorption of Au nanoplates demonstrated an obvious red shift upon binding of the human anti-IgG to their surfaces³⁹.

In addition to the aforementioned unique optical properties and the related applications, the noble metal nanomaterials are also catalytically active and thus have been used in many kinds of catalytic applications⁴¹⁻⁴⁷. Previous investigations suggest that the catalytic activity of noble metal nanomaterials can be significantly affected by their sizes^{48,49}. By decreasing the size of noble metals, the proportion of low-coordination atomic sites will increase and thus give rise to an improved catalytic performance^{2,50}. For instance, although bulk Au is not catalytically active, the Au NPs with a size of 3-4 nm demonstrate a quite high catalytic activity for the low-temperature CO oxidation^{48,51,52}. A recent study showed that the Faradaic efficiency for electrocatalytic reduction of CO₂ at -0.89 V can be dramatically improved from 5.8% to 91.2% by simply reducing the size of Pd NPs from 10.3 nm to 3.7 nm⁴⁹.

Besides the size effect, the shape-dependent catalysis of noble metal nanomaterials has also been well documented⁵³⁻⁵⁵. The catalytic activity of noble metal nanomaterials can be improved by tuning their shapes^{2,50,54}. For example, it was reported that the catalytic activity of Pt@Pd cubes was almost five times of that of the Pt@Pd octahedra for formic acid oxidation in 0.1 M H₂SO₄¹². In

particularly, through the synthesis of nanopolyhedra that are enclosed with high-index facets, which are rich of surface atomic steps and low-coordination atomic sites, the catalytic activity of noble metal nanomaterials can be greatly increased⁵⁶⁻⁵⁸. For instance, Sun *et al.* first reported the successful synthesis of Pt tetrahedra with a square wave potential on the glass carbon substrate (Figure 1-3)⁵³. Importantly, as the obtained Pt tetrahedra are bound by the high-index facets of {730}, they exhibited a significantly improved catalytic activity of up to 400% in the electrocatalytic oxidation of small molecules (e.g. ethanol and formic acid) compared to either Pt nanospheres or commercial Pt/C⁵³. Besides, the catalytic selectivity can also be improved by adjusting the shapes of noble metal nanomaterials⁵⁵. Recently, it was found that the *cis*-to-*trans* isomerization of olefin was favored on the Pt nanotetrahedra, while the *trans*-to-*cis* isomerization of olefin was promoted on the Pt nanocubes⁵⁵. Importantly, the Pt nanospheres have been demonstrated no catalytic selectivity in the isomerization of olefin compared to the aforementioned Pt nanotetrahedra and nanocubes⁵⁵.

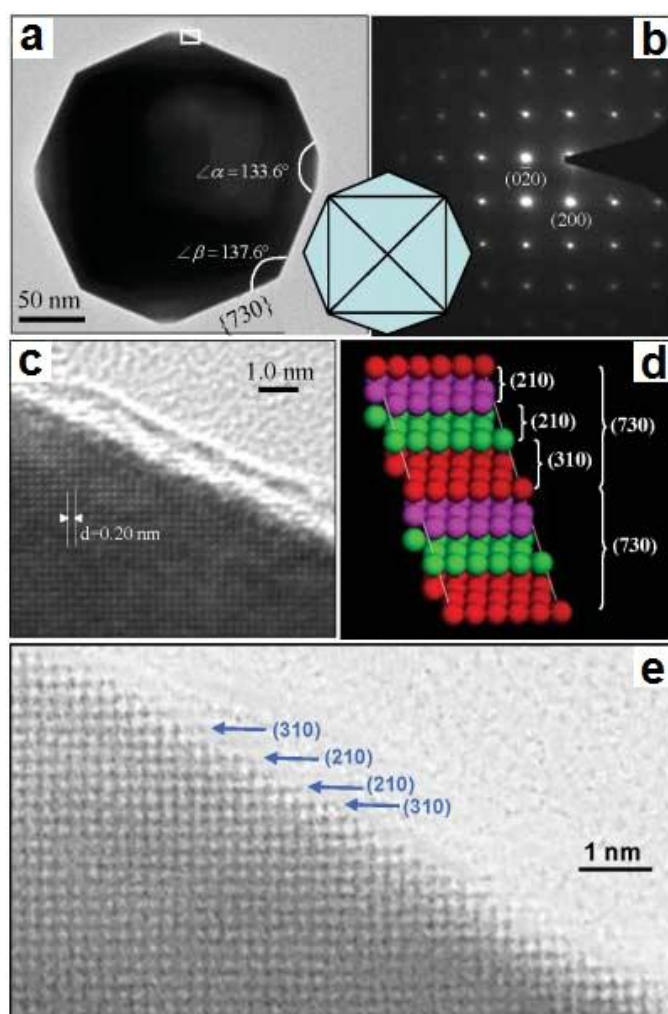


Figure 1-3. (a) The typical TEM image of a Pt tetrahexahedron. Inset: a (001)-oriented model of the Pt tetrahexahedron⁵³. (b) The corresponding selected area electron diffraction (SAED) pattern of the Pt tetrahexahedron shown in (a), which is collected from the zone axis of $[001]$ ⁵³. (c) High-resolution TEM (HRTEM) image of the marked region in (a)⁵³. (d) Atomic structure model of a Pt(730) plane, which is rich of stepped atoms and consisted of (310) and (210) subfacets⁵³. (e) HRTEM image taken from another Pt tetrahexahedron to demonstrate the atomic surface steps in the areas consisted of (310) and (210) subfacets⁵³. Copyright 2007, American Association for the Advancement of Science.

1.2.2 Phase Controlled Synthesis of Noble Metal Nanomaterials

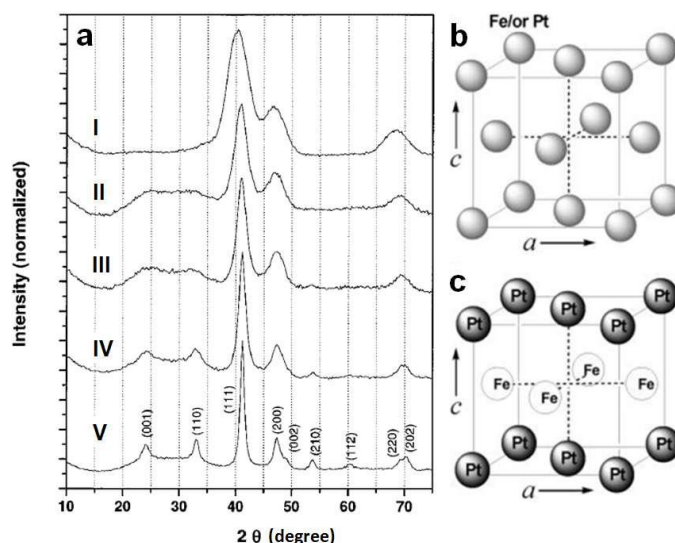


Figure 1-4. (a) XRD patterns of (I) the as-prepared 4 nm FePt NPs, and (II-V) a series of FePt NPs annealed under N_2 gas for 30 min at a temperature of 450 °C, 500 °C, 550 °C and 600 °C, respectively⁹. Copyright 2000, American Association for the Advancement of Science. (b,c) The crystal unit cells of *fcc* and *fct* FePt NPs, respectively¹³. Copyright 2010, American Chemical Society.

To date, various kinds of synthetic methods have been established to realize the phase controlled synthesis of noble metal nanomaterials, and they can be typically divided into three categories: post-processing methods, top-down methods and bottom-up methods. The post-processing methods, starting from the preformed nanomaterials, include the thermal annealing method and compression method^{9,15}. The top-down methods, starting from bulk materials, include the direct current (DC) magnetron sputtering method¹⁶. The bottom-up methods, starting from metal salts as the precursors, include the porous anodized aluminum oxide (AAO) templated electrochemical deposition method¹⁷, polyol method and graphene oxide (GO) templated synthesis^{18,19}. In this section, the aforementioned different

synthetic methods towards the phase controlled synthesis of noble metal nanomaterials will be systematically described, respectively.

Thermal annealing method has been effectively used in the synthesis of different noble metal nanomaterials with non-*fcc* crystal structures^{9,59,60}. In a typical experiment, noble metal nanomaterials with a particular crystal structure are firstly synthesized and then annealed under a high temperature to induce a phase transformation. In 2000, Sun *et al.* first observed that the crystal structure of FePt could be changed from the chemically disordered *fcc* to chemically ordered face-centered tetragonal (*fct*) phases by simply annealing the preformed FePt NPs in a N₂ glove box under a high temperature up to 600 °C for 30 min (Figure 1-4)⁹. However, the FePt NPs suffered from serious aggregation and sintering after annealing under such a high temperature (usually > 550 °C)⁶¹. Later, it was found that the coating of MgO shell on the preformed *fcc* FePt NPs can successfully prohibit the aggregation or sintering during the process of high temperature thermal annealing⁶². Most importantly, the MgO shell can be easily removed with a dilute acid washing after the thermal treatment, resulting in the formation of regular shaped *fct* FePt NPs⁶². Recently, it was reported that the chemically ordered *fct* FePtAu trimetallic NPs could also be synthesized by annealing the preformed chemically disordered *fcc* FePtAu NPs at 600 °C under 95% Ar + 5% H₂ for 1 h⁶³. Besides, chemically ordered *fct* FeAu NPs have also been synthesized by simply heating the preformed chemically disordered *fcc* FeAu NPs⁶⁴.

Another effective method for the phase-controlled synthesis of noble metal nanomaterials is the compression method^{15,65,66}. Typically, the noble metal nanomaterials with a certain phase are firstly synthesized and then loaded under a high pressure to alter their crystal structures in a diamond anvil cell. The pressure

induced phase transformation of noble metal nanomaterials can be monitored by the in-situ synchrotron X-ray diffraction. Guo *et al.* employed this method to synthesize *fct* Pd nanostructures by simply compressing the preformed *fcc* Pd nanocubes with an average edge length of about 10 nm under a high pressure up to 24.8 GPa (Figure 1-5)¹⁵. Recently, Sun *et al.* observed a multiple-step phase change in Ag nanoplates under high pressures: the local *hcp* domains disappeared first at a pressure of 1.03 GPa, and then the *fcc*-to-*fct* phase transformation occurred at a pressure of 12 GPa⁶⁵. Interestingly, the obtained metastable *fct* phase could change back to the *fcc* phase once the external pressure was unloaded⁶⁵.

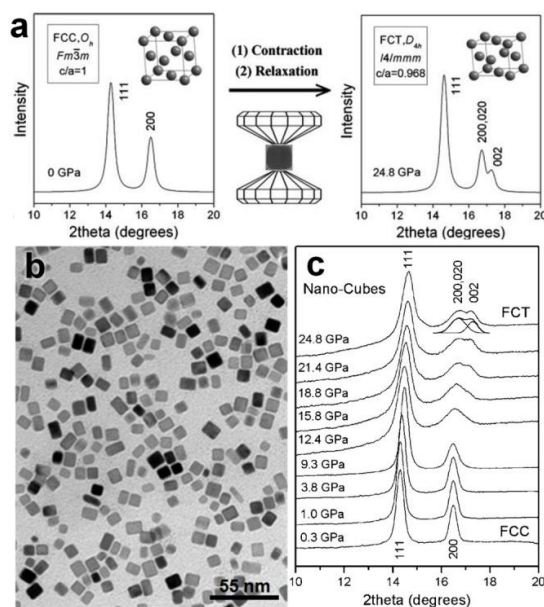


Figure 1-5. (a) The simulated X-ray diffraction (XRD) patterns of *fcc* and *fct* structures, and their phase transformation process under high pressure. Inset: the crystal structures of both *fcc* and *fct* phases. The c/a ratio of *fct* phase was set as 0.88 ($\ll 0.968$) in order to achieve a higher contrast¹⁵. (b) Typical TEM image of the as-prepared Pd nanocubes¹⁵. (c) Typical XRD patterns of the obtained Pd nanocubes from 0.3 GPa to 24.8 GPa¹⁵. Copyright 2008, American Chemical Society.

The DC magnetron sputtering method has been used for the efficient phase controlled synthesis of noble metal nanomaterials, especially Ag NPs¹⁶. This method employs a 50 mm-diameter Ag disc with a purity of 99.99% as the sputtering target, and both Ar and He as the sputtering gases under a pressure between 50 and 200 m Torr¹⁶. The Ag NPs can be deposited onto various kinds of substrates, such as glass, Si and stainless steel¹⁶. Importantly, the obtained Ag NPs with a size less than 30 nm demonstrate a 4H hexagonal structure (Figure 1-6), considering the Ag NPs usually crystallize in the common *fcc* structure¹⁶.

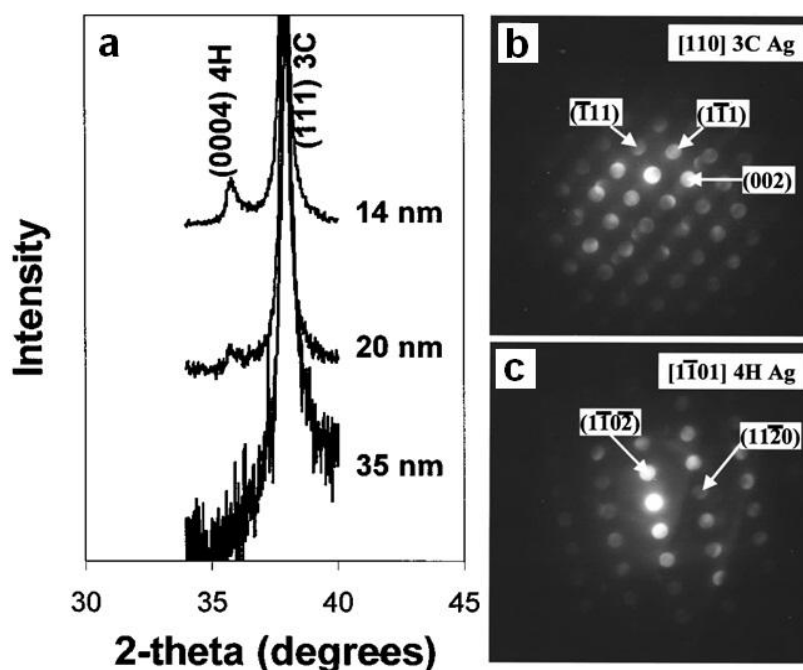


Figure 1-6. (a) XRD patterns of Ag NPs with different average sizes of 14 nm, 20 nm and 35 nm, respectively¹⁶. (b,c) SAED patterns taken from individual Ag nanoparticles with zone axes of $[110]_{3C}$ and $[110]_{4H}$, respectively¹⁶. Copyright 2001, American Physical Society.

The AAO-templated electrochemical deposition method has also been used for the phase controlled synthesis of Ag nanostructures^{14,17,67-70}. Typically, the porous

AAO templates with different pore sizes (from 10 nm to 100 nm) were firstly fabricated by modulating the anodization process and enlarging the pores. Then, the Ag nanowires were electrochemically deposited into the as-prepared porous AAO templates in aqueous AgNO_3 solution with alternating current (AC) under a constant voltage. After the electrochemical process, the porous AAO templates could be etched away in NaOH solution at ambient conditions to give the free-standing 4H Ag nanowires, coexisting with some 3C Ag nanowires as the by-products. In 2002, Zhu *et al.* firstly reported the successful synthesis of 4H Ag nanowires by using porous AAO as a hard template⁶⁷. Later, they found that the porous AAO templates with a pore size of about 30 nm favor the formation of 4H Ag nanowires with the highest concentration compared to that with a size of either > 30 nm or < 30 nm (Figure 1-7)¹⁷. The detailed theoretical calculations indicated that the 4H Ag nanowires have a much more favorable surface configuration but higher volume internal energy compared to the *fcc* counterparts¹⁷. Recently, Fei *et al.* showed that the introduction of tartaric acid and low-temperature during the porous AAO templated electrochemical deposition could further increase the yield of 4H Ag nanowires⁶⁸. Besides, Ayyub *et al.* found that, by controlling the kinetics of the electrochemical deposition, 3C, 4H, and 2H polytypes of Ag nanowires can be obtained at a constant electrochemical potential of 3 V, 200 mV and 2 mV, respectively⁶⁹.

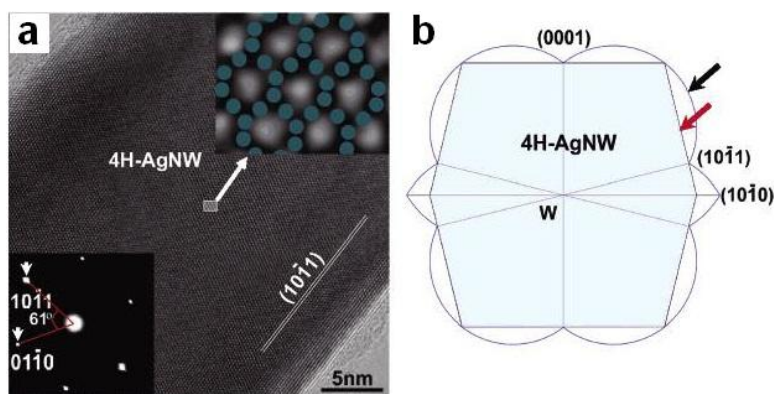


Figure 1-7. (a) Typical HRTEM image of a 4H Ag nanowire. Insets: the bottom-left inset shows the corresponding SAED pattern of the 4H Ag nanowire shown in (a); the top-right inset demonstrates the zoom-in image of the marked region in (a), which is overlaid with some green dots to indicate the atomic projection of 4H Ag nanowire paralleling to $[\bar{2}113]^{17}$. (b) The simulated cross section of a typical 4H Ag nanowire with the Wulff's construction and broken-bond rule, in which the surface of Ag nanowire is marked by a red arrow and enclosed by $\{10\bar{1}1\}$ and $\{0001\}$ planes, and the surface energy plot is marked by a black arrow¹⁷. Copyright 2006, American Chemical Society.

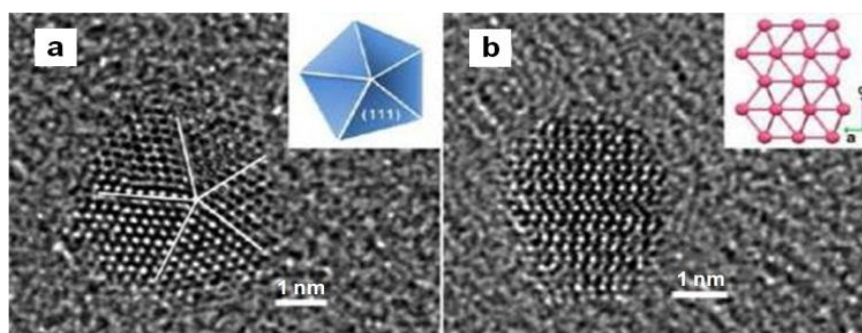


Figure 1-8. (a) Typical HRTEM image of a *fcc* Ru NP¹⁸. Inset: schematic illustration of the decahedral structure. (b) Typical HRTEM image of a *hcp* Ru NP¹⁸. Inset: schematic illustration of the *hcp* lattice observed along the $[100]$ direction. Copyright 2013, American Chemical Society.

The polyol method has been demonstrated as an effective strategy towards the synthesis of noble metal nanomaterials with different crystal structures¹⁸. This method involves the use of poly(N-vinyl-2-pyrrolidone) (PVP) and polyols (such as ethylene glycol (EG) and triethylene glycol (TEG)) with high boiling points as the stabilizing agents and solvents, respectively. After mixing the metal salts and PVP in the polyols, the growth solution is heated to reflux, resulting in the nucleation and growth of NPs. For instance, Kitagawa *et al.* have firstly reported the successful synthesis of *fcc* Ru NPs with a size ranging from 2.4 nm to 5.4 nm by using the polyol method¹⁸. Interestingly, they found that the metal precursor and solvent play an important role on the final structure of the obtained Ru NPs¹⁸. By using Ru(acac)₃ and TEG as the metal precursor and solvent, respectively, pure *fcc* Ru NPs were obtained¹⁸. In contrast, pure *hcp* Ru NPs were obtained when using the RuCl₃·nH₂O and EG as the metal precursor and solvent, respectively¹⁸.

Besides the aforementioned methods, Zhang *et al.* have recently developed a GO-templated synthesis approach for the phase controlled synthesis of noble metal nanomaterials, especially for the Au nanostructures^{19,71}. This method employs the GO sheets and oleylamine as the soft template and capping agents, respectively. After the GO, Au salts and oleylamine are mixed in a binary solvent of hexane/ethanol (v/v = 23/2), the mixture is heated in a 55 °C water bath for 16 h, leading to the nucleation and growth of pure *hcp* Au square sheets (AuSSs) with a thickness of about 2.4 nm on the GO sheets (Figure 1-9)¹⁹. The time-dependent experiments revealed that the GO sheets could help to induce the formation of square-like Au nanodot assemblies at the early stage¹⁹. After that, the AuSSs could be gradually formed via a process involving of oriented attachment and selective etching¹⁹. Importantly, it was found that the solvent system is crucial for the

synthesis of ultrathin Au nanostructures⁷¹. By simply changing the binary solvent system from the aforementioned hexane/ethanol to pure hexane, alternating *hcp*/*fcc* ultrathin Au nanowires with a diameter of about 1.6 nm can be obtained⁷¹.

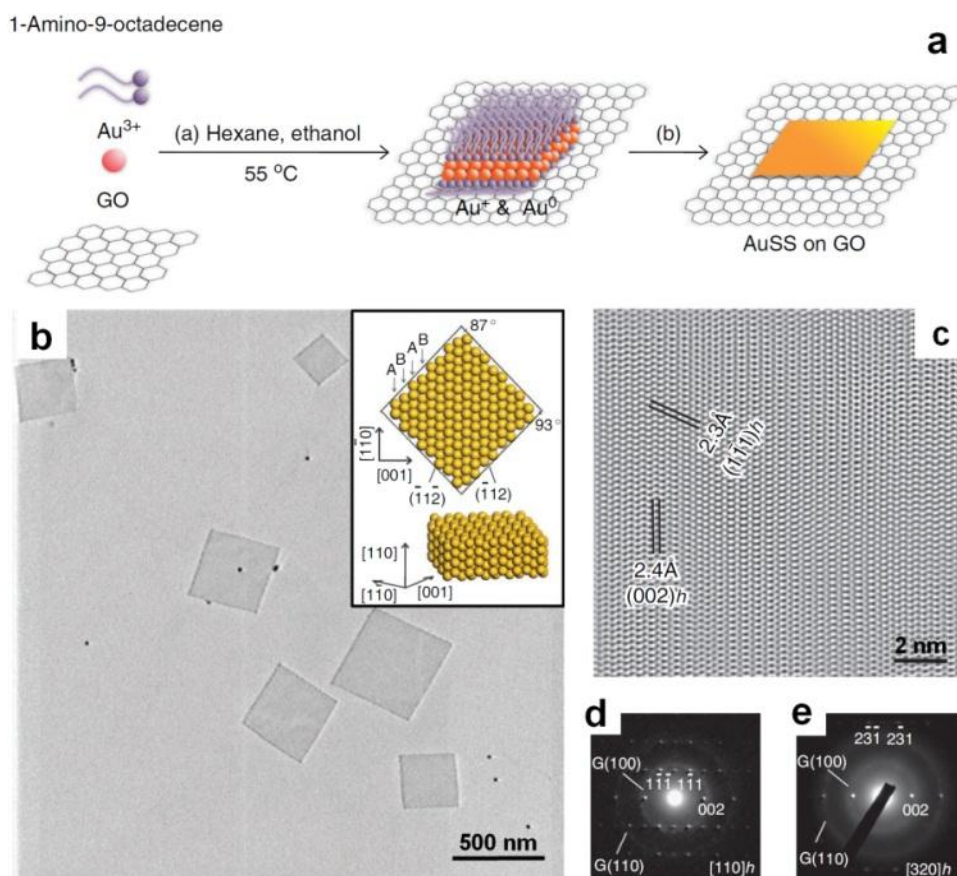


Figure 1-9. (a) Schematic illustration for the synthesis of *hcp* AuSSs on GO sheets¹⁹. (b) Typical TEM image of the obtained *hcp* AuSSs¹⁹. Inset: crystallography models of the *hcp* AuSSs. (c) HRTEM image of a typical *hcp* AuSS. (d,e) Typical SAED patterns of an *hcp* AuSS taken from the $[110]_h$ and $[320]_h$ zone axes, respectively¹⁹. Copyright 2011, Nature Publishing Group.

1.2.3 The Influence of Crystal Phase on Noble Metal Nanomaterials

Similar to the parameters of size and shape, the crystal phase can also greatly affect the chemical and physical properties of noble metal nanomaterials. Firstly, it has been shown that the chemical stability of noble metal nanostructures can be significantly influenced by altering their crystal structures^{13,63}. For instance, Sun *et al.* found that the stability of FePt NPs under strong acid conditions is greatly enhanced by simply changing their crystal structure from the common chemically disordered *fcc* phase to the chemically ordered *fcc* one (Figure 1-10a)¹³. Similarly, by changing the crystal structure of trimetallic FePtAu NPs from *fcc* to *fcc* phases, their chemical stability could also be greatly increased⁶³.

Meanwhile, the optical property of noble metal nanomaterials can also change greatly along with the variation of their crystal phases¹⁴. For instance, it was observed that the 4H Ag nanowire film shows a yellow color and demonstrates a much stronger LSPR absorption than that of the common *fcc* Ag nanowire film with a white color (Figure 1-10b)¹⁴. Moreover, the bulk plasmon absorption in 4H Ag is slightly blue shifted (about 5 nm) compared to that of the *fcc* Ag¹⁴. Interestingly, the low-frequency Raman spectra indicated that the 4H Ag nanowire shows a strong vibrational peak at 64 cm⁻¹, while the *fcc* Ag nanowire does not exhibit any peak in the low-frequency region¹⁴.

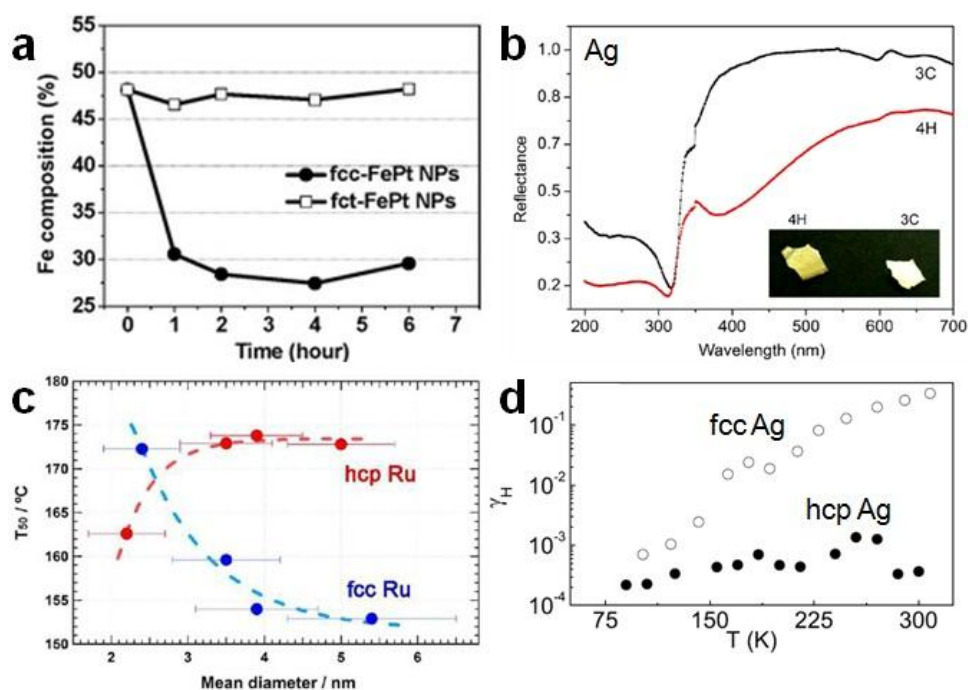


Figure 1-10. (a) The composition change of *fcc* and *fct* FePt NPs in 0.5 M H₂SO₄ solution at different times¹³. Copyright 2010, American Chemical Society. (b) The Ultraviolet-visible (UV-vis) reflectance spectra of 3C and 4H Ag films. Inset: Photographs of the 3C and 4H Ag films¹⁴. Copyright 2014, IOP Publishing Ltd. (c) The size-dependent temperature for 50% conversion of CO to CO₂ for the *fcc* and *hcp* Ru NPs¹⁸. Copyright 2013, American Chemical Society. (d) The change of Hooke parameter γ_H ($f = 1$ Hz) with temperature for the *fcc* (open circles) and *hcp* (filled circles) Ag nanowires⁷². Copyright 2008, American Institute of Physics.

Most importantly, the catalytic activity of noble metal nanomaterials can be significantly affected by their crystal structures^{13,18}. In 2010, it was reported that the catalytic activity of *fct* FePt NPs is almost 1.8 times of that of the *fcc* counterparts towards the oxygen reduction reaction (ORR) at the half-wave potential¹³. Later, it was shown that the catalytic activity of *fct* FePt NPs for ORR can be further increased via coating a thin layer of Pt shell, which will introduce a strain on the Pt shell because of the structure mismatch between the *fct* FePt core

and the *fcc* Pt shell, and thus increase their catalytic activity⁷³. Recently, it was found that, with the formation of *fcc*-FePt-Fe₃O₄ dumbbell, the initial *fcc* FePt NPs can be fully converted to the *fcc* FePt nanoparticles after thermal treatment⁷⁴. As a result, the fully ordered *fcc* FePt nanoparticles shows a much improved catalytic activity in comparison with the partially ordered counterparts⁷⁴. Similar to the aforementioned FePt nanoparticles, the structure change of FePtAu NPs from *fcc* to *fcc* phases also resulted in a big increase of their catalytic activity towards the formic acid oxidation reaction (FAOR)⁶³. Most recently, Kitagawa and coworkers found that the catalytic activity of Ru NPs towards CO oxidation increases with the increasing of particle size for the uncommon *fcc* polytype, while the catalytic activity decreases with increasing of particle size for the common *hcp* polytype (Figure 1-10c)¹⁸. Besides, the structure change induced catalytic activity variation has also been observed in the bimetallic CoPt and CuPt NPs^{59,60}.

In addition to the properties mentioned above, the structure transformation of noble metal nanomaterials can also lead to the change of their electrical and magnetic properties^{13,72}. For instance, the electrical noise in *hcp* Ag nanowires is far lower (up to several orders of magnitude) than that in the conventional *fcc* Ag nanowires⁷². Another study revealed that the 4H polytype of Ag nanowires demonstrates a relatively larger resistivity (19.9 $\mu\Omega$ cm) compared to that of the common *fcc* polytype (11.9 $\mu\Omega$ cm)⁷⁵. Besides the electrical property, by changing the structure of noble metal nanomaterials, their magnetic property can also be altered^{13,76,77}. Taking FePt as an example, it was reported that, by simply changing the crystal structure of FePt NPs from *fcc* to *fcc* phases, their magnetic properties would change from the superparamagnetic (coercivity is 0 Oe) to ferromagnetic (in-plane coercivity is 1800 Oe) types¹³.

1.2.4 Monochromated Electron Energy Loss Spectroscopy of Individual Noble Metal Nanostructures

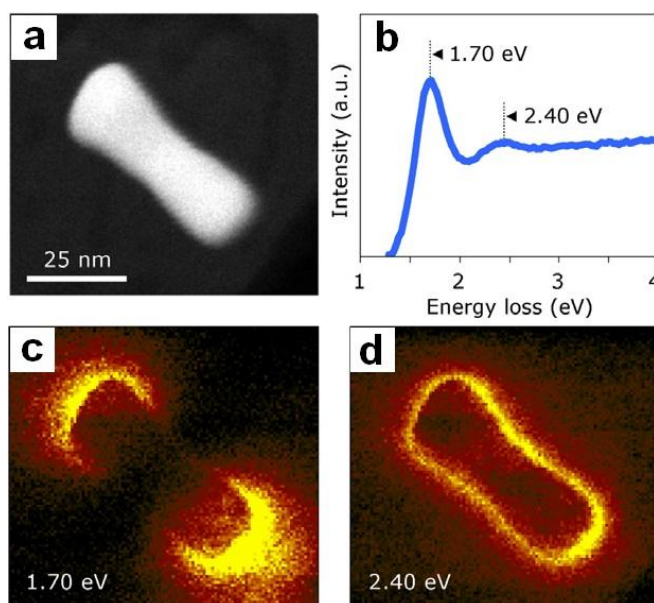


Figure 1-11. (a) Typical HAADF-STEM image of a concave Au nanorod²². (b) The average monochromated EELS spectrum of the Au nanorod after removing the zero-loss peak²². (c,d) The corresponding EELS maps of surface plasmon resonance intensity of the Au nanorod at 1.70 eV ($\lambda = 730$ nm) and 2.40 eV ($\lambda = 517$ nm), respectively²². Copyright 2007, IOP Publishing Ltd.

The intriguing optical properties of noble metal nanomaterials are derived from the excitation of LSPR, as shown in Figure 1-2b²⁷. The resonant energy and spatial distribution of LSPR modes are determined by the size, composition, shape and environment of noble metal nanomaterials²⁷. Conventionally, the optical properties of noble metal nanomaterials are studied by the far-field optical techniques that have remarkable spectral resolution⁵. However, the traditional optical techniques demonstrate relatively low spatial resolution, which is constricted by the light diffraction limit. Therefore, to investigate the complex

relationship between LSPR and structure of noble metal nanomaterials, monochromated electron energy loss spectroscopy (EELS) in scanning transmission electron microscopy (STEM), which combines both high spectral resolution and excellent spatial resolution on the nanometer scale, has recently been developed^{21,78,79}. Importantly, the monochromated EELS can probe all the LSPR modes of noble metal nanomaterials, including both bright and dark modes⁷⁹.

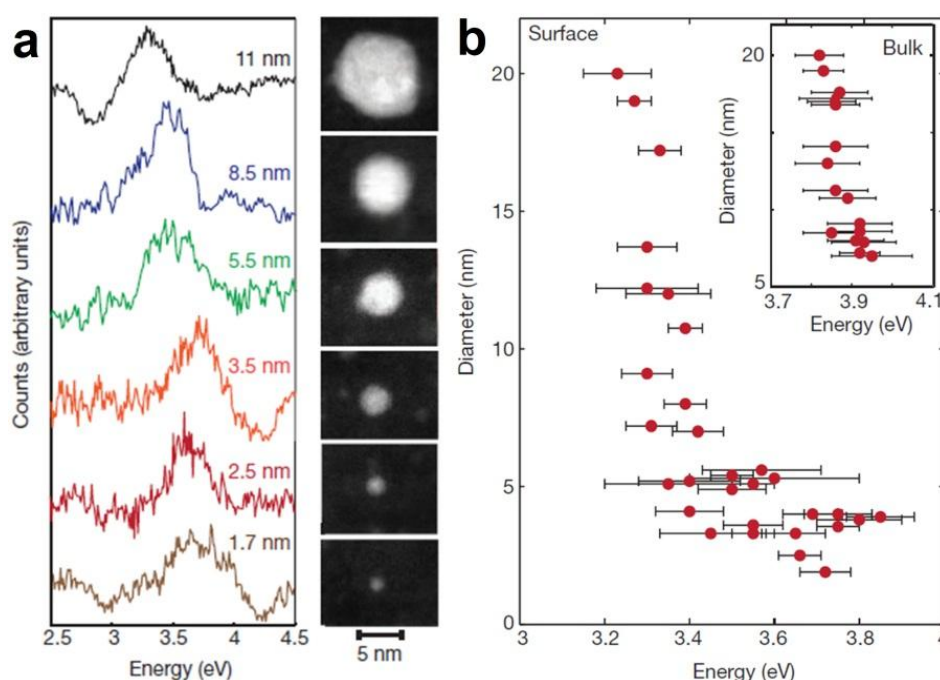


Figure 1-12. (a) The normalized monochromated EELS spectra and corresponding high-angle annular dark-field STEM (HAADF-STEM) images of Ag NPs with different sizes from 1.7 nm to 11 nm⁷⁸. (b) The plot of particle diameter of Ag NPs versus surface plasmon resonance energy⁷⁸. Inset: the plot of particle diameter of Ag NPs versus the bulk plasmon resonance energy. Copyright 2012, Nature Publishing Group.

In a typical experiment of monochromated EELS²⁰, the samples of noble metal nanomaterials is firstly deposited on the amorphous silicon nitride substrate with a

thickness of several tens of nanometers (e.g. 30 nm), which has a band gap of about 4 eV and thus are optically transparent in the range from 0 eV to 4 eV. Then the sample is loaded into the STEM with a holder. After that, the focused electron beam is located a few nanometers next to the sample to excite the LSPR and detect the EELS of noble metal nanomaterials.

To date, by using the monochromated EELS, the optical properties of various kinds of noble metal nanomaterials with different sizes, shapes and compositions have been studied^{22,78,80-83}. For instance, by using new techniques in EELS imaging and spectral processing, Michel *et al.* have mapped the LSPR response of individual Au nanorods (Figure 1-11) with a spatial resolution of approximately one order of magnitude higher compared to that of the scanning near-field optical microscope²². Importantly, the measured surface plasmon resonance energies of Au nanorods with EELS match well with previous calculations, and the mappings clearly demonstrate the well-defined plasmon intensity distribution of both the longitudinal and transverse modes (Figure 1-11)²². Recently, Dionne and coworkers have systematically investigated the surface plasmon resonance of individual Ag NPs with ultrasmall sizes ranging from 20 nm to less than 2 nm by using the monochromated EELS in the STEM mode (Figure 1-12)⁷⁸. Significantly, it was found that surface plasmon resonance energy demonstrates a blue-shift of as large as 0.5 eV along with the size decreasing from 20 nm to less than two nanometers (Figure 1-12b), which reveals the quantum plasmonic properties of ultrasmall noble metal NPs⁷⁸.

1.2.5 Short Summary

In this section, the unique properties and phase controlled synthetic methods of noble metal nanomaterials have been concisely reviewed. Most of existing synthetic strategies have exhibited limitations, e.g. high temperature, high pressure, high vacuum and multiple steps. Therefore, in order to achieve a better phase controlled synthesis of noble metal nanomaterials, the development of facile and low cost synthetic approaches that are conducted under mild conditions is urgent and important. Meanwhile, the influence of crystal phase on the physical and chemical properties of noble metal nanomaterials is also reviewed, which suggests the phase controlled synthesis may greatly improve or even completely change the remarkable properties of noble metal nanomaterials. Besides, the monochromated EELS study of individual noble metal nanomaterials has also been briefly reviewed.

CHAPTER 2 AIMS AND MOTIVATION

2.1 Objectives and Scope

Because of the importance of noble metal nanomaterials and the limitations of existing synthetic methods, this project aims to develop new routes for synthesis of novel noble metal nanomaterials with controlled crystal structure, and simultaneously to investigate their unusual physical and chemical properties.

To realize the aforementioned objectives, the following works are executed in this project. Firstly, ligand exchange is used to synthesize face-centered cubic (*fcc*) Au square sheets (AuSSs) from hexagonal close-packed (*hcp*) AuSSs. Secondly, a simple metal coating method is well developed to prepare a series of noble bimetallic nanosheets, such as *fcc* and *hcp/fcc* Au@Ag square sheets, *fcc* Au@Pt and Au@Pd rhombic sheets. Thirdly, a colloidal synthetic method is established to favor the nucleation and growth of 4H hexagonal Au nanoribbons. To study their morphology, crystal phase and chemical composition, the obtained new noble metal nanomaterials are thoroughly characterized by transmission electron microscopy (TEM), aberration-corrected scanning TEM (STEM), atomic force microscopy (AFM), X-ray diffraction (XRD), and X-ray photoelectron spectroscopy (XPS).

2.2 Hypothesis

Based on the works proposed above, the following hypotheses have been made.

Firstly, in the process of ligand exchange, the surface energy of *hcp* AuSSs can be dramatically changed because of the much stronger interaction between Au and thiol molecules compare to that between Au and oleylamine molecules. Due to the large surface area-to-volume ratio, the surface energy of inorganic nanomaterials cannot be neglected and may even dominate in the total systemic energy. According to the previous studies on the phase stability of inorganic nanomaterials, the crystal structure of *hcp* AuSSs might be modulated by adjusting its surface energy, which can be achieved by simply tuning the surface capping agents.

Secondly, metal coating on the *hcp* AuSSs, similar to that of the aforementioned ligand exchange process, can also change its surface energy via the increase of thickness and formation of metal bonds. Meanwhile, it has been previously revealed that the epitaxial stain between two materials can result in unusual physical and chemical phenomena. Therefore, via the solution epitaxial growth of other noble metals on *hcp* AuSSs, novel Au-based bimetallic nanomaterials with unique morphology and structure might form.

Lastly, colloidal synthetic method has been broadly applied for the shape and phase control of various kinds of inorganic nanomaterials. Previous reports suggest that crystal structures of inorganic nanomaterials can be modulated by modulating the experimental conditions, such as solvent system, temperature or pressure, in the colloidal synthesis. Very recently, our group firstly reported the synthesis of *hcp* AuSSs by heating a mixture of oleylamine and HAuCl_4 in a binary solvent system of hexane and ethanol. Therefore, by changing the solvent system in the

synthesis of *hcp* AuSSs, novel Au nanomaterials with unprecedented crystal structure might be achieved.

CHAPTER 3 EXPERIMENTAL DETAILS

3.1 Chemicals and Materials

Natural graphite (SP-1) was bought from Bay Carbon (Bay City, MI, USA). Gold(III) chloride hydrate ($\text{HAuCl}_4 \cdot \text{aq}$, Au basis $\sim 50\%$), silver nitrate (AgNO_3 , $\geq 99.0\%$), chloroplatinic acid hexahydrate ($\text{H}_2\text{PtCl}_6 \cdot 6\text{H}_2\text{O}$, Pt basis $\geq 37.5\%$), palladium chloride (PdCl_2 , $\geq 99.9\%$), oleylamine (70%, technical grade), KMnO_4 , concentrated H_2SO_4 (98%), H_2O_2 (30%), L-ascorbic acid (BioXtra, $\geq 99.0\%$, crystalline), octadecanethiol (ODT, 98%), octylamine (99%), 1-dodecanethiol (DDT, $\geq 98\%$), 1-propanethiol (PT, 99%), 1-octanethiol (OT, 98.5%), 6-mercapto-1-hexanol (MHO, 97%), 11-mercapto-1-undecanol (MUDO, 98%), 3-mercaptopropionic acid (MPA, $\geq 99\%$), 11-mercaptopundecanoic acid (MUDA, 95%), benzeneethanethiol (BET, 98%), 1,6-hexanedithiol (HdT, $\geq 97\%$), 1,2-dichloropropane (99%), chloroform ($\geq 99.5\%$), and the other chemicals used in the experiments without special mention were bought from Sigma-Aldrich. Ethanol (99.9%, absolute) and concentrated hydrochloric acid (HCl , $\sim 37\%$) were purchased from Merck. H_2PdCl_4 stock solution (8.0 mM, in ethanol) was prepared by mixing PdCl_2 powder with concentrated HCl in ethanol. Sodium borohydride (NaBH_4 , $\geq 99.0\%$) was bought from Fluka. All the chemicals were directly used without further purification. De-ionized water was used throughout the experiments.

3.2 Ligand Exchange Mediated Synthesis of Face-Centered Cubic Au Square Sheets

3.2.1 Synthesis of Graphene Oxide

Single-layer graphene oxide (GO) sheets were synthesized from natural graphite by a modified Hummers method⁸⁴. Typically, 0.6 g graphite powder was added into a mixture of 4.8 mL concentrated H₂SO₄ (98%), 1.0 g P₂O₅ and 1.0 g K₂S₂O₈, and then the solution was maintained at 80 °C for 4.5 h. The obtained preoxidized products were washed by water and dried. After the preoxidized products were added into 24 mL H₂SO₄ (98%), followed by slowly adding 3.0 g KMnO₄ with temperature maintained below 20 °C so as to avoid overheating and explosion, the temperature of the solution was gradually increased to 35 °C and kept for 2 h. Then 50 mL H₂O was added to dilute the mixture in an ice-water bath. After 2 h, 140 mL H₂O was added to further dilute the solution, followed by injecting 4 mL H₂O₂ (30%) in the solution to remove the excess KMnO₄, the color of the solution changed to bright yellow. After that, the as-prepared product was successively washed by HCl and H₂O, and the isolated single-layer GO was obtained. The obtained GO sheet was dispersed in ethanol (0.2 mg/mL) by sonication.

3.2.2 Synthesis of Hexagonal Close-Packed Au Square Sheets on GO Sheets

The hexagonal close-packed (*hcp*) Au square sheet (AuSS) was synthesized according to our previously reported approach with a slight adjustment¹⁹. In a typical experiment, 200 µL GO sheet solution (0.2 mg/mL, in ethanol) was centrifuged, and re-dispersed in a 2 mL growth solution consisted of HAuCl₄ (7.25 mM) and oleylamine (150 mM) in a binary solvent of ethanol and hexane (1/7, v/v).

After that, the 2 mL solution in a sealed glass bottle was heated at 58 °C for 16 h in a water bath. The as-prepared products were collected with centrifugation (5,000 rpm, 5 min), washed with hexane for another four times, and re-dispersed into hexane (2.0 mL). The concentration of Au atoms in the as-prepared *hcp* AuSS solution is about 4.6 mM.

3.2.3 Ligand Exchange on Hexagonal Close-Packed Au Square Sheets

Equal volumes of the aforementioned *hcp* AuSS solution and a freshly prepared thiol (such as DDT, ODT, PT, OT, MHO, MUDO, MUDA, BET, HdT, and MPA) solution (50 mM, in hexane) were mixed with each other, and then vortexed for 5 min under ambient conditions. After that, the final products were collected by centrifugation (7,000 rpm, 1 min), and then washed by hexane for twice. The as-prepared product was re-dispersed into hexane for future characterizations. In order to evaluate the influence of thiol concentrations, ODT solution with various concentrations ranging from 2 mM to 200 mM were applied for ligand exchange on *hcp* AuSSs.

3.2.4 Fabrication of Cross-Section Samples of Face-Centered Cubic Au Square Sheets

Cross-section samples of face-centered cubic (*fcc*) AuSSs were fabricated on an FEI Nova NanoLab 600i focused-ion beam (FIB)/scanning electron microscopy (SEM) dual-beam system. Briefly, the *fcc* AuSS solution was first dropped on a Si substrate and dried at ambient conditions. After the sample was loaded in the chamber of SEM, a typical *fcc* AuSS of interest was positioned and rotated to make one of the two diagonals parallel to the horizontal x-axis of SEM. Then a

thin layer of W was pre-deposited on the region of interest with e-beam induced coating. After that, two alignment marks were made to locate the exact position of the interested region before the successive coating of a thick W layer with FIB. Then, the interested area was cut from the Si substrate and transferred to a transmission electron microscopy (TEM) half-grid with an in-situ manipulator. Finally, the sample was milled with FIB to a certain thickness.

3.2.5 Localized Surface Plasmon Resonance Study of Individual Face-Centered Cubic Au Square Sheets

Monochromated electron energy loss spectroscopy (EELS) characterization of individual *fcc* AuSSs was conducted in the scanning TEM (STEM) mode on an FEI Titan TEM with Schottky electron source, which is operated at a voltage of 80 kV, using convergence and collection semiangles of 13 mrad. Diameter of the applied electron probe was about 1 nm and an energy resolution of 170 meV was achieved by using a Wien-type monochromator. As a result, an EELS spectrum was collected from a single AuSS on GO sheets, by positioning the incident focused electron beam next to (2–3 nm) the single AuSS to excite and detect its LSPR. A control spectrum was acquired about 500 nm away from the AuSS, with only GO sheet present, and did not excite the localized surface plasmon resonance (LSPR) of the single AuSS. The acquisition time was selected as 1 s so as to avoid the influence of organic contaminations. As the acquisition time is relatively short, the resulted signal-to-noise ratio of obtained EELS spectra is rather low.

3.3 Metal Coating Assisted Synthesis of Novel Bimetallic Nanosheets

3.3.1 Synthesis of Face-Centered Cubic Au@Ag Square Sheets

The *fcc* Au@Ag square sheet was synthesized via coating of Ag onto the aforementioned *hcp* AuSSs by using ascorbic acid (or NaBH₄) as the reductant. In a typical experiment, 350 μ L ethanol and 50 μ L AgNO₃ solution (4 mM, in ethanol) were successively added into 500 μ L *hcp* AuSS solution. The mixed solution was mildly shaken and cooled in an ice-water bath. Then, 100 μ L ascorbic acid solution (1 mM, in ethanol) was added in the aforementioned mixed solution, followed by mild shaking. After that, the solution was maintained undisturbed for 2 h in an ice-water bath. The final products were collected with centrifugation (8,000 rpm, 1 min), cleaned once by hexane and then re-dispersed in hexane.

3.3.2 Synthesis of Hexagonal Close-Packed/Face-Centered Cubic Au@Ag Square Sheets

The *hcp/fcc* Au@Ag square sheet was synthesized via coating of Ag on the aforementioned *hcp* AuSS by using oleylamine as the reductant. In a typical experiment, 133 μ L oleylamine, 230 μ L ethanol, 20 μ L AgNO₃ solution (20 mM, in ethanol), and 620 μ L hexane were successively added into 1.0 mL *hcp* AuSS solution. After that, a glass bottle containing the aforementioned mixed solution was sealed, and then heated at 38 °C for 20 h in a water bath. The final products were collected with centrifugation (5,000 rpm, 2 min), cleaned twice by hexane and re-dispersed in hexane.

3.3.3 Synthesis of Face-Centered Cubic Au@Pt Nanosheets

The *fcc* Au@Pt nanosheet was synthesized via coating of Pt on the aforementioned *hcp* AuSSs by using NaBH₄ as reductant. In a typical experiment, 375 μ L hexane, 540 μ L ethanol, 60 μ L NaBH₄ solution (20 mM, in ethanol), and 100 μ L H₂PtCl₆ solution (2 mM, in ethanol) were successively added into 125 μ L *hcp* AuSS solution. After that, the mixed solution was gently shaken and maintained undisturbed at ambient conditions for 3 h. The final products were collected with centrifugation (8,000 rpm, 1 min), cleaned once by hexane and re-dispersed in hexane. The majority of final product (> 90%) is the *fcc* Au@Pt rhombic nanosheets, while the minority of final product (< 10%) is the *fcc* Au@Pt square nanosheets.

3.3.4 Synthesis of Face-Centered Cubic Au@Pd Nanosheets

The *fcc* Au@Pd rhombic nanosheet was synthesized via coating of Pd on the aforementioned *hcp* AuSS by using NaBH₄ as reductant. In a typical experiment, 375 μ L hexane, 590 μ L ethanol, 60 μ L NaBH₄ solution (20 mM, in ethanol), and 50 μ L H₂PdCl₄ solution (4 mM, in ethanol) were successively added in 125 μ L *hcp* AuSS solution. After that, the mixed solution was gently shaken and maintained undisturbed at ambient conditions for 3 h. The final products were collected with centrifugation (10,000 rpm, 1 min), cleaned once by hexane and re-dispersed in hexane. The majority of final product (> 90%) is the *fcc* Au@Pd rhombic nanosheets, while the minority of final product (< 10%) is the *fcc* Au@Pd square nanosheets.

3.3.5 Fabrication of Cross-Section Samples of Face-Centered Cubic Au@Ag Square Sheets

The cross-section sample of *fcc* Au@Ag square sheets was fabricated on an FEI Nova NanoLab 600i FIB/SEM dual-beam system. Briefly, the *fcc* Au@Ag square sheet solution was firstly dropped on a Si substrate and then dried at ambient conditions. After the aforementioned sample was loaded in the chamber of SEM, a typical *fcc* Au@Ag square sheet was positioned and rotated to make one of the two diagonals parallel to horizontal x-axis of SEM. Then a layer of W was pre-deposited on the interested region with e-beam induced coating. After that, two alignment marks were prepared to locate exact positions of the interested regions before further coating of a thick W layer with FIB. Then the interested area was cut from the Si substrate and transferred to a TEM half-grid with an in-situ manipulator. Finally, the sample was milled to a certain thickness with FIB.

3.3.6 Fabrication of Cross-Section Samples of Hexagonal Close-Packed/Face-Centered Cubic Au@Ag Square Sheets

The cross-section sample of *hcp/fcc* Au@Ag square sheet was fabricated on an FEI Helios NanoLab 400S FIB/SEM dual-beam system. Two cross-section samples of the *hcp/fcc* Au@Ag square sheet are fabricated by cutting along the $[001]_h/[\bar{1}\bar{1}1]_f$ and $[1\bar{1}0]_h/[\bar{1}\bar{2}1]_f$ directions, respectively. In a typical experiment, the *hcp/fcc* Au@Ag square sheet solution was first dropped on a Si substrate and then dried at ambient conditions. After the sample was loaded in the chamber of SEM, a typical *hcp/fcc* Au@Ag square sheet was positioned and then rotated to make one of the two diagonals (unequal to each other) parallel to horizontal x-axis of SEM. Then a layer of C was coated on the interested area with e-beam induced coating.

After that, two alignment marks were prepared to locate exact positions of the interested regions before successive coating of a thick layer of Pt with FIB. Then the interested area was cut from the Si substrate and transferred to a TEM half-grid with an in-situ manipulator. Finally, the sample was milled to a certain thickness with FIB.

3.3.7 Fabrication of Cross-Section Samples of Face-Centered Cubic Au@Pt Rhombic Nanosheets

Cross-section lamellas of *fcc* Au@Pt rhombic nanosheet were prepared using a FIB/SEM dual-beam system. The Au@Pt rhombic nanosheet solution was first dropped on a Si substrate and then dried at ambient condition. After the aforementioned sample was inserted in the chamber of SEM, a typical Au@Pt rhombic nanosheet was located and rotated to make its long diagonal parallel to horizontal x-axis of SEM. A thin layers of C (or W) and Pt were then successively coated onto the interested region with e-beam induced coating, and two alignment marks were prepared to locate exact positions of interested regions before further coating of a thick Pt (or W) layer with FIB. Then the interested area was cut from the Si substrate and transferred to a TEM half-grid with an in-situ manipulator. Finally, the sample was milled to a certain thickness with FIB.

3.3.8 Localized Surface Plasmon Resonance Study of Individual Face-Centered Cubic Au@Ag Square Sheets

Monochromated EELS characterization of individual *fcc* Au@Ag square sheets was carried out in the STEM mode on an FEI Titan TEM with Schottky electron

source, which was operated at a voltage of 80 kV, using convergence and collection semiangle of 13 mrad. Diameter of the applied electron probe was about 1 nm, and an energy resolution of 170 meV was achieved by using a monochromator of Wien-type. As a result, EELS spectra were collected from individual Au@Ag square sheets on GO sheets, by locating the focused incident electron beam next to (2–3 nm) the single Au@Ag square sheet to excite and detect the LSPR. A control spectrum was acquired about 500 nm away from the Au@Ag square sheets, with merely GO sheet present, and did not excite the LSPR of individual Au@Ag square sheets. Acquisition time was chosen as 1 s so as to avoid the influence of organic contaminations. As acquisition time is relatively short, the resulted signal-to-noise ratio of obtained EELS spectra is rather low.

3.4 Colloidal Synthesis of 4H Hexagonal Au Nanoribbons

3.4.1 Synthesis of 4H Au Nanoribbons

In a typical experiment, 4.08 mg HAuCl_4 and 220 μL oleylamine were added into a binary solvent of 3.54 mL hexane and 250 μL 1,2-dichloropropane. Then the mixture in a sealed glass bottle was heated at 58 °C for 16 h in a water bath. After that, the final products were collected with centrifugation (5,000 rpm, 1 min), washed at least three times with hexane and re-dispersed into hexane (4 mL).

3.4.2 Ligand Exchange on 4H Au Nanoribbons

In a typical experiment, 300 μL 4H Au nanoribbon (NRB) solution was centrifuged (5,000 rpm, 1 min) and re-dispersed into 300 μL chloroform. A freshly

prepared DDT solution (0.8 M, in chloroform) was then added and vortexed for about 5 min at ambient conditions. After that, the final products were collected with centrifugation (6,000 rpm, 1 min), cleaned twice by hexane and re-dispersed in hexane. It is worth to mention that DDT used here can be replaced by other thiols, e.g. PT and HdT.

3.4.3 Synthesis of Polytypic 4H/Face-Centered Cubic Au@Ag Nanoribbons

The 4H/*fcc* Au@Ag NRB was synthesized via the epitaxial growth of Ag on 4H Au NRBs with oleylamine as reductant. In a typical experiment, 130 μL oleylamine, 250 μL AgNO_3 solution (50 mM, in ethanol), and 1.14 mL hexane were successively added into 0.5 mL 4H Au NRB solution. Then the mixture in a sealed glass bottle was heated at 58 $^{\circ}\text{C}$ for 20 h in a water bath. The final products were collected with centrifugation (5,000 rpm, 1 min), washed twice by hexane and re-dispersed in hexane.

3.4.4 Synthesis of Polytypic 4H/Face-Centered Cubic Au@Pd Nanoribbons

Firstly, 250 μL 4H Au NRB solution was centrifuged (5,000 rpm, 1 min) and re-dispersed into 250 μL chloroform. The 4H/*fcc* Au@Pd NRB was synthesized via the epitaxial growth of Pd on 4H Au NRBs by using NaBH_4 as the reductant. In a typical experiment, 250 μL chloroform, 390 μL ethanol, 50 μL H_2PdCl_4 solution (8 mM, in ethanol), and 60 μL NaBH_4 solution (20 mM, in ethanol) were successively added into 250 μL 4H Au NRB solution. Then the mixture was gently shaken and kept undisturbed at ambient conditions for 1 h. The final products were

collected with centrifugation (5,000 rpm, 1 min), cleaned once by hexane and re-dispersed in hexane.

3.4.5 Synthesis of Polytypic 4H/Face-Centered Cubic Au@Pt Nanoribbons

Firstly, 250 μL 4H Au NRB solution was centrifuged (5,000 rpm, 1 min) and re-dispersed into 250 μL chloroform. The 4H/fcc Au@Pt NRB was synthesized via the epitaxial growth of Pt on 4H Au NRBs by using NaBH_4 as the reductant. In a typical experiment, 250 μL chloroform, 340 μL ethanol, 100 μL H_2PtCl_6 solution (8 mM, in ethanol), and 60 μL NaBH_4 solution (20 mM, in ethanol) were successively added into 250 μL 4H Au NRB solution. Then the mixture was gently shaken and kept undisturbed at ambient conditions for 1 h. The final products were collected with centrifugation (5,000 rpm, 1 min), cleaned once by hexane and re-dispersed in hexane.

3.4.6 Localized Surface Plasmon Resonance Study of Individual 4H Au Nanoribbons

The monochromated EELS measurement of single Au NRB was carried out in the STEM mode using an FEI Titan TEM with Schottky electron source, which is operated at a voltage of 80 kV, using an EELS collection semiangle of 16 mrad and a convergence semiangle of 13 mrad. Diameter of the electron probe was about 1–2 nm. The energy resolution was set to about 0.1 eV (as full-width at half-maximum value), using a monochromator of Wien-type. The EELS spectroscopy and map were collected with a Gatan Tridiem ER EELS detector. The monochromated EELS was taken with a modified binned gain averaging acquisition routine²¹, to give improved signal-to-noise ratio for the relatively weak

plasmon signal from few-nm thick Au NRB. The background signal was taken from the bare amorphous SiN_x, fitted to and subtracted from experimental EELS spectra. The EELS maps plotted the loss signal integrated over an energy window of 0.05 eV, centered around selected LSPR peaks.

3.4.7 Density Functional Theory Computational Details

The dielectric function of 4H Au thin film is calculated by first principle calculations based on the optical package of WIEN2k⁸⁵⁻⁸⁷. This package allows us to calculate the dipole matrix elements for transitions between intraband and interbands within the random phase approximation. The spin orbit interactions are taken into consideration in all calculations. In order to increase the accuracy of the optical properties, we used a very high k-mesh of 40×40×1 for the computation.

3.4.8 Finite-Element-Method Simulation

The swift electron-driven excitation of plasmons in individual 4H Au NRBs was simulated using the finite-element-method (FEM) in COMSOL Multiphysics RF module. The Au NRB was modeled as a perfect cuboid with the dimensions extracted from STEM image of the sample (length: 840 nm, width: 20 nm, and thickness: 4 nm). The frequency-dependent dielectric function of Au was taken from a handbook⁸⁸.

The electron beam was modeled in the framework of classical electrodynamics^{79,89} as an infinitely long broadband current $J_z(\omega)$ propagating in the z-direction with the radius of 1 nm corresponding to the kinetic energy of 80 keV. In our model, the beam was located at 105 nm (i.e. position “T”), 210 nm (i.e.

position “II”), 315 nm (i.e. position “III”) and 420 nm (i.e. position “IV”) away from one end of the Au NRB. The surrounding medium was air/vacuum with $\epsilon = 1$. The 30 nm-thick Si_3N_4 substrate was ignored in the simulation setup.

The electromagnetic field distribution was obtained by solving 3D Maxwell’s equations in the frequency domain. The power lost by electron beam in the excitation of wave perturbations with frequency ω was calculated as the integral over the beam volume V ,

$$P(\omega) = \int_V \mathbf{J}(\omega) \cdot \mathbf{E}(\omega) dV, \quad (1)$$

where $\mathbf{E}(\omega)$ is the calculated distribution of electric field. Finally, the electron loss probability⁷⁹,

$$\Gamma = P(\omega)/\hbar\omega, \quad (2)$$

versus photon energy $\hbar\omega$ is compared with the EELS spectrum.

3.5 Characterizations

3.5.1 Transmission Electron Microscopy

TEM was operated at a constant voltage (200 keV) with either a JEOL JEM-2010 or JEM 2100F instruments. The TEM sample was prepared by dropping about 5 μL sample solution on copper grid (200 mesh) with full carbon-coating and then dried at ambient condition.

3.5.2 Aberration-Corrected Transmission Electron Microscopy

The aberration-corrected high-resolution scanning TEM (STEM) was conducted on an FEI Titan Cubed S-Twin TEM operated at 300 kV. To achieve better spatial resolution, probe Cs corrector was applied. Briefly, high-resolution STEM imaging was performed at a 20 $\mu\text{s}/\text{pixel}$ scanning rate with spot size 7, 50 μm C2 aperture, 146 mm camera length, and a high-angle annular dark-field (HAADF) detector. In this way, a spatial resolution of about 1.0 \AA was obtained.

The aberration-corrected high-resolution TEM (HRTEM) images were acquired using the negative spherical aberration (C_s) imaging (NCSI) technique on TEAM 0.5, which is equipped with a high-brightness Schottky-type field emission gun and a monochromator of Wien-filter. The accelerating voltage was set to 80 kV. The lens aberrations were measured and compensated prior to the image acquisition by evaluating the Zemlin tableau of an amorphous carbon area on the grid, which is close to the area of interest in the specimen. According to the measurements, the residual lens aberrations were listed below: $C_s \sim -13 \mu\text{m}$, three-fold astigmatism $A2 < 40 \text{ nm}$, two-fold astigmatism $A1 < 2 \text{ nm}$, axis coma $B2 < 30 \text{ nm}$.

3.5.3 X-Ray Diffraction

The X-ray diffraction (XRD) pattern was collected on an X-ray diffractometer (Shimadzu thin film, XRD-6000) operated at 40 kV and 30 mA, using the $\text{CuK}\alpha$ radiation. The XRD sample was prepared by dropping a concentrated sample solution on a glass substrate and then dried at ambient conditions.

3.5.4 Atomic Force Microscopy

The atomic force microscopy (AFM) image was acquired with a scanning line of 512 and scanning rate of 1 Hz on a Dimension 3100 AFM (Veeco, USA), NSCRIPTOR system with a Si tip (spring constant: 42 N/m; resonance frequency: 320 kHz) in the tapping mode at ambient condition.

3.5.5 X-ray Photoelectron Spectroscopy

The X-ray photoelectron spectroscopy (XPS) data was acquired on either a Theta Probe electron spectrometer (ESCA-Lab-200i-XL, Thermo Scientific) or an AXIS ultra spectrometer (Kratos). The XPS sample was prepared by dropping the sample solutions on Si/SiO_x substrates and dried at ambient conditions.

CHAPTER 4 RESULTS AND DISCUSSIONS

4.1 Ligand Exchange Mediated Synthesis of Face-Centered Cubic Au Square Sheets

4.1.1 Introduction

During the past two decades, the inorganic nanomaterial have been intensively explored due to their promising applications in energy conversion⁹⁰, catalysis⁶, surface enhanced Raman scattering (SERS)², etc. The chemical and physical properties of inorganic nanomaterials can be modulated by tuning their shape, topology, size, and composition^{2,23}. Besides, the crystal structure of inorganic nanomaterials can also greatly influence their functional properties, e.g. optical⁹¹, magnetic^{9,92}, electrical⁹³ and catalytic properties¹³. For example, the structure change of FePt nanoparticles (NPs) from face-centered cubic (*fcc*) to face-centered tetragonal (*fcc*) phases resulted in the improved stability and catalytic activity for the oxygen reduction reaction (ORR)¹³. Hence the investigation of crystal structures and phase transitions of inorganic nanomaterials is critical to their shape and phase controlled synthesis, and potential applications.

Typically, the structure change of inorganic nanomaterials is achieved at high temperature^{9,13,94} or high pressure^{15,65,91,95}. Moreover, the electron-beam induced structure changes have been found, e.g. the phase change from the low-chalcocite to the high-chalcocite structures in Cu₂S nanorods⁹⁶. In addition, cation exchanges have been applied for the phase modulation of the inorganic nanomaterials⁹⁷⁻⁹⁹. But the compositions of original nanomaterials are altered during the process of cation exchange. Take CdSe as an example, the hexagonal CdSe nanostructures

were changed to the cubic Ag₂Se nanostructures after the cation exchange of Cd²⁺ with excess Ag⁺ ions⁹⁷. It should be noted that, below a certain size, when surface energy of a nanomaterial dominates total systemic energy, solvent molecules or ligand can greatly manipulate its crystal phase^{100,101}. For instance, the surface region of 3 nm ZnS NPs prepared in the methanol undergoes a phase change from the irregular state to regular cubic phase upon its capping by water molecules¹⁰¹. But it still remains a huge challenge to achieve the complete phase change of a nanomaterial from one crystal structure to another under ambient condition.

The phase change of metals with close-packed crystal structures (such as hexagonal close-packed (*hcp*) and *fcc*) has been extensively investigated both theoretically and experimentally¹⁰²⁻¹⁰⁴. The *fcc* and *hcp* polymorphs are different from the stacking order of the close-packed planes with the repeated ABC stacking along the [111]_f direction and AB stacking along the [001]_h direction, respectively. Usually, the *hcp*-to-*fcc* phase transition in metals, such as the phase change of Co occurs upon heating, is achieved by the movement of partial dislocation on the closed-packed plane, resulting in the formation of twins/stacking faults, or the coexisting of alternative *fcc* and *hcp* phases^{102,103}. So far, other kind of phase transition pathway or mechanism between *fcc* and *hcp* phases has scarcely been found in the noble metals¹⁰⁵.

Very recently, Huang *et al.* prepared thin Au square sheet (AuSS) with an uncommon *hcp* structure that is stable under ambient condition¹⁹. In this section, a simple ligand exchange approach has been developed to induce the phase change of AuSSs from *hcp* to *fcc* phases under ambient condition, resulting in the formation of ultrathin *fcc* AuSSs with a unique orientation of (100)_f. The crystallinity of the obtained *fcc* AuSS can be finely modulated by changing the

concentration of thiol molecules. Importantly, various kinds of thiol molecules can realize the formation of *fcc* AuSSs from *hcp* AuSSs at ambient conditions. Furthermore, the localized surface plasmon resonance (LSPR) absorption property of individual *fcc* AuSSs on graphene oxide (GO) is investigated with monochromated electron energy loss spectroscopy (EELS).

4.1.2 Synthesis and Characterization of Face-Centered Cubic Au Square Sheets

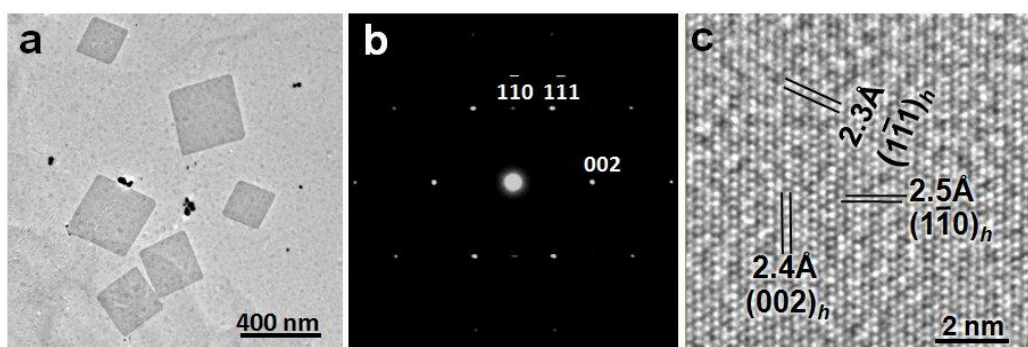


Figure 4-1. (a) TEM image of *hcp* AuSSs prepared on GO sheets. (b) SAED pattern of an *hcp* AuSS collected along $[110]_h$ zone axis. (c) HRTEM image of an *hcp* AuSS.

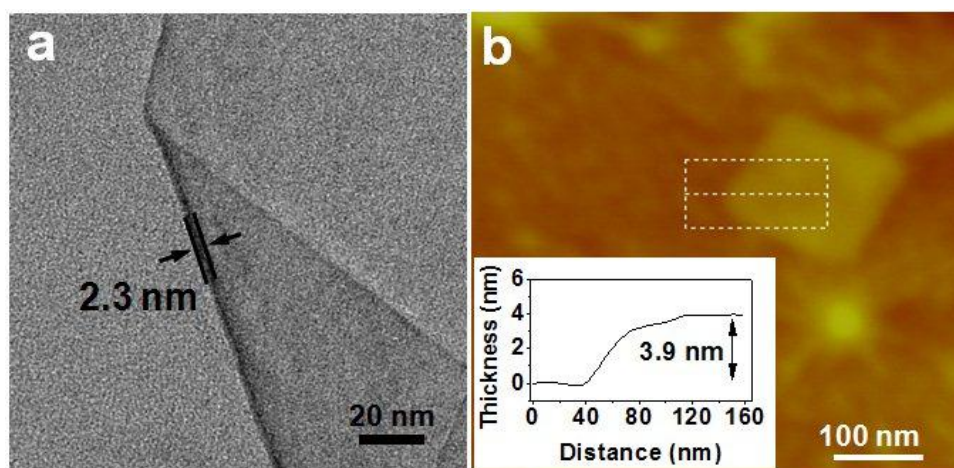


Figure 4-2. (a) TEM image of a folded *hcp* AuSS. (b) AFM image and height profile (inset) of an *hcp* AuSS.

The *hcp* AuSS protected by oleylamine was firstly synthesized according to a recently reported approach with a small change¹⁹. Typically, *hcp* AuSSs were prepared by heating a mixture consisted of oleylamine (150 mM), HAuCl₄ (7.25 mM), hexane, ethanol and GO under 58 °C for 16 h. The edge length and thickness of the as-prepared AuSSs are 100-500 nm and 2.3±0.5 nm, respectively (Figures 4-1 and 4-2). Transmission electron microscope (TEM) study showed that the obtained AuSSs have the *hcp* crystal structure, consistent with the previous report (Figure 4-1)¹⁹. It should be pointed out that although the *fcc* phase is much more stable than *hcp* phase in the bulk Au, the *hcp* AuSSs are very stable in hexane solution for four months under ambient condition, as their low surface energy, because of interaction with the ligand (i.e. oleylamine), dominates in the overall systemic energy¹⁰⁶ and thus helps to stabilize the *hcp* phase.

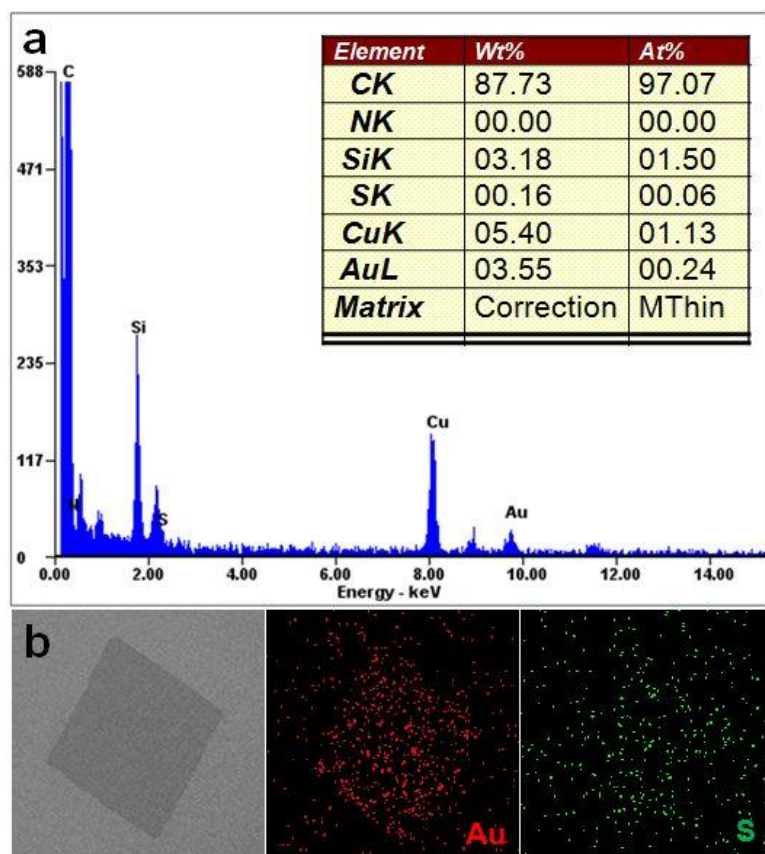


Figure 4-3. (a) EDS investigation of AuSSs deposited on a copper grid after the oleylamine-to-ODT ligand exchange. (b) STEM image and corresponding element mappings of an AuSS after ligand exchange.

The oleylamine originally capped on the *hcp* AuSSs are replaced by octadecanethiol (ODT) molecules when the AuSSs were mixed with the freshly prepared ODT solution, which was then vortexed for 5 min under ambient condition. The energy-dispersive X-ray spectroscopy (EDS) investigation (Figure 4-3) and X-ray photoelectron spectroscopy (XPS) study (Figure 4-4) of the obtained final products after purification revealed that the surface oleylamine molecules was replaced by ODT molecules, which is well consistent with the previous study¹⁰⁷.

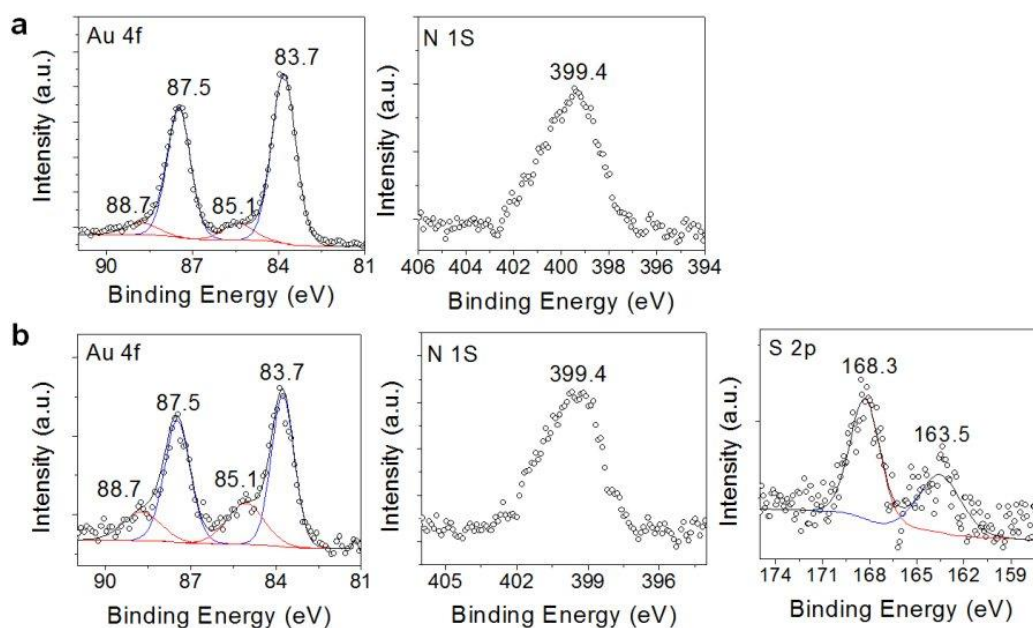


Figure 4-4. XPS spectra of AuSSs on GO sheets (a) before and (b) after ligand exchange from oleylamine to ODT.

The TEM measurement of AuSSs after the oleylamine-to-ODT ligand exchange is demonstrated in Figure 4-5. After the ligand exchange, the square shape of AuSSs is maintained (Figure 4-5a,b). To our surprise, the structure of the obtained AuSSs was totally changed from *hcp* to *fcc* phases after ligand exchange, as confirmed by selected area electron diffraction (SAED) patterns acquired along two different zone axes (Figure 4-5c,d). SAED pattern of a typical AuSS flatly lying on the copper grid showed a $[100]_f$ zone pattern (Figure 4-5c), together with the other two diffraction rings assigned to the $\{100\}$ and $\{110\}$ planes of GO sheets. SAED pattern of the $[310]_f$ zone axis (Figure 4-5d) was also taken by tilting an *fcc* AuSS around $[001]_f$ zone axis for ca. 18.3° , which is well consistent with theoretical angle (i.e. 18.4°) between the $[310]_f$ and $[100]_f$ zone axes, further revealing the *fcc* crystal structure of the as-prepared AuSSs. It is worthy to point out that forbidden $\{011\}_f$ diffraction spots were also observed in SAED patterns of obtained *fcc* AuSSs (Figure 4-5c,d), indicating a likely $c(2 \times 2)$ surface structure of

ODT molecules adsorbed on the surface of $\text{Au}(100)_f$, which matches well with the former study¹⁰⁸.

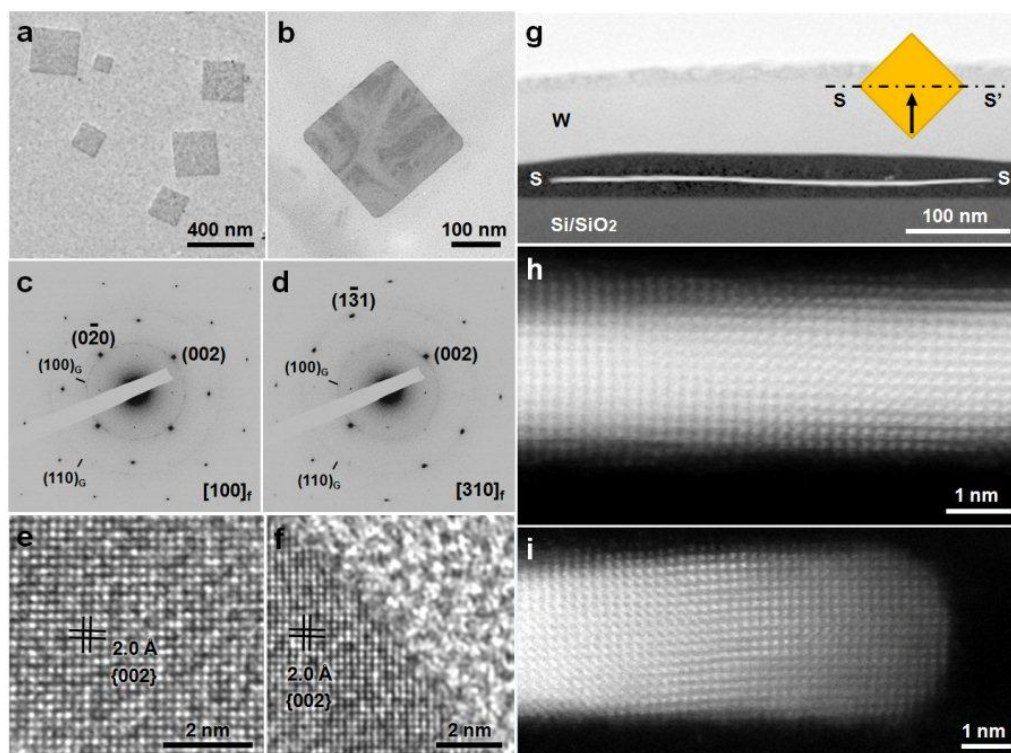


Figure 4-5. (a,b) TEM images of *fcc* AuSSs on GO sheets. (c,d) SAED patterns taken along (c) $[100]_f$ and (d) $[310]_f$ zone axes of an *fcc* AuSS in (b). (e,f) HRTEM images of *fcc* AuSSs. (g) HAADF-STEM image demonstrating cross-section of an *fcc* AuSS. Inset: schematic illustration for the preparation method and view direction of the cross-section sample. (h,i) Aberration-corrected HAADF-STEM images showing the cross-section of the *fcc* AuSS in (g).

HRTEM images of the obtained *fcc* AuSSs (Figure 4-5e,f) demonstrate a square lattice pattern with the inter-plane distance of 2.0 Å, attributed to the $\{002\}_f$ planes. Moreover, high angular annular dark field (HAADF)-scanning TEM (STEM) image of cross section of a typical *fcc* AuSS (Figure 4-5g), which was prepared by the focused ion beam (FIB) along one of the two diagonals, shows a thickness of

about 3.1 ± 0.5 nm (Figure 4-5h,i). It is about 1.7 nm thinner in comparison to the thickness determined by AFM (about 4.8 nm, Figure 4-6), because of ODT molecules adsorbed on the surface. The thickness of resulted *fcc* AuSSs (3.1 ± 0.5 nm) is about 35% larger than that of the original *hcp* AuSSs (2.3 ± 0.5 nm), which is in good agreement with the increased spacing between basal atomic layers, i.e. from the original $d_{(110)h} = 1.5$ Å to final $d_{(200)f} = 2.0$ Å. Aberration-corrected HAADF-STEM images collected in the center (Figure 4-5h) and on the edge (Figure 4-5i) regions of the cross section of atypical *fcc* AuSS demonstrate the $[010]_f$ zone lattice pattern, further proving the complete *hcp*-to-*fcc* phase change of AuSSs.

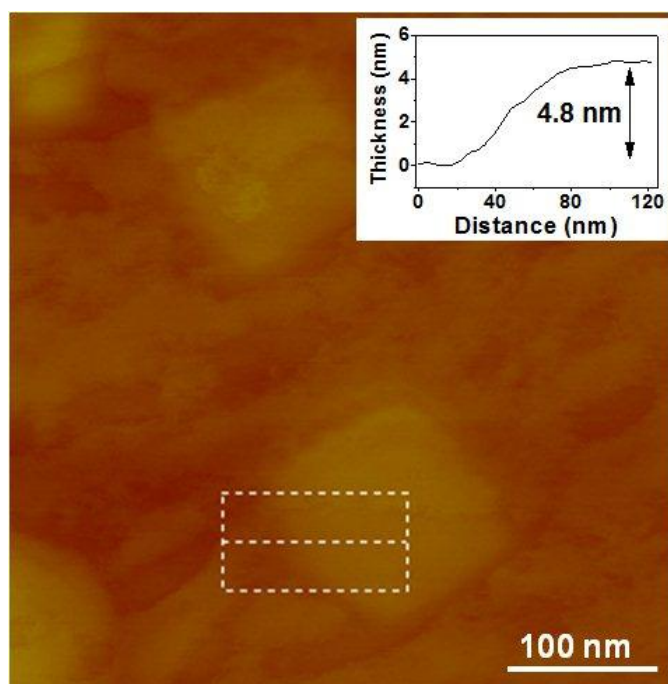


Figure 4-6. AFM image and step investigation of an *fcc* AuSS.

Previously, influences of thiol molecules and the other sulfur-containing chemicals (such as sulfur (S) and H₂S gas) on surface structures of metals and alloys have been investigated^{107,109-111}. It has been suggested that thiols can cause

surface reconstruction of Au films, such as Au(111), because of the spontaneous formation of chemical bond (Au-S)^{107,112-114}. Moreover, the other surface adsorbates (e.g. S) have been revealed to induce surface reconstructions of metal films, especially, benefiting the formation of overlayer with large coordination numbers, e.g. *fcc*(100) surface that has a four-fold hollow site¹¹¹. For instance, S can induce the formation of an overlayer structure of a pseudo Ni{100}_f-c(2×2)S, in which the S atoms take up the rectangular hollow site of the pseudo Ni{100}_f overlayer, on a Ni(111)_f substrate^{110,115}. In addition, H₂S gas can induce the faceting of Pt NPs from initial spherical shape to {100}_f-enclosed nanocubes¹¹⁶. Based on the above discussions, the ligand exchange induced phase change of AuSSs is most probably initiated by a surface reconstruction of (100)_f caused by the adsorbed thiols, followed with a complete phase change over their entire structure.

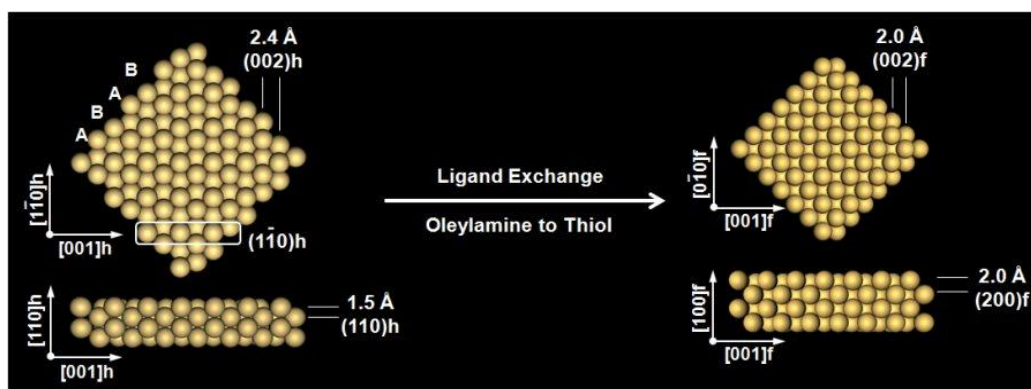


Figure 4-7. Schematic illustration for phase change of *hcp* AuSSs induced by ligand exchange of oleylamine with ODT molecules. Both top and side views are shown.

Figure 4-7 schematically demonstrates the phase change of *hcp* AuSSs induced by the ligand exchange. The oleylamine-to-ODT ligand exchange caused the

transition of the initial $(110)_h$ oriented *hcp* AuSSs to $(100)_f$ oriented *fcc* Au nanosheets. This kind of phase transformation can be obtained through the relative motion of the adjacent $(002)_h$ planes in the opposite directions, together with the concurrent enlargement of inter-plane distance of the $(110)_h$ planes and shrinkage of that of the $(002)_h$ planes, as shown in Figure 4-7¹¹⁷⁻¹¹⁹. Moreover, it can also be regarded as the flattening of the $(1\bar{1}0)_h$ planes, indicated with a rectangle in the left image of Figure 4-7, similar to the phase transformation pathway of wurtzite-to-rock salt found in certain semiconductor nanomaterials, such as GaN and CdSe¹¹⁷⁻¹¹⁹.

4.1.3 Effect of Ligand Concentration

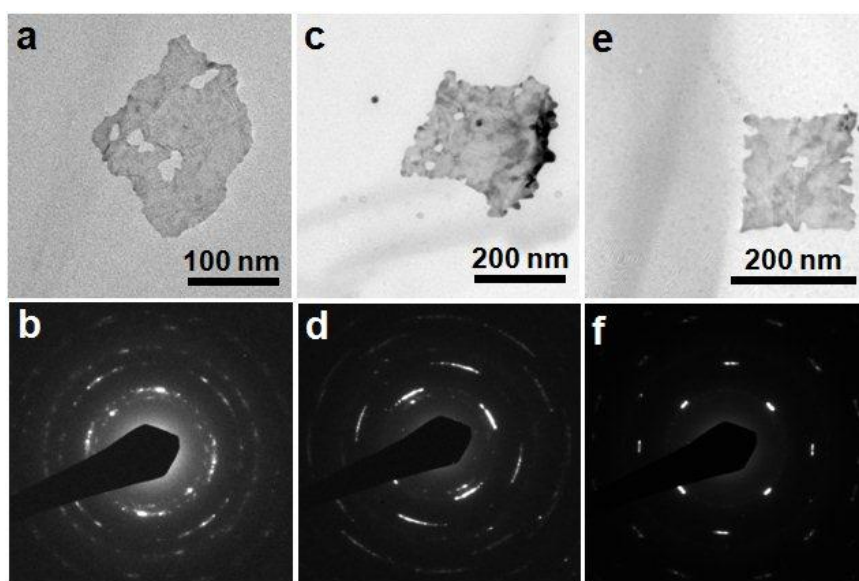


Figure 4-8. TEM images and SAED patterns of Au nanostructures prepared via ligand exchange with ODT at different concentrations for 5 min: (a,b) 2 mM, (c,d) 5 mM, and (e,f) 10 mM.

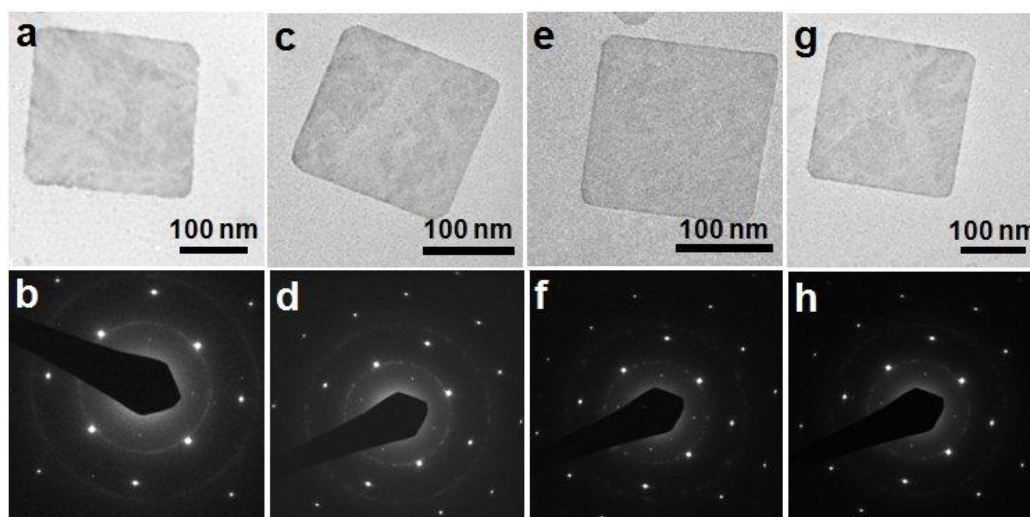


Figure 4-9. TEM images and SAED patterns of Au nanostructures prepared via ligand exchange with ODT at different concentrations for 5 min: (a,b) 20 mM, (c,d) 50 mM, (e,f) 100 mM, and (g,h) 200 mM.

It was observed that the phase change of *hcp* AuSSs can be dramatically affected by the concentration of ODT molecules, as shown in Figures 4-8 and 4-9. At low concentrations of ODT (such as $C_{\text{ODT}} < 20$ mM), the oleylamine-to-ODT ligand exchange resulted in the formation of abnormally shaped Au nanosheets with low crystallinity (Figure 4-8), while under high concentrations of ODT (usually, $C_{\text{ODT}} \geq 20$ mM) Au sheets with well maintained square shape and high crystallinity were synthesized (Figure 4-9). It should be pointed out that in the experiments mentioned above, the concentration of Au atoms was maintained constant (about 2.3 mM). If the Au atom concentration was significantly increased (such as 92 mM), while keeping the concentration of ODT unchanged (e.g. 25 mM), the complete phase change of AuSSs could also be realized, as shown in Figure 4-10. The aforementioned experimental phenomena suggest that sufficiently high concentration of ODT in solution enabled a fast and complete

replacement of oleylamine with ODT molecules, and thus a uniform structure transition over the entire area of *hcp* AuSSs.

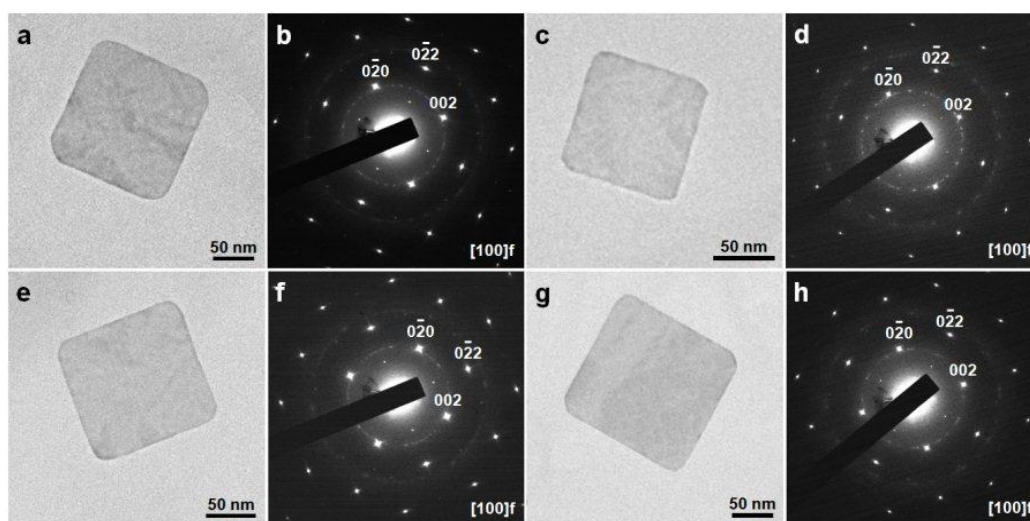


Figure 4-10. (a,c,e,g) TEM images and (b,d,f,h) SAED patterns of AuSSs after the oleylamine-to-ODT ligand exchange at different concentrations of AuSSs: (a,b) 1000 μL AuSS solution (Au atom concentration: 4.6 mM) mixed with 1000 μL ODT solution (50 mM), (c,d) 200 μL AuSS solution (Au atom concentration: 23 mM) mixed with 200 μL ODT solution (50 mM), (e,f) 100 μL AuSS solution (Au atom concentration: 46 mM) mixed with 100 μL ODT solution (50 mM); (g,h) 25 μL AuSS solution (Au atom concentration: 92 mM) mixed with 25 μL ODT solution (50 mM).

4.1.4 Effect of Various Kinds of Thiol Molecules

Besides ODT molecules, other thiol have been applied for ligand exchange of AuSSs, as shown in Figure 4-11. Significantly, the experimental results revealed that the complete phase change of *hcp* AuSSs can be realized by various kinds of thiol molecules, regardless of the length of the *n*-alkane chains ($3 \leq n \leq 18$),

hydrophilicity, the function groups (such as carboxylic acid, benzene or hydroxide), and the number of thiol function groups (such as monothiol or dithiol) (Figure 4-12).

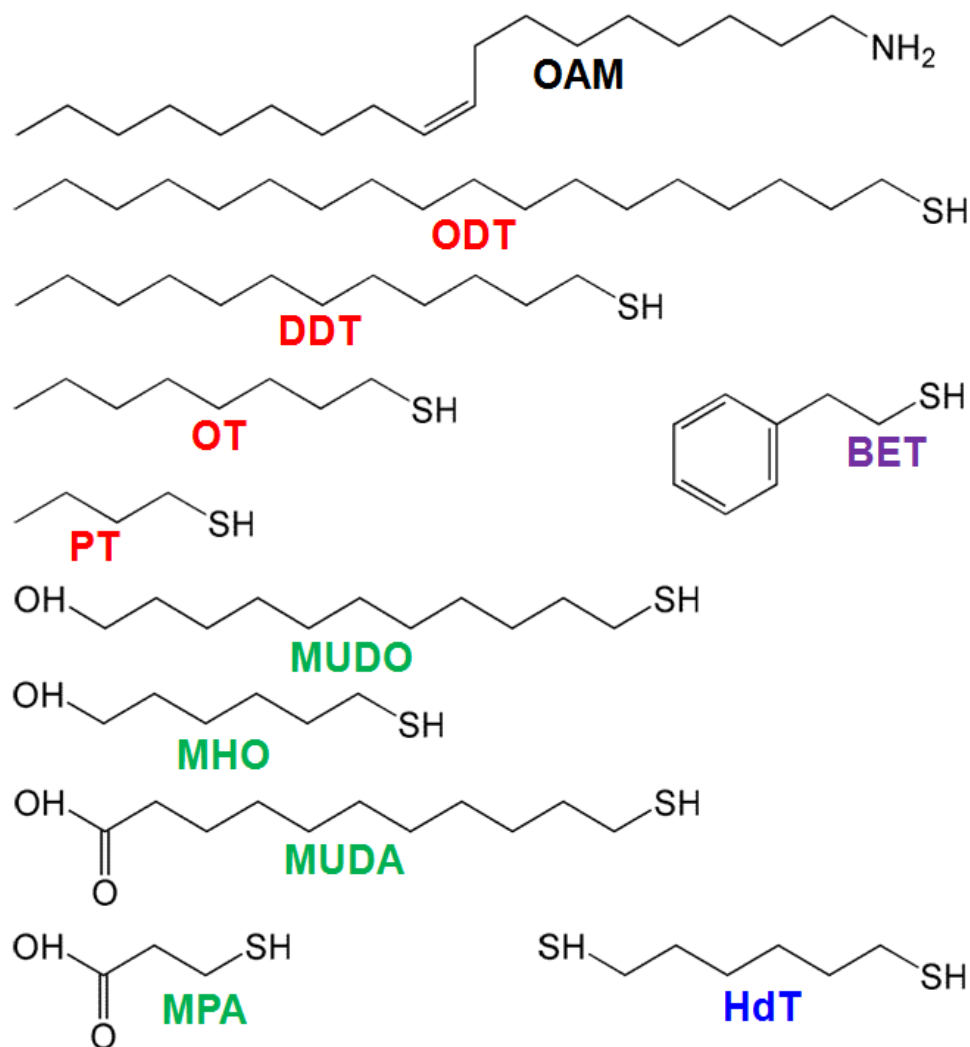


Figure 4-11. Chemical structures of n-alkane thiols (in red color): 1-octadecanethiol (ODT), 1-dodecanethiol (DDT), 1-octanethiol (OT) and 1-propanethiol (PT); hydrophilic thiols (in green color): 11-mercapto-1-undecanol (MUDO), 6-mercapto-1-hexanol (MHO), 11-mercaptoundecanoic acid (MUDA) and 3-mercaptopropionic acid (MPA); aromatic thiol (in purple color): benzeneethanethiol (BET); dithiol (in blue color): 1,6-hexanedithiol (HdT).

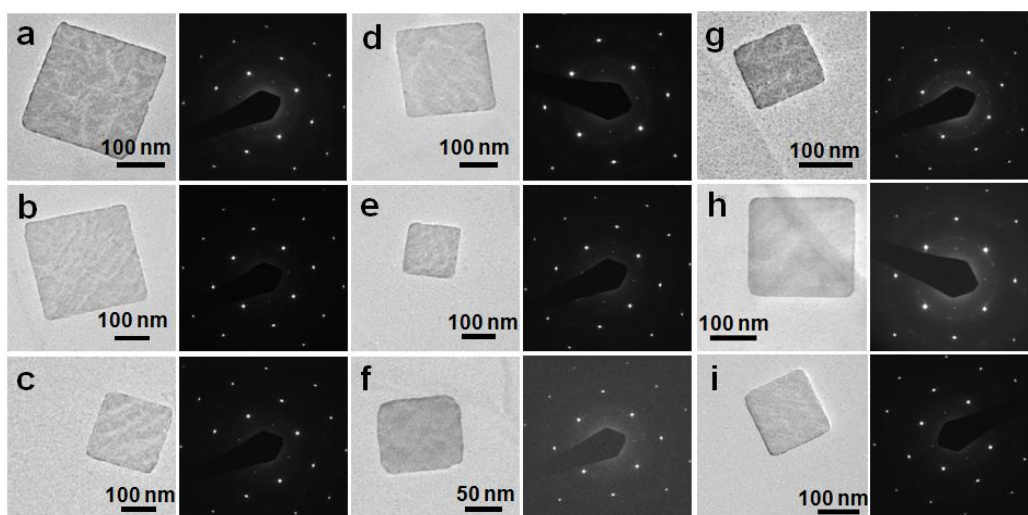


Figure 4-12. TEM images and SAED patterns of *fcc* AuSSs prepared after the oleylamine-to-thiol ligand exchange with different thiol molecules (the concentration of thiols is 50 mM): (a) DDT, (b) OT, (c) PT, (d) MUDO; (e) MHO, (f) MUDA, (g) MPA; (h) BET; (i) HdT.

4.1.5 Monochromated Electron Energy Loss Spectroscopy Measurement of Individual Face-Centered Cubic Au Square Sheets

Localized surface plasmon resonance (LSPR) absorption properties of metal nanostructures, particularly nanosheets and nanoplates, have received widely interests because of their extremely strong LSPR absorption in the visible-infrared (vis-IR) region, which can effectively benefit their various potential applications (such as IR photothermal therapy)^{2,6,120,121}. Normally, the LSPR properties of metal nanostructures are studied by common optical spectrophotometer. But the spatial resolution of common optical spectrophotometer is relatively low, and hence not applicable for the nanometer scale plasmon measurement of an individual metal nanostructure. Importantly, with the rapid development of monochromated EELS

technique^{22,122}, which integrates high spectral and spatial resolution, the LSPR properties of individual metal nanostructures can be characterized.

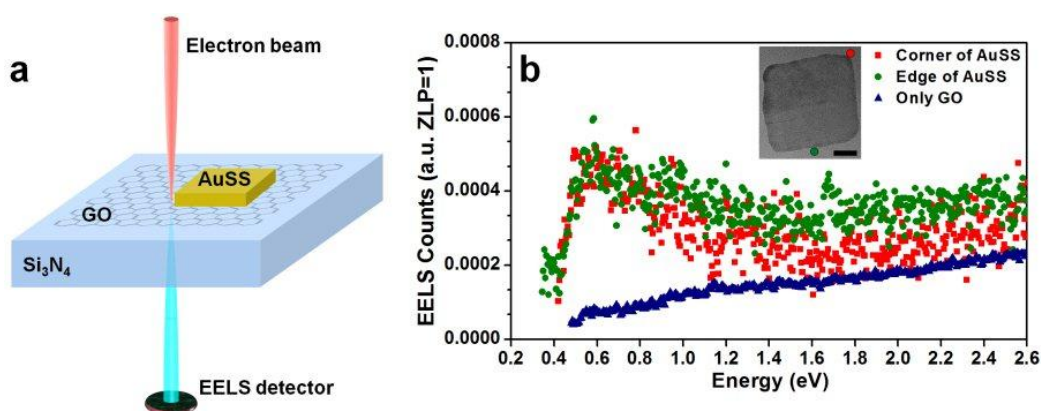


Figure 4-13. (a) Schematic illustration for monochromated EELS characterization of a single *fcc* AuSS on GO sheet. (b) EELS spectra collected from an individual AuSS on GO sheet (excited next to edge and corner of an *fcc* AuSS and GO sheet. Inset: STEM image of the selected AuSS on GO sheet (scale bar, 20 nm), in which positions of the focused electron beam are indicated.

The LSPR properties of an individual *fcc* AuSS on GO sheet were studied by monochromated EELS in STEM. In a typical experiment, the EELS characterization of individual *fcc* AuSSs was executed by positioning the focused electron beam next to (2–3 nm) the edge or corner regions of the *fcc* AuSS on GO sheet to excite its LSPR (Figure 4-13a). A control EELS spectrum of GO sheet was also acquired at about 500 nm away from the *fcc* AuSS, where merely GO presents (Figure 4-13b, the blue curve). Remarkably, the EELS spectrum of the corner region of *fcc* AuSS on GO sheet demonstrates a strong LSPR absorption peak at 0.59 eV (or 2102 nm) (Figure 4-13b, the red curve). The EELS spectrum of the edge region of the *fcc* AuSS on GO sheet demonstrates a similar LSPR absorption feature, which further proves its LSPR absorption in the IR region

(Figure 4-13b, the green curve). Such a strong IR absorption is derived from the in-plane surface plasmon resonance of two-dimensional *fcc* AuSS with relatively large edge length-to-thickness aspect ratio^{6,120,121,123,124}.

4.1.6 Short Summary

In this section, the *fcc* AuSSs, with a thickness of about 3.1 ± 0.5 nm, have been successfully synthesized from *hcp* AuSSs via the oleylamine-to-ODT ligand exchange under ambient conditions. Note that noble metal nanoplates/nanosheets usually shows the common shapes of triangle or hexagon, which are enclosed low energy basal planes of $\{111\}_f$ ². The first observation of *fcc* Au nanosheets/nanoplates with the orientation of $(111)_f$ dates back to the 1950s¹²⁵. But free-standing noble metal nanosheets/nanoplates with the other orientations have not been synthesized by wet-chemical solution method during the following six decades. In this work, $(100)_f$ -oriented AuSSs have been prepared. Importantly, the crystallinity of *fcc* AuSSs can be finely tuned by adjusting the concentration of ligand. Significantly, besides ODT, various kinds of thiol molecules can be used to synthesize *fcc* AuSSs from *hcp* AuSSs. In addition, monochromated EELS revealed strong LSPR absorption of the *fcc* AuSS in IR range. It is believed that the ligand exchange mediated synthetic approach developed in the present work will provide new opportunities for the controlled synthesis of new noble metal nanomaterials, which have promising applications in plasmonics and catalysis^{2,6}.

4.2 Metal Coating Assisted Synthesis of Novel Bimetallic Nanosheets

4.2.1 Introduction

Noble metal nanocrystal (NC) has received extensive interest because it shows fascinating catalytic and optical properties and exhibited promising applications in plasmonics¹²⁶, surface-enhanced Raman spectroscopy (SERS)^{2,126,127}, catalysis^{6,53}, and photo-thermal therapy⁶. As widely known, the physical and chemical properties of noble metal NCs can be adjusted with their shape and size^{2,6,53}. Moreover, their functional properties are also largely influenced by their crystal phases^{18,72}. For instance, hexagonal close-packed (*hcp*) Ag nanowires demonstrated low-frequency electrical noise of two to six orders of magnitude lower in comparison with that of common face-centered cubic (*fcc*) Ag nanowires⁷². Thus the control over the crystal phase is of paramount importance in the preparation of noble metal NCs. Former investigations on the structure modulation of noble metal NCs mostly relied on the harsh experiment conditions, e.g. high pressure⁶⁵, high temperature¹⁶, or electron beam illumination at ultra-high vacuum conditions¹⁹. But it still remains a big challenge to realize the structure adjustment of noble metal NCs at ambient condition.

Very recently, wide attention has been drawn to the preparation of noble bimetallic NCs because they exhibit better functional properties^{46,47,128-130} and demonstrate much higher stability^{47,131} in comparison with the monometallic counterparts. As widely known, epitaxial seeded growth has been widely found in solution phase preparation of noble bimetallic NCs at ambient condition due to the relatively small crystal lattice mismatch between two noble metals (normally <

5%)¹³². Typically, the synthetic procedure starts with noble metal NC as the “seed”, followed by the consecutive epitaxial growth^{12,56,133}, or Galvanic replacement reaction¹³⁴ with another noble metal. So far, noble metal NCs with a shape of nanosphere^{135,136}, nanorod¹³⁴, triangular and hexagonal nanoplate^{131,137}, or nanopolyhedron^{12,56,57,132,133,138} have been applied as the seeds for the synthesis of noble bimetallic nanostructures with well controlled shape, size, atomic distribution (such as core-shell, alloy and heterostructure) and composition. But all of the noble metal seeds used in the aforementioned studies are *fcc* NCs. To date, the solution epitaxial seeded growth of noble bimetallic NC via using the non-*fcc* nanocrystal as the seed has scarcely been explored¹³⁹, particularly, for Pt, Pd, Au, and Ag.

In 2011, Huang *et al.* reported the successful preparation of ultrathin *hcp* Au square sheet (AuSS) on graphene oxide (GO) sheets¹⁹. In this section, a facile strategy has been established to synthesize a series of ultrathin noble bimetallic nanosheets via metal coating on *hcp* AuSSs under ambient conditions. The (100)_f-oriented *fcc* Au@Ag square sheets have been prepared via the epitaxial growth of Ag on the *hcp* AuSSs in the absence of oleylamine. Interestingly, polytypic *hcp/fcc* Au@Ag square sheets with an orientation of (110)_h/(101)_f are obtained through the epitaxial seeded growth of Ag on *hcp* AuSSs in the presence of oleylamine. Remarkably, (101)_f oriented *fcc* Au@Pt and Au@Pd rhombic sheets, coexisting with tiny amount of (100)_f oriented *fcc* Au@Pt and Au@Pd square sheets, are obtained from *hcp* AuSSs by changing the coating metal from Ag to Pt and Pd, respectively. In addition, monochromated electron energy loss spectroscopy (EELS) study on the localized surface plasmon resonance (LSPR) absorption property of individual *fcc* Au@Ag square sheets has been conducted.

4.2.2 Synthesis and Characterization of Face-Centered Cubic Au@Ag Square Sheets

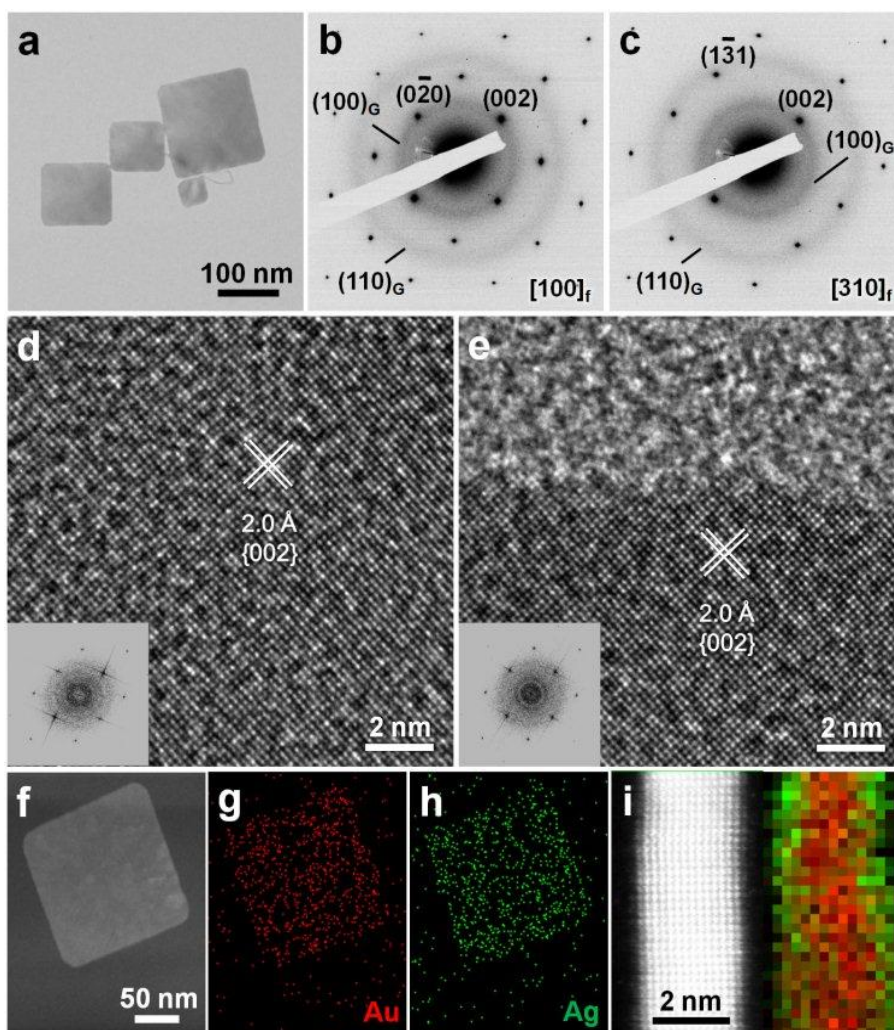


Figure 4-14. (a) TEM image of *fcc* Au@Ag square sheets on GO sheets by using ascorbic acid as reductant. (b,c) SAED patterns taken along (b) $[100]_f$ and (c) $[310]_f$ zone axes of an *fcc* Au@Ag square sheet. (d,e) HRTEM images of an *fcc* Au@Ag square sheet. Insets in (d,e): fast Fourier transform (FFT) patterns of the HRTEM images in (d) and (e). (f) HAADF-STEM image and (g,h) STEM-EDS element mappings of an *fcc* Au@Ag square sheet. (i) Aberration-corrected HAADF-STEM image and STEM-EDS element mapping showing the cross section of an *fcc* Au@Ag square sheet.

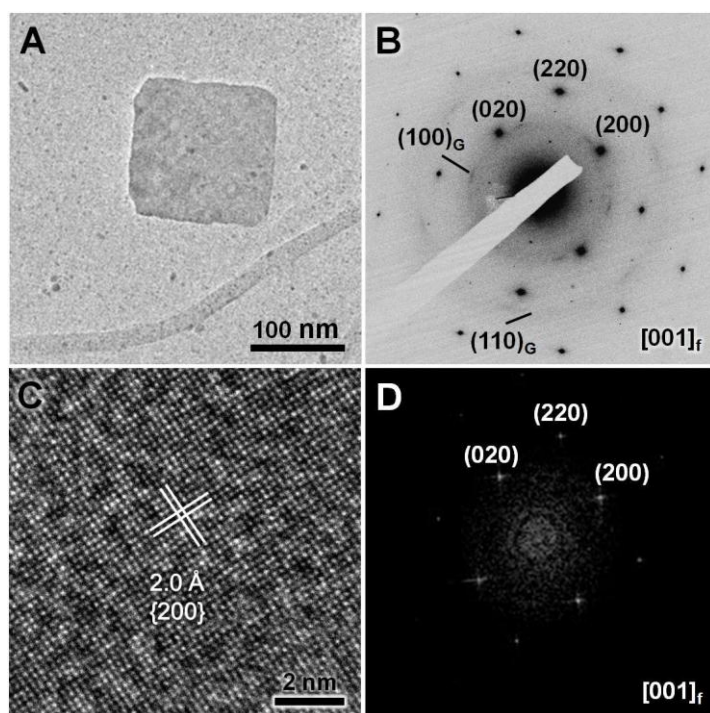


Figure 4-15. (a) TEM image and (b) SAED pattern of an *fcc* Au@Ag square sheet on GO by using NaBH₄ as reductant. (c) HRTEM image and (d) FFT pattern of obtained *fcc* Au@Ag square sheets.

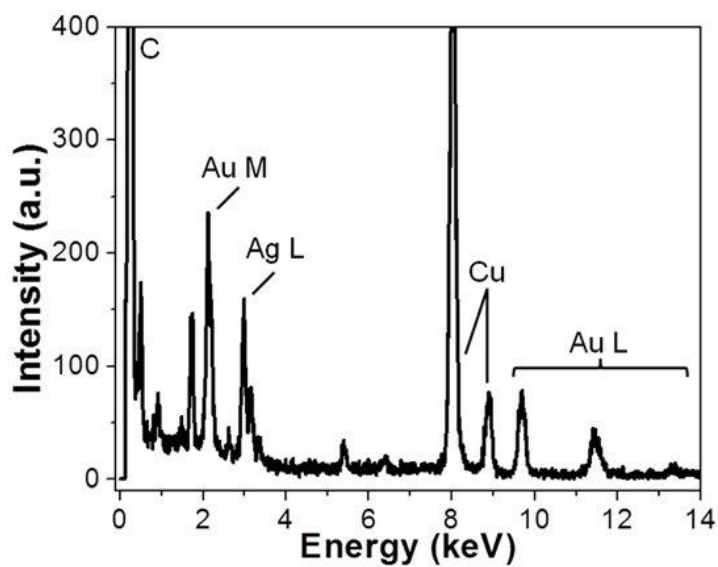


Figure 4-16. STEM-EDS spectrum of *fcc* Au@Ag square sheets. The average atomic ratio between Au and Ag is estimated to be 1: 1.4.

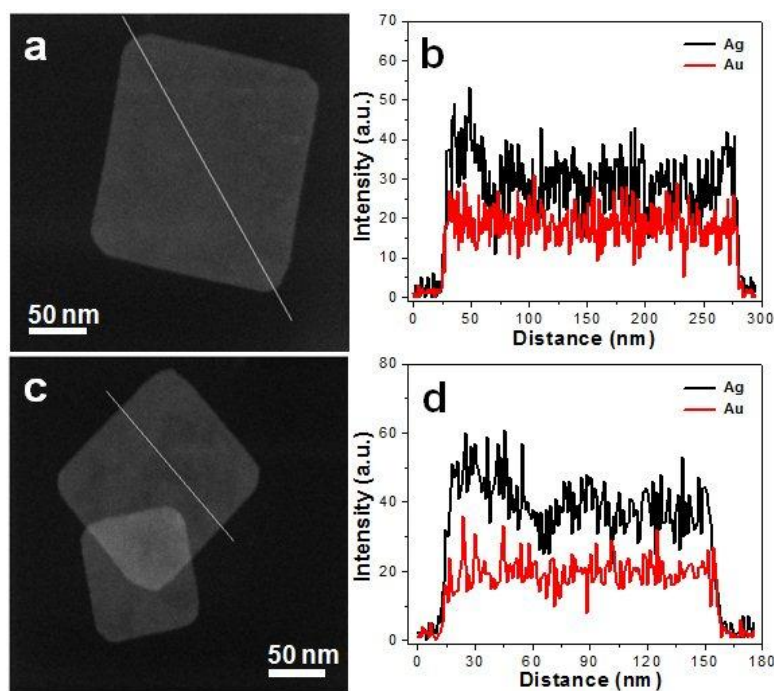


Figure 4-17. (a,c) HAADF-STEM images and (b,d) STEM-EDS line scanning analyses of obtained *fcc* Au@Ag square sheets.

Similar to the ligand exchange mediated synthesis of *fcc* AuSSs from *hcp* AuSSs (Figures 4-1 and 4-5), it was observed that coating of a thin layer of Ag onto *hcp* AuSSs can induce a phase change from *hcp* to *fcc* structures in the absence of oleylamine. In a typical experiment, the epitaxial growth of Ag on the *hcp* AuSSs was realized by reducing AgNO_3 with ascorbic acid or NaBH_4 (Figures 4-14 and 4-15). It shows that after the deposition of Ag, square shape of nanostructures is maintained (Figure 4-14a). The chemical composition of as-prepared Au-Ag square sheets is studied by the energy dispersive X-ray spectroscopy (EDS) (Figure 4-14f-h and Figures 4-16 and 4-17), which indicates the uniform distribution of Ag and Au in the obtained bimetallic nanostructure. Besides, X-ray photoelectron spectroscopy (XPS) data suggests the surface of as-prepared Au-Ag nanostructures are bound by oleylamine molecules (Figure 4-18).

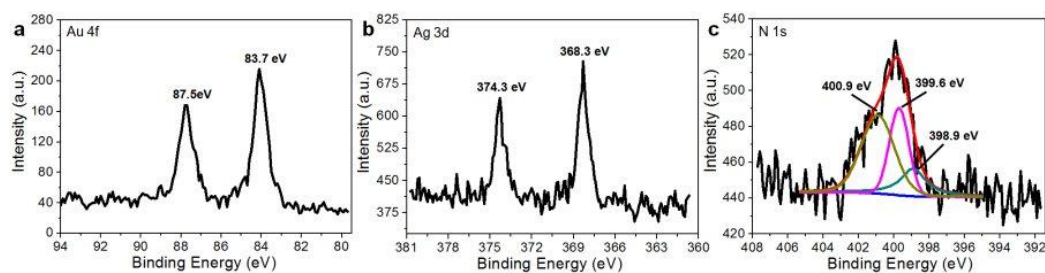


Figure 4-18. High-resolution XPS spectra of (a) Au 4f, (b) Ag 3d, and (c) N 1s in obtained *fcc* Au@Ag square sheets.

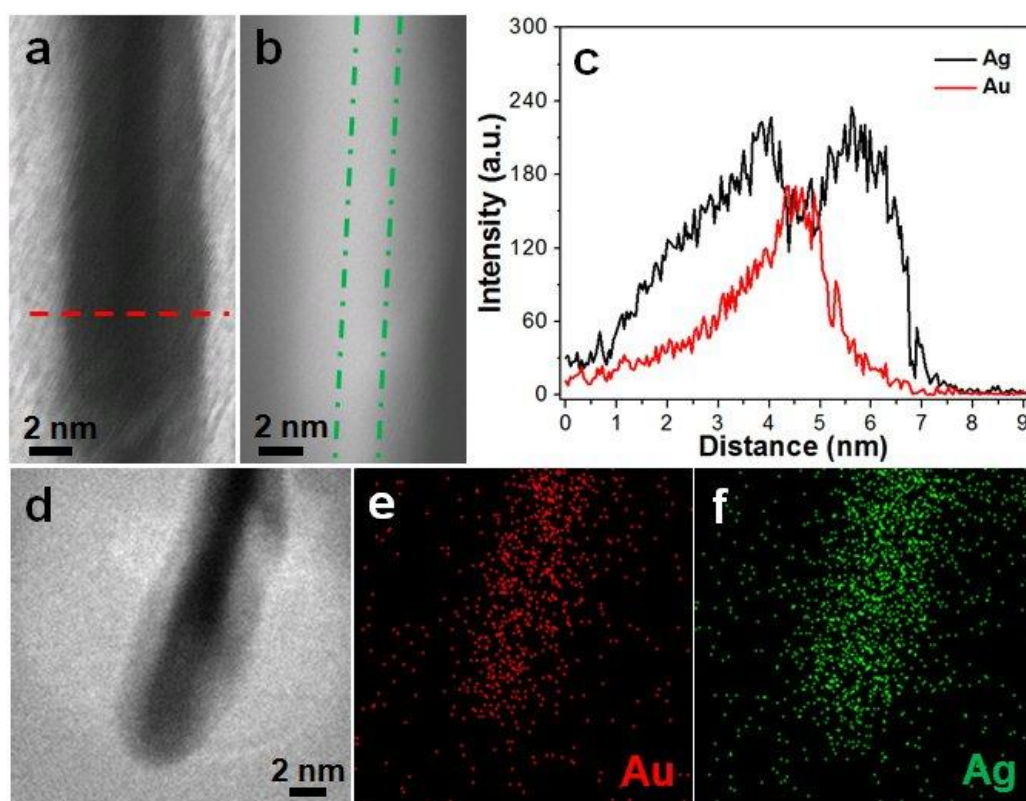


Figure 4-19. (a) Bright-field and (b) dark-field STEM images of the cross section of an *fcc* Au@Ag square sheet. (c) STEM-EDS line scanning profile of the cross section shown in (a). (d) STEM image and (e,f) STEM-EDS element mappings of the cross-section sample of an *fcc* Au@Ag square sheet.

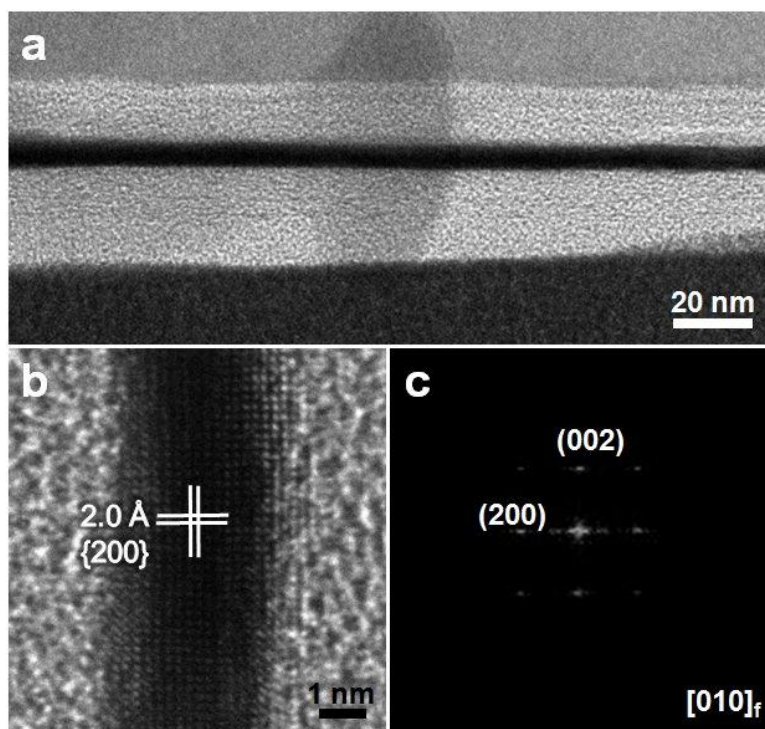


Figure 4-20. (a) TEM image, (b) HRTEM image and (c) FFT pattern of a cross-section sample of an *fcc* Au@Ag square sheet.

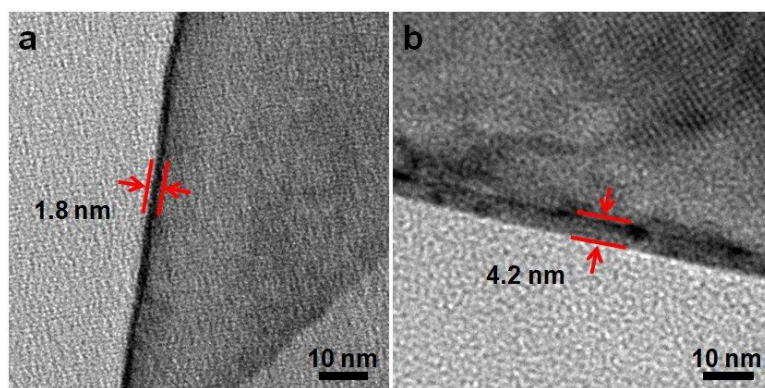


Figure 4-21. TEM images of a folded (a) *hcp* AuSS and (b) *fcc* Au@Ag square sheet. The Moiré pattern observed in (b) are induced by the folding of *fcc* Au@Ag square sheet.

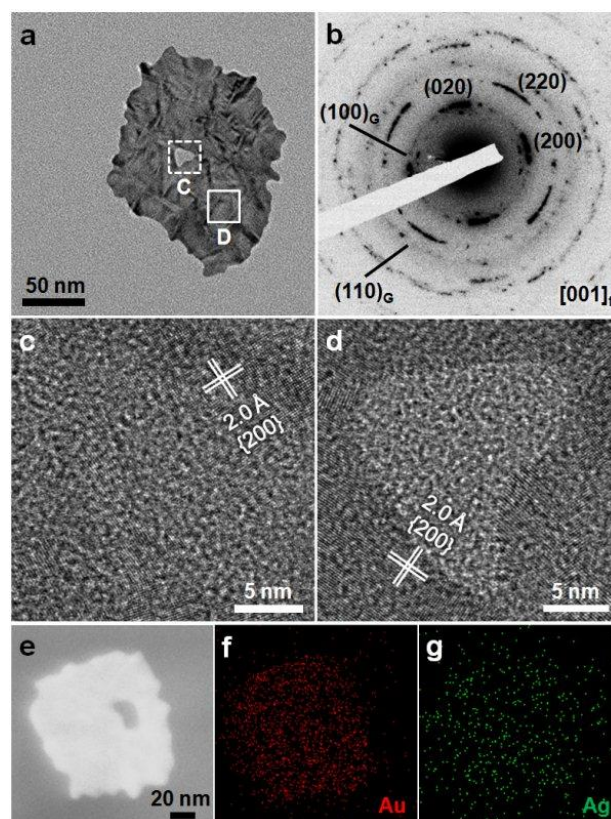


Figure 4-22. (a) TEM image and (b) SAED pattern of an irregular-shaped *fcc* Au@Ag sheet. (c,d) HRTEM images of the marked regions in (a). (e) HAADF-STEM image and (f,g) STEM-EDS element mapping of an irregular-shaped *fcc* Au@Ag sheet.

The cross section of the obtained Au-Ag nanosheets was fabricated with focused ion beam (FIB), and studied under the transmission electron microscopy (TEM). The EDS mappings (Figure 4-14i) and line scannings (Figure 4-14) of the as-prepared cross sections of Au-Ag nanosheets indicated that the resulted final product is Au@Ag core-shell nanostructures. Depending on the amount of Ag grown on the initial *hcp* AuSS, the thickness of obtained Au@Ag bimetallic nanosheets changed in range of 3.0 to 4.6 nm (Figure 4-14i, Figures 4-19 to 4-21). Surprisingly, the selected area electron diffraction (SAED) patterns (Figure 4-14b,c) and high-resolution TEM (HRTEM) images (Figure 4-14d,e) of a typical

Au@Ag bimetallic nanosheet lying on the copper grid, and high angle annular dark field-scanning TEM (HAADF-STEM) image of a cross section of the Au@Ag nanosheet (Figure 4-14i) suggest that crystal phase of obtained Au@Ag square sheets is pure of *fcc* structure with a unique orientation of (100)_f, which is similar to the crystal structure of *fcc* AuSSs synthesized from *hcp* AuSSs by ligand exchange (Figure 4-5).

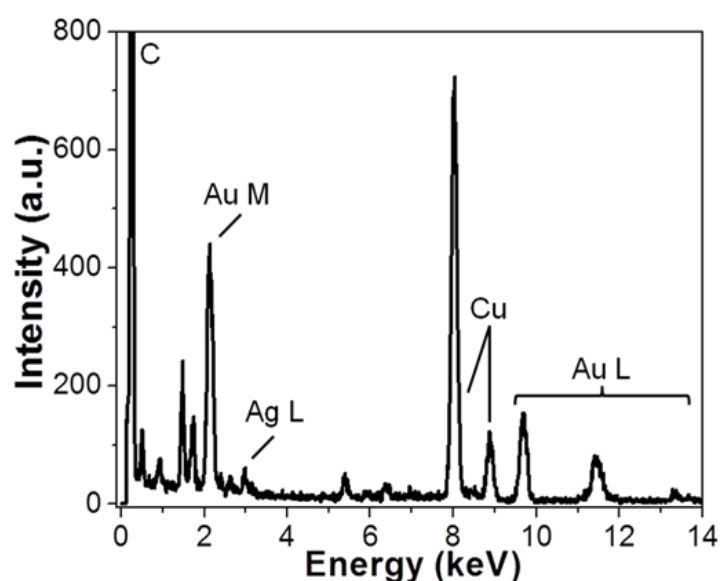


Figure 4-23. STEM-EDS spectrum of irregular-shaped *fcc* Au@Ag sheets. The average atomic ratio between Au and Ag is estimated to be 1: 0.3.

It should be pointed out that the crystal lattice parameters of *fcc* Ag ($a = 4.086 \text{ \AA}$, ICSD no. 604630) and Au ($a = 4.078 \text{ \AA}$, ICSD no. 52249) are close to each other (about 0.2% lattice mismatch), which favors for the epitaxial growth between Au and Ag. Indeed, the continuous lattice fringe from the inside Au core to outside Ag shell was found, suggesting epitaxial relationship between the Au core and the Ag shell (Figure 4-14i and Figure 4-20). Furthermore, it was found that insufficient coating of Ag on *hcp* AuSSs can cause the formation of abnormally shaped and lowly crystallized Au@Ag nanostructure (Figures 4-22 and 4-23), which is in

good agreement with that of the ligand exchange mediated synthesis of *fcc* AuSSs under low concentrations of thiol molecules (Figure 4-8).

4.2.3 Synthesis and Characterization of Polytypic Hexagonal Close-Packed/Face-Centered Cubic Au@Ag Square Sheets

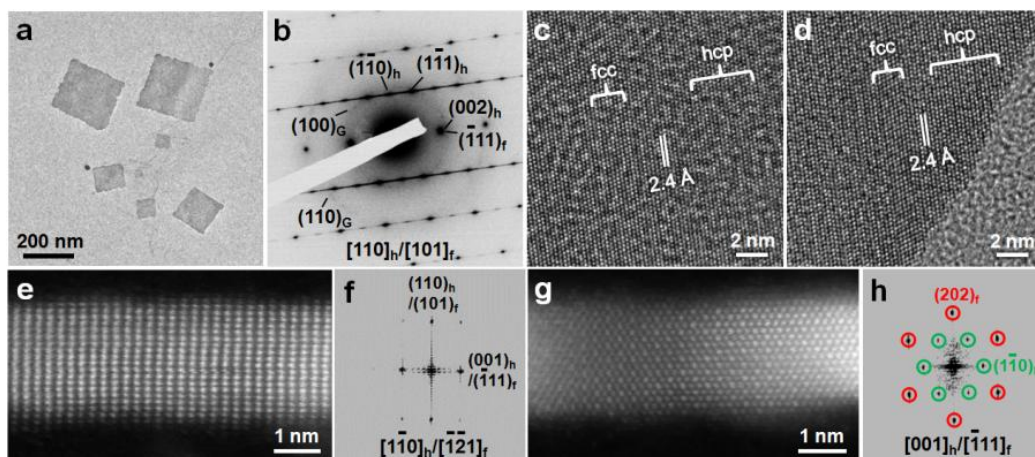


Figure 4-24. (a) TEM image of *hcp/fcc* Au@Ag square sheets on GO sheet. (b) SAED pattern and (c,d) HRTEM images of an *hcp/fcc* Au@Ag square sheet. (e,g) Aberration-corrected HAADF-STEM images and (f,h) FFT patterns of the cross sections of the *hcp/fcc* Au@Ag square sheets collected along $[1\bar{1}0]_h/[\bar{1}\bar{2}1]_f$ and $[001]_h/[\bar{1}\bar{1}1]_f$ zone axes, respectively.

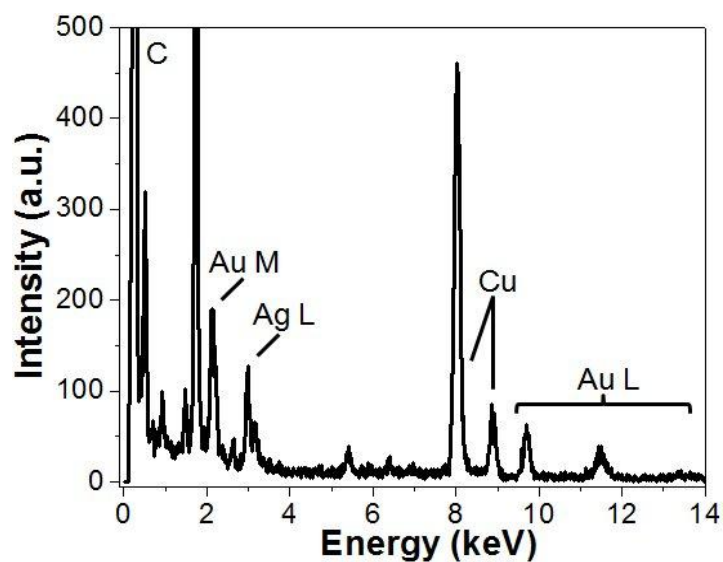


Figure 4-25. STEM-EDS spectrum of *hcp/fcc* Au@Ag square sheets. The average atomic ratio between Au and Ag is estimated to be 1: 1.5.

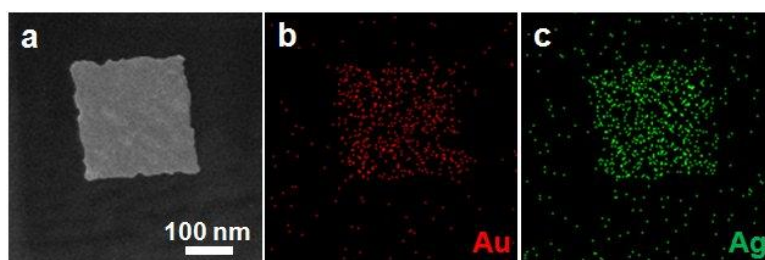


Figure 4-26. (a) HAADF-STEM image and (b,c) STEM-EDS element mapping of an *hcp/fcc* Au@Ag square sheet.

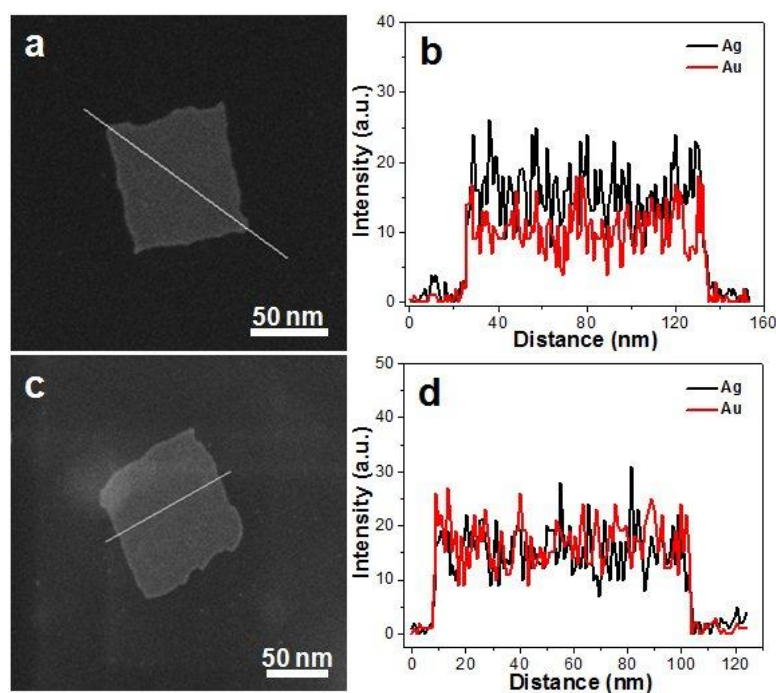


Figure 4-27. (a,c) HAADF-STEM images and (b,d) STEM-EDS line scanning analyses of *hcp/fcc* Au@Ag square sheets.

Surprisingly, polytypic *hcp/fcc* Au@Ag square sheet was achieved when the reductant used for epitaxial seeded growth of Ag on the *hcp* AuSS was changed from NaBH_4 or ascorbic acid to oleylamine (Figure 4-24). The EDS analysis on plan-view and cross-section samples reveals the homogeneous growth of Ag shell on the Au core (Figures 4-25 to 4-28). The XPS study shows that the obtained Au@Ag square sheets are capped with oleylamine molecules (Figure 4-29). The thickness of the as-prepared *hcp/fcc* Au@Ag square sheets was measured to be about 2.8 ± 0.5 nm with the TEM images of the cross-section samples (Figure 4-24e,g; Figures 4-28 and 4-30).

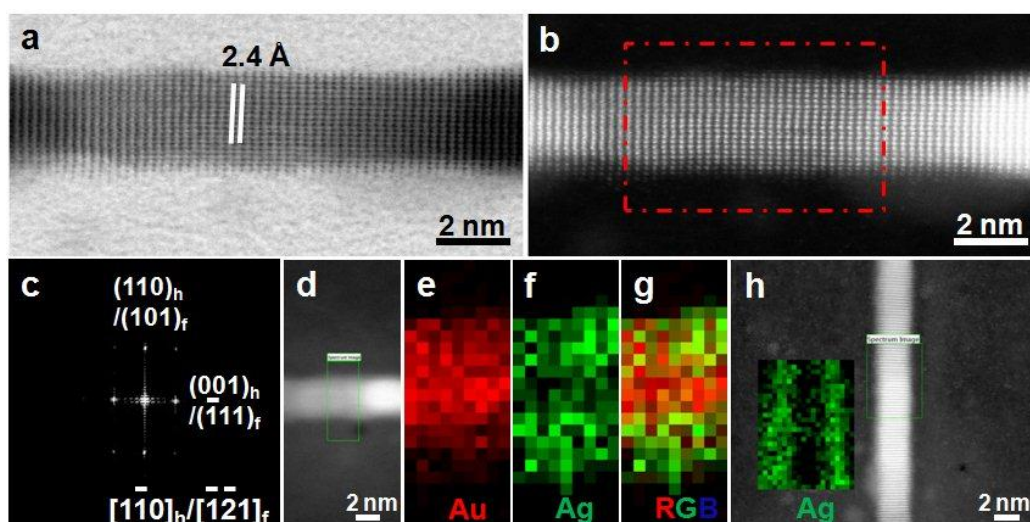


Figure 4-28. Aberration-corrected (a) bright-field and (b) dark-field STEM images of a cross section of *hcp/fcc* Au@Ag square sheets cut along $[001]_h/[111]_f$ directions. (c) FFT pattern of the region marked in (b). (d) HAADF-STEM image and (e-g) STEM-EDS element mappings of a cross section of *hcp/fcc* Au@Ag square sheets. (h) HAADF-STEM image of the cross section of an *hcp/fcc* Au@Ag square sheet (Inset: EELS mapping of Ag).

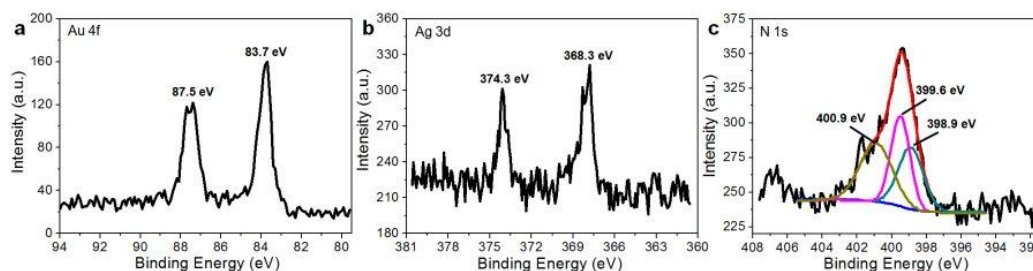


Figure 4-29. High-resolution XPS spectra of (a) Au 4f, (b) Ag 3d, and (c) N 1s in obtained *hcp/fcc* Au@Ag square sheets.

A TEM image of as-prepared Au@Ag square sheets is demonstrated in Figure 4-24a, which shows that the edge of nanosheets was slightly etched in the process of Ag coating. SAED pattern of a typical Au@Ag square sheet (Figure 4-24b) can be assigned to the *hcp*- $[110]_h$ zone pattern along with the other diffuse diffraction

spot streaking along the $[001]_h$ direction, indicating the coexisting of alternative *hcp* and *fcc* phases along with lots of twins and stacking faults along the $[001]_h/[111]_f$ directions. The center (Figure 4-24c) and edge (Figure 4-24d) areas (the *hcp* and *fcc* domains are marked) of Au@Ag square sheets were further studied with the plan-view HRTEM images, and the dark-field TEM image acquired with the $[1\bar{1}0]_h$ diffraction spot (Figure 4-31).

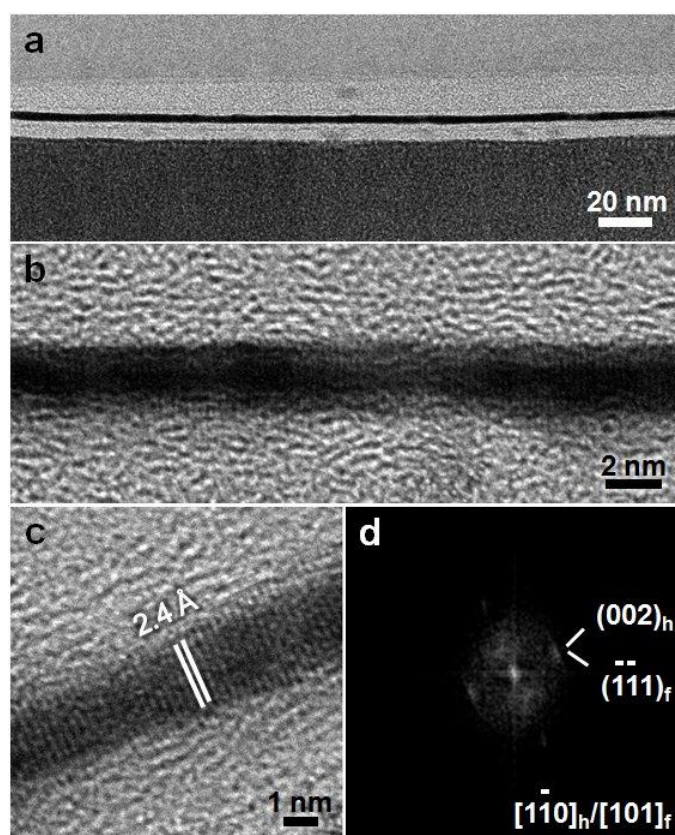


Figure 4-30. (a) Low-magnification and (b-c) high-resolution TEM images of a cross-section of obtained *hcp/fcc* Au@Ag square sheets cut along $[001]_h/[111]_f$ directions. (d) FFT pattern of HRTEM image shown in (c).

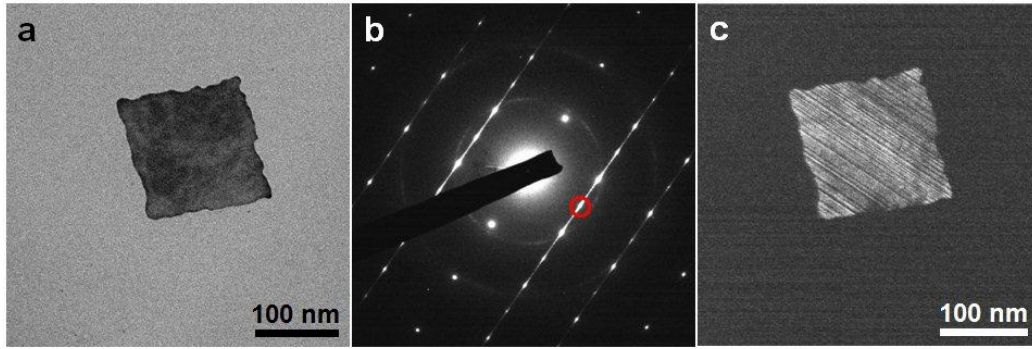


Figure 4-31. (a) TEM image and (b) SAED pattern of an *hcp/fcc* Au@Ag square sheet. (c) The dark-field TEM image acquired with $(1\ \bar{1}\ 0)_h$ diffraction spot indicated in (b).

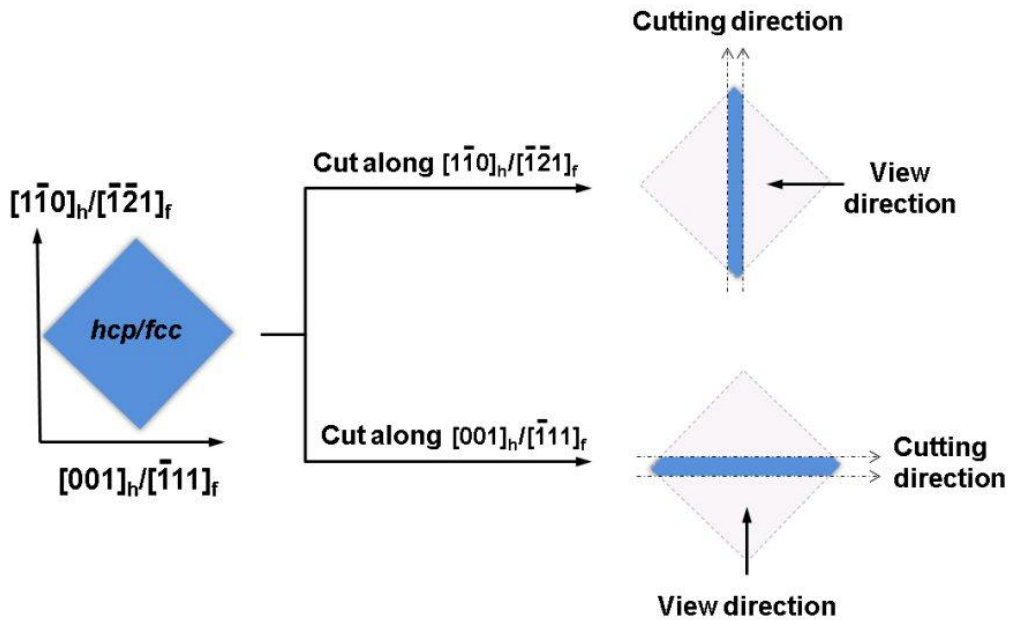


Figure 4-32. Schematic illustration on the preparation of cross sections of *hcp/fcc* Au@Ag square sheets.

To further identify the crystal lattice correlation between the outside Ag shell and inside Au core, the *hcp/fcc* Au@Ag square sheets were cut along the $[001]_h/[\bar{1}\ \bar{1}\ 1]_f$ and $[1\ \bar{1}\ 0]_h/[\bar{1}\ \bar{2}\ 1]_f$ directions (Figure 4-32) to show the crystal lattice patterns of the $[1\ \bar{1}\ 0]_h/[\bar{1}\ \bar{2}\ 1]_f$ (Figure 4-24e) and $[001]_h/[\bar{1}\ \bar{1}\ 1]_f$ zone axes (Figure 4-24g),

respectively. The cross-section HAADF-STEM images and the FFT patterns (Figure 4-24e-h) clearly reveal the coherent atomic arrangement from the inside Au core to outside Ag shell, indicating the epitaxial relationship between Au and Ag. It should be pointed out that from the view direction in Figure 4-24g, *hcp* (002) planes are overlapped with the *fcc* ($\bar{1}11$) planes, and thus the corresponding FFT pattern in Figure 4-24h demonstrates two sets of diffraction patterns, i.e. $[001]_h$ (marked in green) and $[\bar{1}11]_f$ (marked in red) zone patterns, respectively.

4.2.4 Role of Surfactant in the Synthesis of Au@Ag Square Sheets

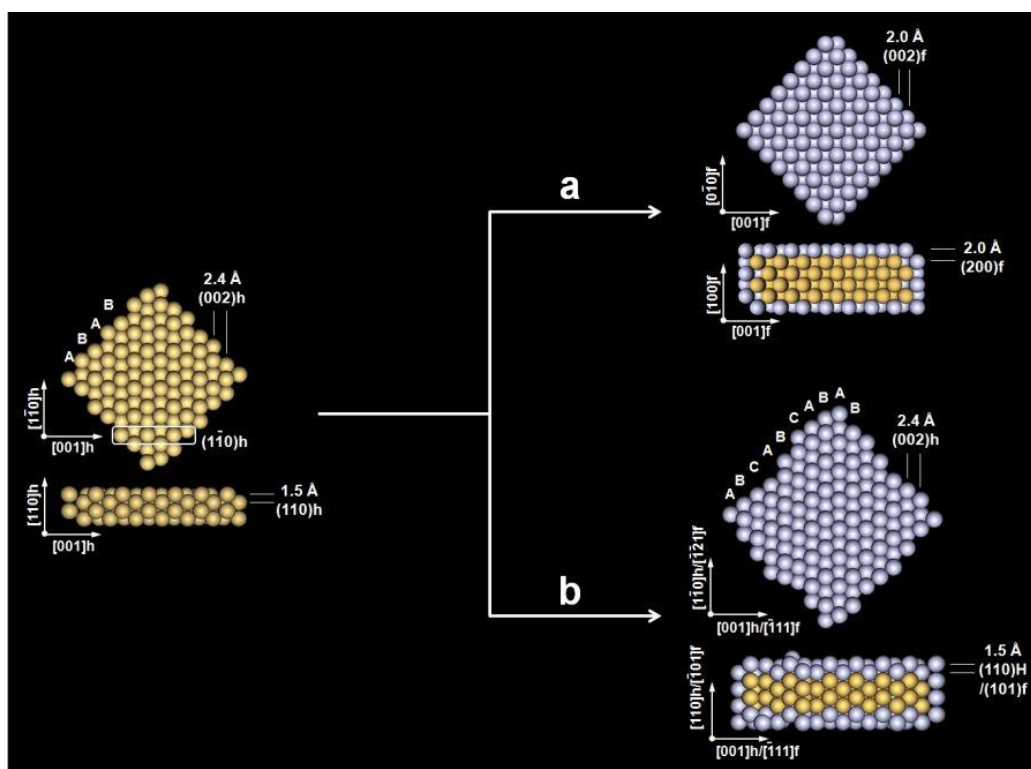


Figure 4-33. Schematic illustration for the Ag coating on *hcp* AuSSs (a) with ascorbic acid as reductant in the absence of oleylamine, and (b) with oleylamine as reductant and capping agent.

As for the Ag coating on *hcp* AuSSs, when NaBH_4 or ascorbic acid was applied as the reductant, *fcc* Au@Ag square sheet with the orientation of $(100)_f$ was achieved (Figure 4-33a). It should be pointed out that *hcp* AuSSs initially protected with oleylamine molecules were cleaned four times before the epitaxial growth of Ag. Therefore, only a tiny amount of oleylamine molecules remained on the surface of *hcp* AuSSs. When oleylamine was applied as the reductant and capping agent, polytypic *hcp/fcc* Au@Ag square sheets with the $(110)_h/(101)_f$ orientations was realized (Figure 4-33b). This kind of phase change belongs to commonly observed Martensitic transition (Figure 4-33b), which usually proceeds by the change of stacking sequence of the closed-packed planes, leads to formation of twins/stacking faults, or the coexisting of alternative *hcp* and *fcc* phases¹⁰³. Furthermore, the nanostructure's orientation regarding to its close-packed directions (i.e. $[111]_f$ and $[001]_h$ directions) is maintained in the process of structure evolution.

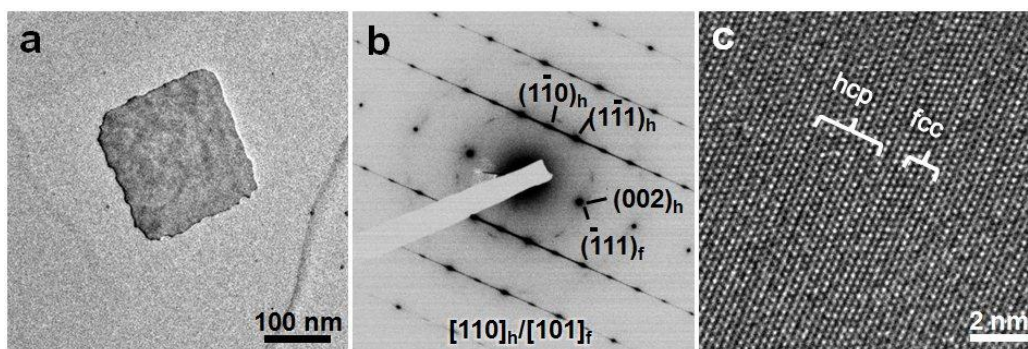


Figure 4-34. (a) TEM image and (b) SAED pattern along $[110]_h/[101]_f$ zone axes of an *hcp/fcc* Au@Ag square sheet, which was synthesized via using octylamine as reductant and capping agent. (c) HRTEM image of obtained *hcp/fcc* Au@Ag square sheets.

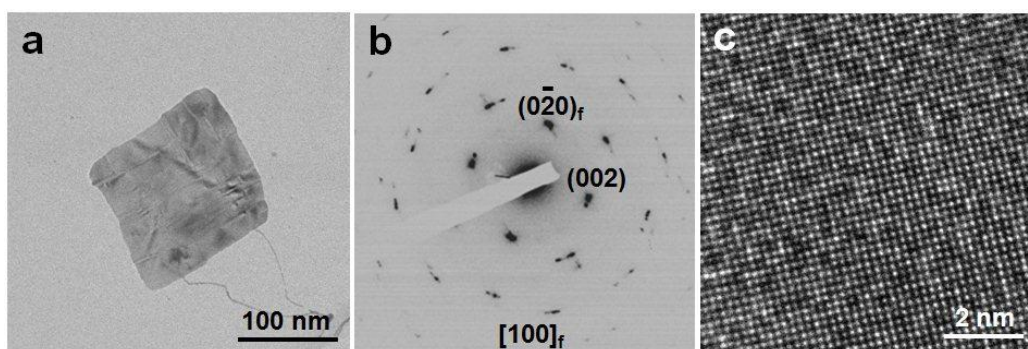


Figure 4-35. (a) TEM image and (b) SAED pattern along $[100]_f$ zone axis of an *fcc* Au@Ag square sheet, which was obtained by using dioctylamine as reductant and capping agent. (c) HRTEM image of obtained *fcc* Au@Ag square sheets.

The observations mentioned above reveal that oleylamine molecules played a critical role in modulating crystal phases of obtained Au@Ag square sheets. To further investigate the influence of surfactants, we executed the control experiments by changing the surfactants from oleylamine to octylamine (belongs to primary amine) and dioctylamine (belongs to secondary amine) as the reductants and capping agents for the epitaxial growth of Ag onto *hcp* AuSSs. The experimental results demonstrated that the octylamine-induced deposition of Ag result in the formation of $(110)_h/(101)_f$ -orientated *hcp/fcc* Au@Ag square sheets (Figure 4-34), similar to that obtained by oleylamine (Figure 4-24), while the dioctylamine-induced reduction of Ag led to formation of $(100)_f$ oriented *fcc* Au@Ag square sheets (Figure 4-35). These experimental phenomena indicated that primary amines may benefit formation of *hcp* containing nanostructures, which is in good agreement with the former studies indicating that primary amines can favor the growth of hexagonal wurtzite structures in some semiconductor nanostructures, e.g. GaP¹⁴⁰. Based on the above discussions, the kind of surfactants used for the deposition of Ag helped to control the kind of structure evolution,

which is most probably caused via the interplay of the adhesive energy of metal structures and surfactant-metal bonding energy^{141,142}.

4.2.5 Synthesis and Characterization of Face-Centered Cubic Au@Pt Nanosheets

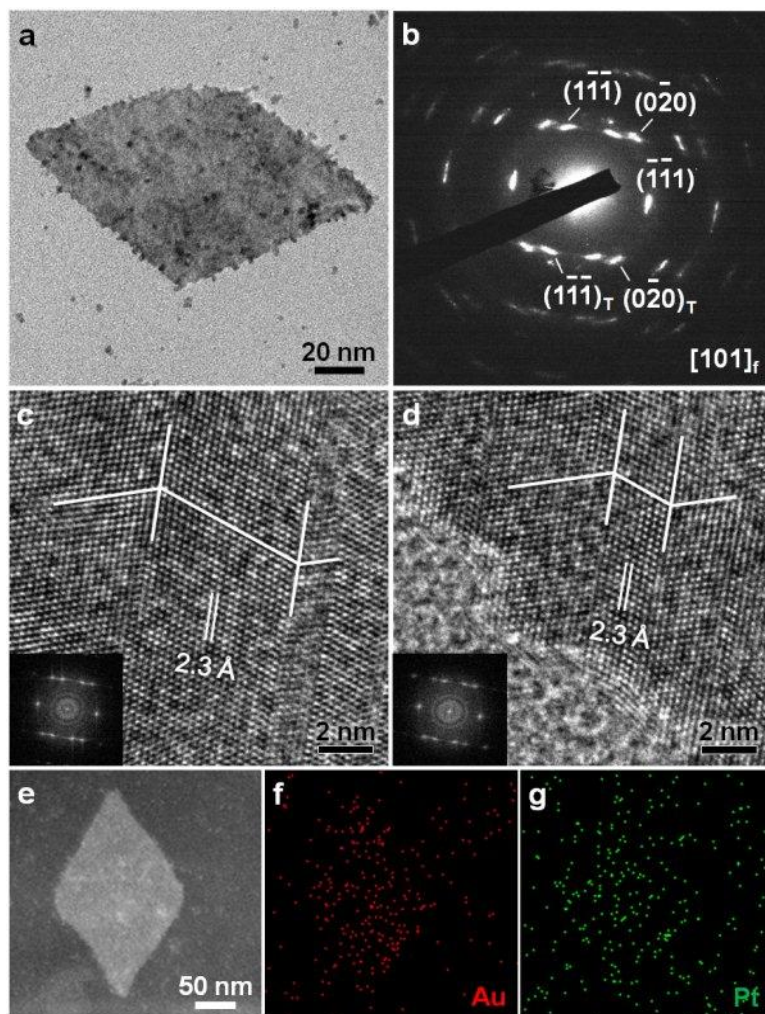


Figure 4-36. (a) TEM image and (b) SAED pattern of a $(101)_f$ -orientated *fcc* Au@Pt rhombic nanosheet. (c,d) HRTEM images of an *fcc* Au@Pt rhombic nanosheet collected from the center and edge areas, respectively. Insets in (c,d): FFT patterns of the HRTEM images in (c,d). (e) HAADF-STEM image and (f,g) STEM-EDS element mappings of a $(101)_f$ -oriented *fcc* Au@Pt rhombic nanosheet.

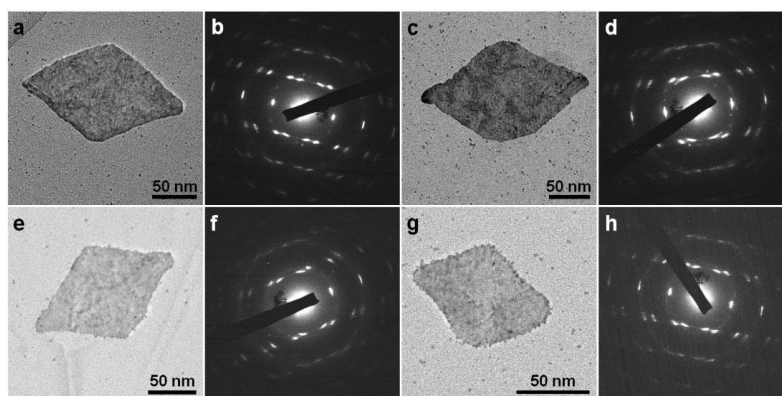


Figure 4-37. (a,c,e,g) TEM images and (b,d,f,h) SAED patterns of obtained *fcc* Au@Pt rhombic nanosheets.

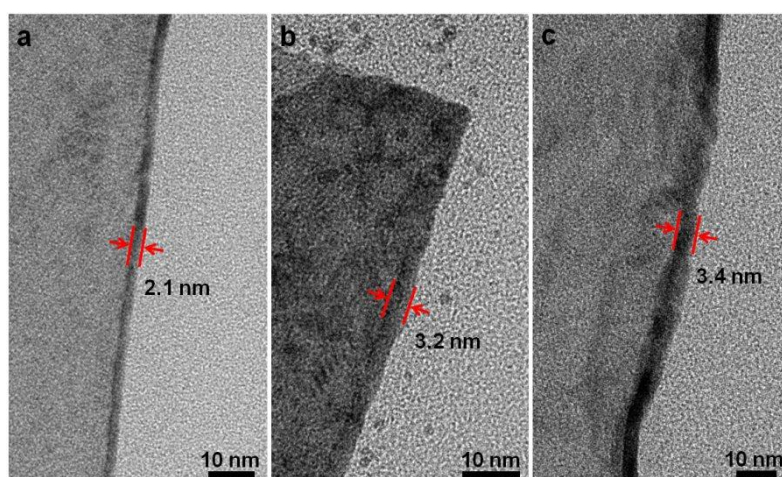


Figure 4-38. TEM images of a folded (a) *hcp* AuSS, (b) *fcc* Au@Pt rhombic nanosheet, and (c) *fcc* Au@Pd rhombic nanosheet.

The bimetallic *fcc* Au@Pt nanosheet was prepared via the deposition of Pt on the *hcp* AuSSs with NaBH_4 as the reducing agent. Surprisingly, the shape of nanosheets changed from square to rhombic shapes after the coating of Pt on *hcp* AuSSs (Figure 4-36a and Figure 4-37). The thickness of the as-prepared Au@Pt rhombic nanosheets is measured as 3.5 ± 0.7 nm by TEM (Figure 4-38b). Importantly, the electron diffraction reveals the crystal structure of obtained Au@Pt rhombic nanosheets is *fcc* phase with an unusual orientation of $(101)_f$. It

should be pointed out that almost all of the formerly prepared two-dimension (2D) *fcc* metal NCs demonstrate a common orientation of $(111)_f^{2,125,131,137,143}$. The SAED pattern collected along $[101]_f$ zone axis of obtained *fcc* Au@Pt rhombic nanosheets are demonstrated in Figure 4-36b and Figure 4-37. The diffraction spots ascribed to twins are also found and noted with a subscript of “T” (Figure 4-36b). The dark-field TEM image acquired with the $(1\bar{1}\bar{1})_f$ diffraction spot further suggests that the twins randomly distribute over the entire structure of *fcc* Au@Pt rhombic nanosheets (Figure 4-39).

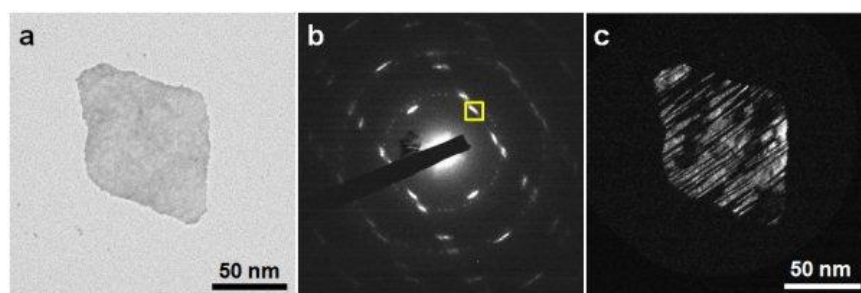


Figure 4-39. (a) TEM image and (b) SAED pattern of an *fcc* Au@Pt rhombic nanosheet. (c) Dark-field TEM image taken with $(1\bar{1}\bar{1})_f$ diffraction spot as marked in (b).

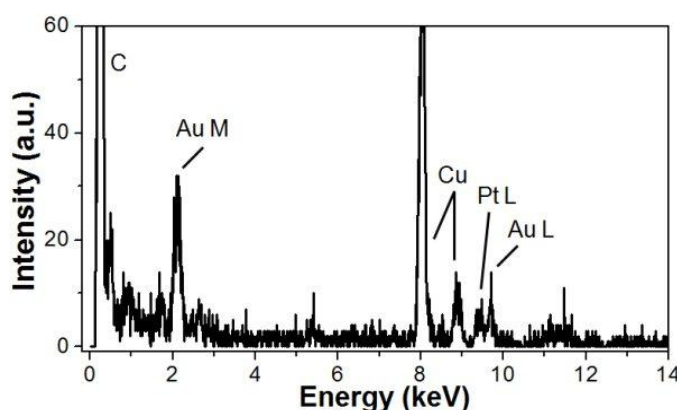


Figure 4-40. STEM-EDS spectrum of obtained *fcc* Au@Pt rhombic nanosheets. The average atomic ratio between Au and Pt is 1: 1.

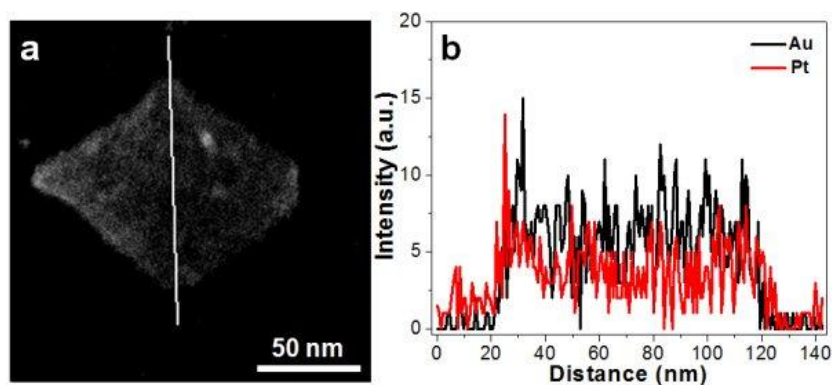


Figure 4-41. (a) HAADF-STEM image and (b) STEM-EDS line scanning analysis of obtained *fcc* Au@Pt rhombic nanosheets.

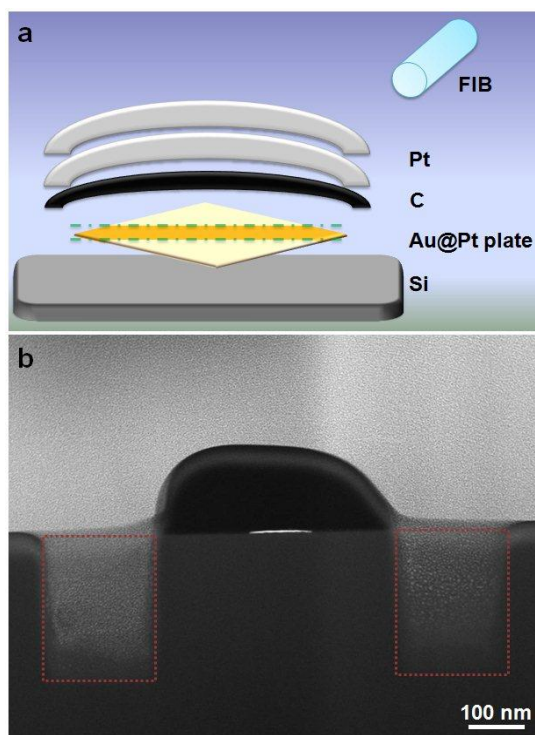


Figure 4-42. (a) Schematic illustration for fabrication of cross sections of *fcc* Au@Pt rhombic nanosheets. The green dashed lines show the cutting direction with FIB. (b) The HAADF-STEM image of obtained cross section of an *fcc* Au@Pt rhombic nanosheet. The regions in the two red rectangles indicate the alignment marks produced in the process for preparation of cross sections of *fcc* Au@Pt rhombic nanosheets.

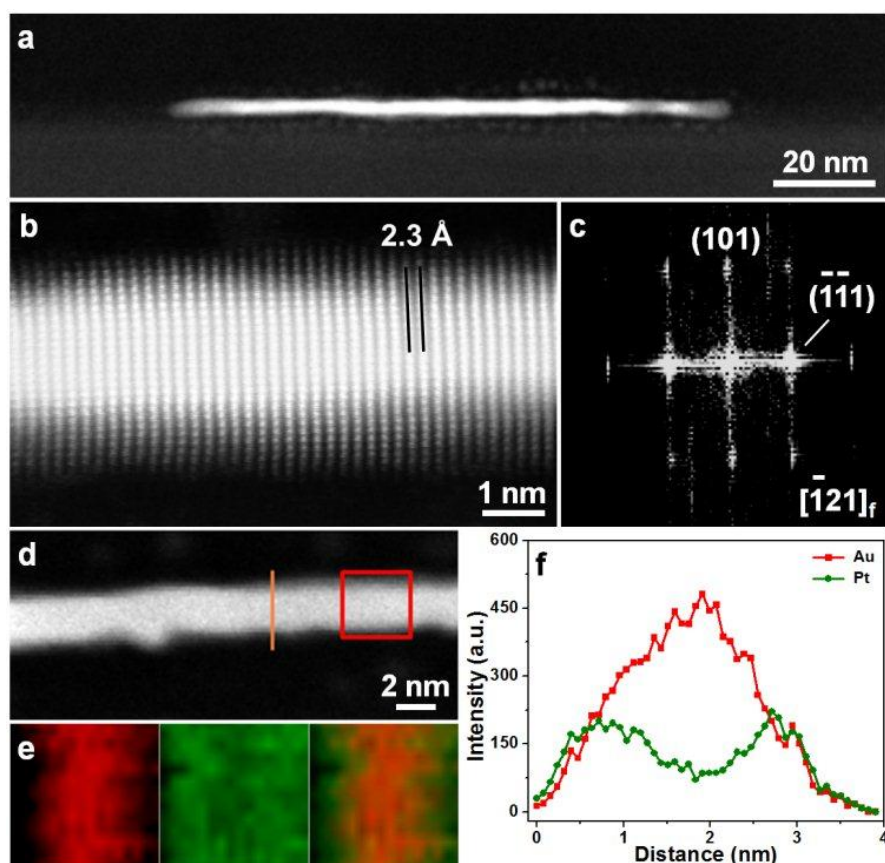


Figure 4-43. (a) Low-magnification and (b) aberration-corrected HAADF-STEM images of cross section of an *fcc* Au@Pt rhombic nanosheet. (c) FFT pattern of HAADF-STEM image in (b). (d) HAADF-STEM image of cross section of the *fcc* Au@Pt rhombic nanosheet. (e) STEM-EDS element mapping of Au (in red color) and Pt (in green color), and the overlapped image. (f) STEM-EDS line scanning plots of the selected areas indicated by rectangle and line in (d), respectively.

Figure 4-36c,d demonstrate the HRTEM images of an *fcc* Au@Pt rhombic nanosheets collected from the center and edge areas. An inter-plane lattice distance of 2.3 Å is measured from the HRTEM images, which is assigned to *fcc*{111} planes. HRTEM image clearly demonstrates the twin structures, which is in good agreement with the results of SAED and dark-field TEM (Figure 4-36b and Figure 4-39). The chemical composition of the as-prepared Au@Pt rhombic nanosheets is

measured by the STEM-EDS (Figure 4-40), giving an average atomic ratio between Au and Pt of 1: 1. A typical HAADF-STEM image of an *fcc* Au@Pt rhombic nanosheet and the STEM-EDS elemental mappings clearly indicate both Au and Pt are uniformly distributed in obtained *fcc* Au@Pt rhombic nanosheets (Figure 4-36e-g), which is proved by STEM-EDS line scanning analysis of as-prepared *fcc* Au@Pt rhombic nanosheets (Figure 4-41).

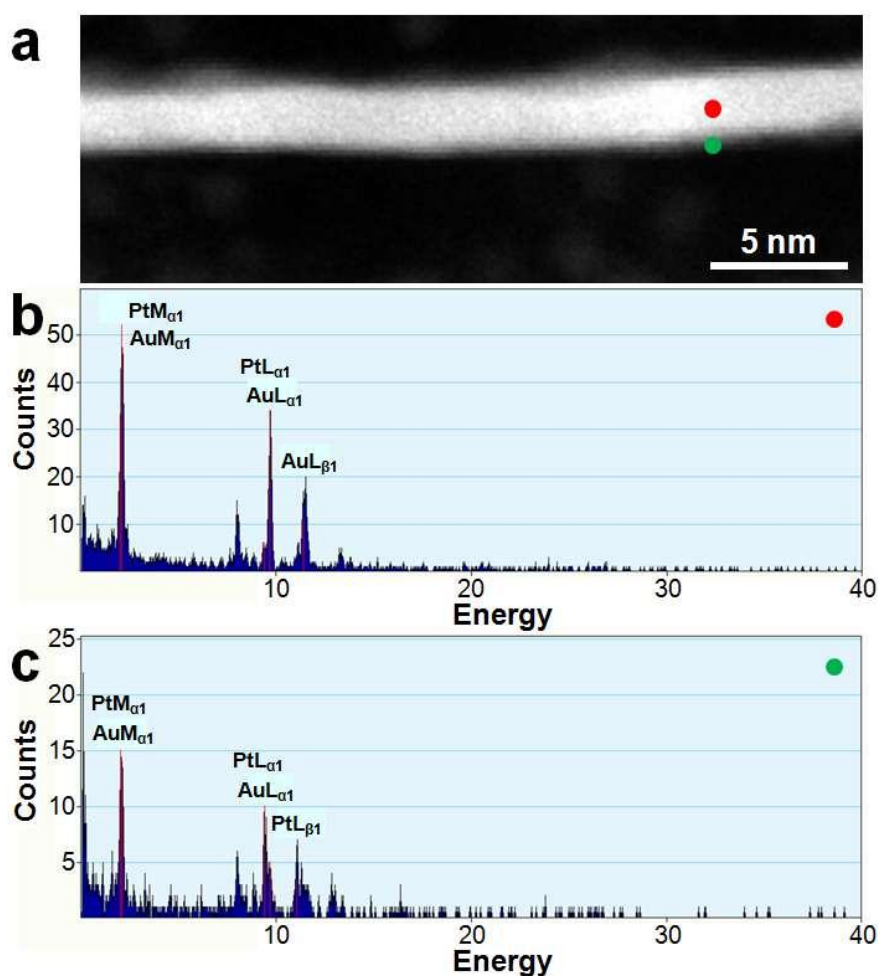


Figure 4-44. (a) HAADF-STEM image of a cross section of an *fcc* Au@Pt rhombic nanosheet. (b,c) Selected-point STEM-EDS spectra taken from the regions marked by red and green dots in (a), respectively.

To further study the crystal structure of as-prepared *fcc* Au@Pt rhombic nanosheet, FIB was applied to cut it along its long diagonal (see Figure 4-42 for details), in order to investigate its cross section (Figure 4-43a,b,d). STEM-EDS element mappings and the line scanning profiles of cross section suggest the whole surface of *fcc* Au nanosheets is covered Pt, resulting in the formation of a core-shell structure (Figure 4-43e,f), which is also identified by the selected point STEM-EDS study (Figure 4-44). Aberration-corrected HAADF-STEM image of cross section of the as-prepared *fcc* Au@Pt rhombic nanosheets indicates the continuous lattice fringes extending from the inside Au core to outside Pt shell (Figure 4-43b), suggesting epitaxial relationship between Au and Pt. A lattice spacing of 2.3 Å is attributed to *fcc* {111} planes of the as-prepared Au@Pt rhombic nanosheets. The FFT pattern is in good agreement with the SAED pattern along *fcc*[$\bar{1}21$] zone axis (Figure 4-43c), which further identifies a complete phase transformation of AuSSs from *hcp* to *fcc* after the coating of Pt.

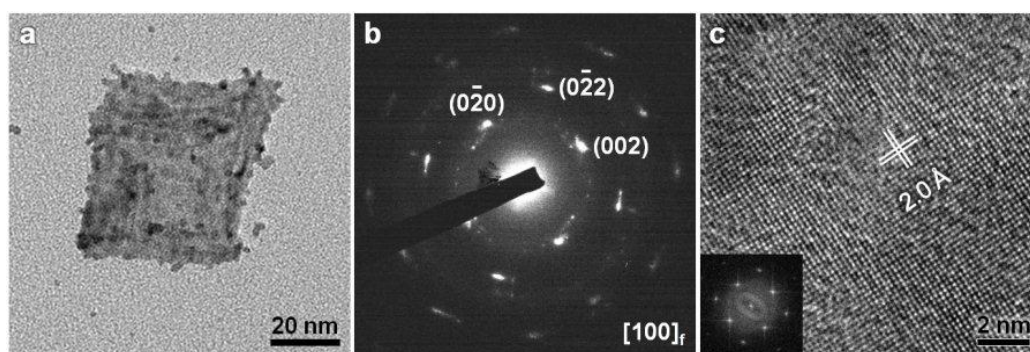


Figure 4-45. (a) TEM image and (b) SAED pattern of an *fcc* Au@Pt square nanosheet. (c) HRTEM image of an *fcc* Au@Pt square nanosheet. Inset in (c): FFT pattern of HRTEM image shown in (c).

Interestingly, besides the *fcc* Au@Pt rhombic nanosheets mentioned above, a tiny amount of Au@Pt square nanosheets (yield is < 10%) was also found in the

final products (Figures 4-45 to 4-47). Figure 4-45a demonstrates the typical TEM image of an Au@Pt square nanosheet. SAED pattern indicates that the as-prepared Au@Pt square nanosheets exhibit the *fcc* structure with an orientation of $(100)_f$, which is further confirmed by HRTEM images (Figure 4-45b,c). A lattice spacing of 2.0 Å is assigned to *fcc* {100} planes (Figure 4-45c).

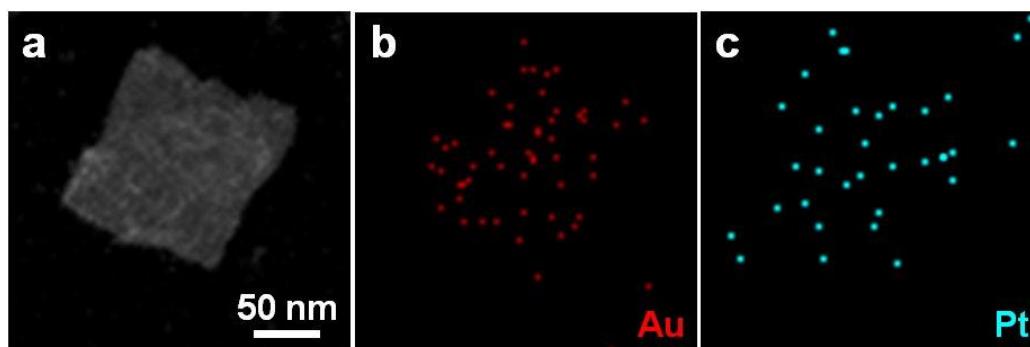


Figure 4-46. (a) HAADF-STEM image and (b,c) STEM-EDS element mappings of an *fcc* Au@Pt square nanosheet.

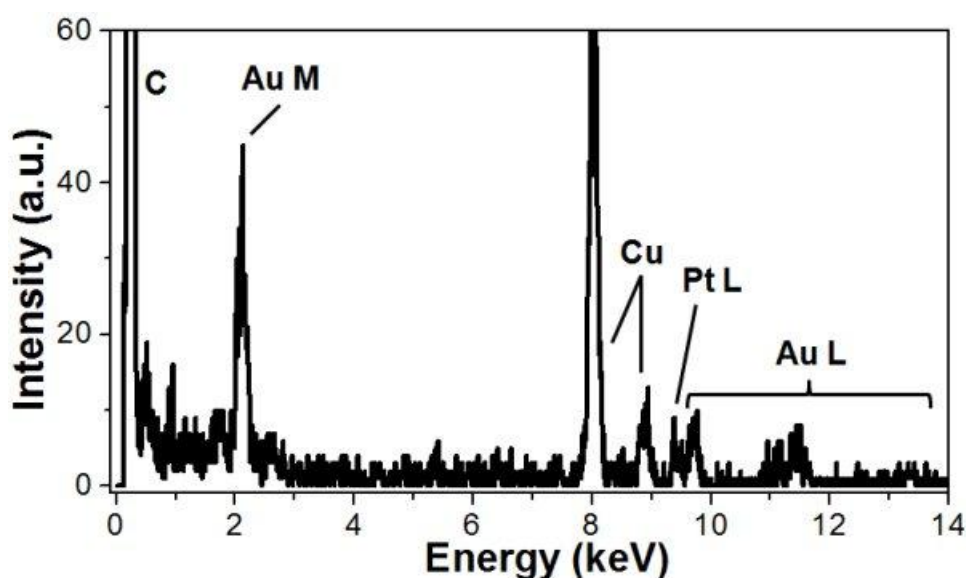


Figure 4-47. STEM-EDS spectrum of *fcc* Au@Pt square nanosheets. The average atomic ratio between Au and Pt is 1.0: 0.7.

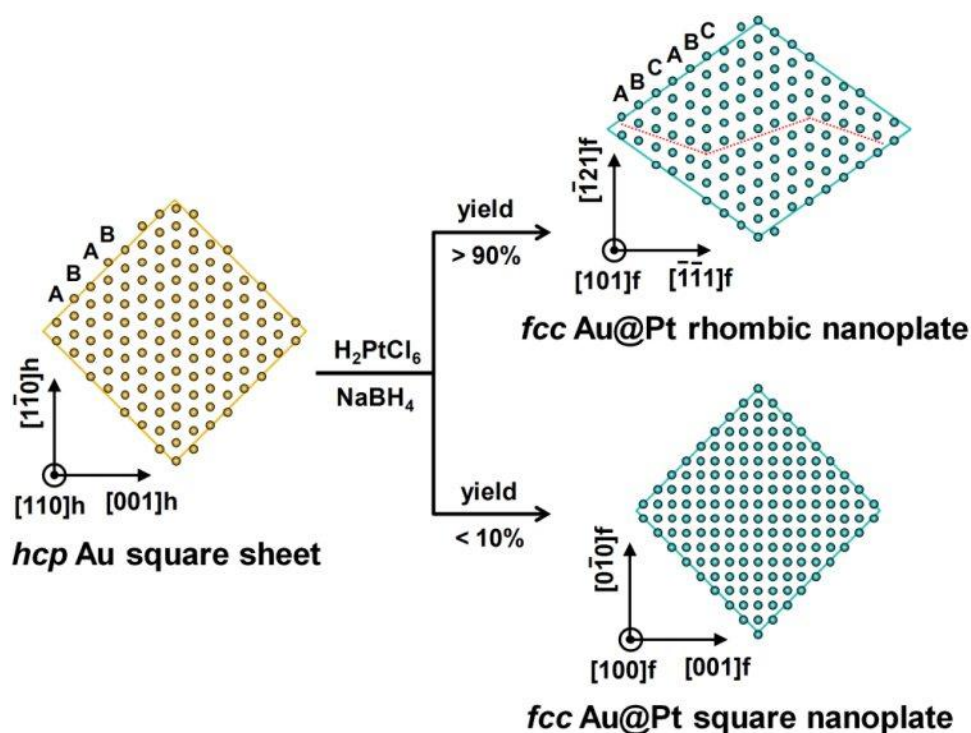


Figure 4-48. The scheme illustrating the synthesis of $(101)_f$ oriented fcc Au@Pt rhombic nanosheets with twin structures (indicated by dashed red line) from $(110)_h$ oriented hcp AuSSs (top panel), along with the formation of a tiny amount of $(100)_f$ oriented fcc Au@Pt square nanosheets (bottom panel).

The top panel of Figure 4-48 schematically illustrates the structure and morphology evolution of hcp AuSSs caused by the epitaxial deposition of a thin Pt layer, i.e. the transformation from the initial $(110)_h$ oriented hcp AuSSs to obtained $(101)_f$ oriented fcc Au@Pt rhombic nanosheets. The fcc and hcp polytypes are different from the packing sequence of the close-packed planes with the repeated ABC stacking along $[111]_f$ direction and AB stacking along $[001]_h$ direction, respectively. This kind of phase change can be realized by the transition of stacking order of the close-packed planes, leading to the formation of lots of crystal defects (such as twins, dislocations, and stacking faults) and shape transformation^{95,144,145}. Furthermore, the nanostructure's orientation regarding to

its close-packed directions (i.e. $[111]_f$ and $[001]_h$ directions) maintains^{19,145}, which is in good agreement with the aforementioned experimental results (Figure 4-36 and Figure 4-37). Differently, the close-packed directions (i.e. $[111]_f$ and $[001]_h$ directions) have changed in the another structure transition from $(110)_h$ oriented *hcp* AuSSs to the obtained $(100)_f$ oriented *fcc* Au@Pt square nanosheets (Figure 4-48, bottom panel).

Theoretical and experimental investigations have suggested that crystal phases of inorganic NC can be largely influenced by surface energy, which dominates or contributes a lot to total systemic energy^{17,19,145,146}. For example, the *hcp* Ag^{16,17} NPs and *fcc* Ru¹⁸ have been obtained even though their bulk counterparts are *fcc* and *hcp* structures, respectively. In the present work, the epitaxial coating of Pt on the *hcp* AuSSs led to the increase of their thicknesses (Figure 4-43 and Figure 4-38b) and thus resulted to the decrease of the surface area-to-volume ratio, which may induce instability of initial *hcp* phase and hence its change from *hcp* to *fcc* structures.

Besides, it has been widely found that the epitaxial strain, induced by the crystal lattice mismatch between the underlying substrate and epitaxial thin film, plays an important role in the final structure of the deposited thin film^{144,147}. Recently, a study reveals that for the CdS@ZnS core-shell nanospheres with a shell thickness of merely 7.5-monolayered ZnS, 7% crystal lattice mismatch between the CdS core and the ZnS shell produced a radial pressure as large as 4 GPa on the CdS core¹⁴⁸. In the current contribution, crystal lattice mismatch between close-packed planes of *fcc* Pt ($\{111\}_f$ plane, $d = 2.26 \text{ \AA}$, COD no. 9013417) and *hcp* Au ($\{001\}_h$ plane, $d = 2.4 \text{ \AA}$, refer to the former work¹⁹) is around 5.8%. It should be pointed out that thickness of *hcp* AuSSs is just about 1.8

nm (Figure 4-38a), i.e. ~ 12 atomic layers of Au. Hence the influence of epitaxial strain induced by the outside Pt shell on the crystal phase of the *hcp* AuSSs may be significantly large. In addition, it has been revealed that the energy differences among body-centered cubic (*bcc*), *hcp* and *fcc* crystal structures is very small in many noble and transition metals¹⁴⁹. Therefore, it is proposed that the phase change of the *hcp* AuSSs caused by epitaxial deposition of Pt is probably a result of the interplay among phase stability, surface energy and epitaxial strain. The underlying reason for coexistence of two types of structure change caused by Pt deposition on the *hcp* AuSSs, i.e. $(110)_h$ oriented *hcp* Au nanosheets to $(100)_f$ and $(101)_f$ oriented *fcc* Au@Pt nanosheets, still remains unclear, which needs further study.

4.2.6 Synthesis and Characterization of Face-Centered Cubic Au@Pd Nanosheets

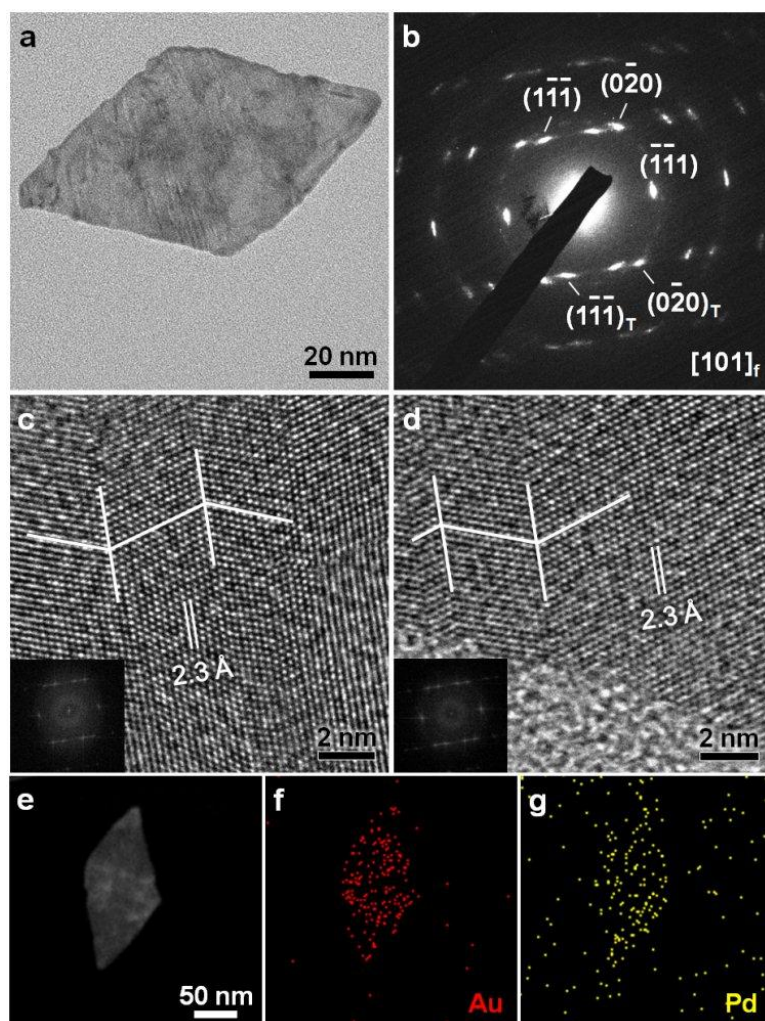


Figure 4-49. (a) TEM image and (b) SAED pattern of a $(101)_f$ -orientated *fcc* Au@Pd rhombic nanosheet. (c,d) HRTEM images of an *fcc* Au@Pd rhombic nanosheet collected from center and edge areas, respectively. Insets in (c,d): FFT patterns of the HRTEM images in (c,d). (e) HAADF-STEM image and (f,g) STEM-EDS element mappings of a $(101)_f$ -oriented *fcc* Au@Pd rhombic nanosheet.

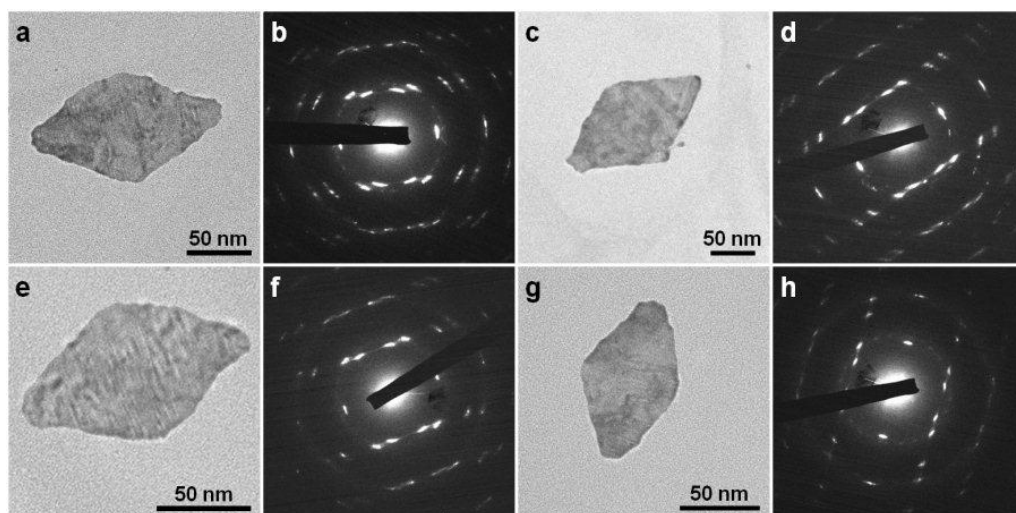


Figure 4-50. (a) (a,c,e,g) TEM images and (b,d,f,h) SAED patterns of obtained *fcc* Au@Pd rhombic nanosheets.

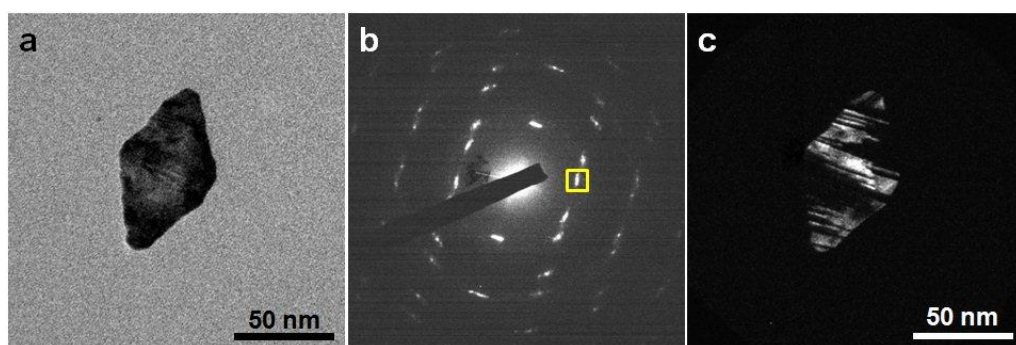


Figure 4-51. (a) TEM image and (b) SAED pattern of an *fcc* Au@Pd rhombic nanosheet. (c) Dark-field TEM image taken with $(1\bar{1}\bar{1})_f$ diffraction spot as marked in (b).

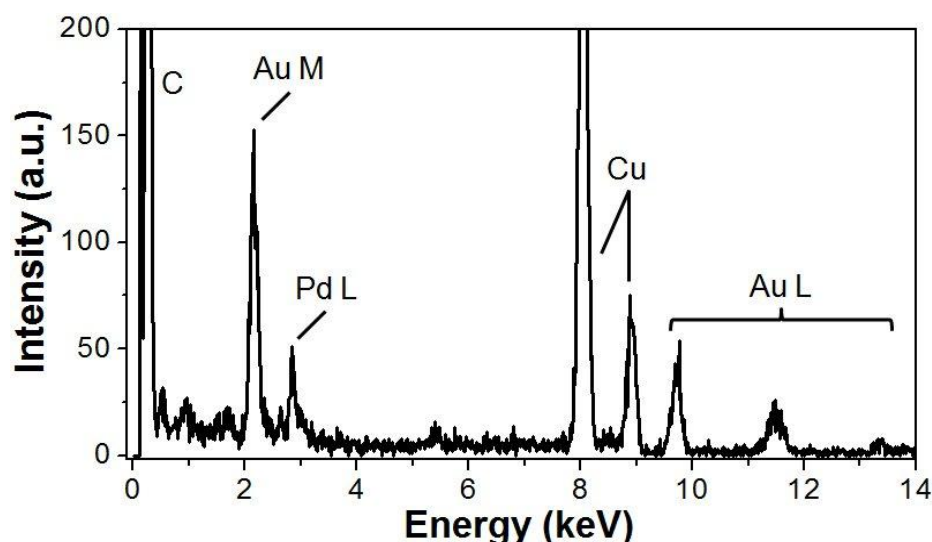


Figure 4-52. STEM-EDS spectrum of *fcc* Au@Pd rhombic nanosheets. The average atomic ratio between Au and Pt is 1.0: 0.8.

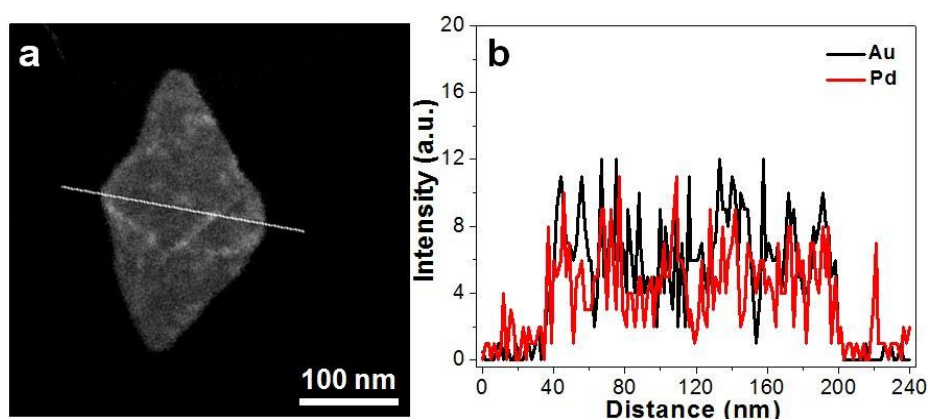


Figure 4-53. (a) HAADF-STEM image and (b) STEM-EDS line scanning analysis of an *fcc* Au@Pd rhombic nanosheet.

Importantly, the epitaxial deposition of Pd on the *hcp* AuSSs can also cause a structure change, leading to the production of $(101)_f$ oriented *fcc* Au@Pd rhombic nanosheets (Figures 4-49 and 4-50). The *fcc* phase of Au@Pd rhombic nanosheets with lots of twin structures is revealed by SAED pattern (Figure 4-49b), which is confirmed by dark-field TEM image acquired from the $(1\bar{1}\bar{1})_f$ diffraction spot (Figure 4-51). HRTEM images collected perpendicular to basal plane of the

obtained Au@Pd rhombic nanosheets further suggest the presence of twins and an unusual orientation of $(101)_f$ (Figure 4-49c,d). The thickness of as-prepared *fcc* Au@Pd rhombic nanosheets is measured as 3.4 ± 0.8 nm by TEM (Figure 4-38c). The STEM-EDS spectrum reveals the coexistence of Au and Pd (Figure 4-52) with an average Au/Pt atomic ratio of 1/0.8. Typical HAADF-STEM image of an *fcc* Au@Pd rhombic nanosheet is demonstrated in Figure 4-49e. The STEM-EDS element mappings (Figure 4-49f,g) reveal both Pd and Au are homogeneously distributed in as-prepared *fcc* Au@Pd rhombic nanosheets, which is further identified by STEM-EDS line scanning analysis (Figure 4-53). Moreover, a tiny amount of $(100)_f$ oriented *fcc* Au@Pd square nanosheets with a yield of $< 10\%$ was also observed in the final products (Figures 4-54 and 4-55), similar to the aforementioned results of Pt coating on *hcp* AuSSs (Figure 4-45).

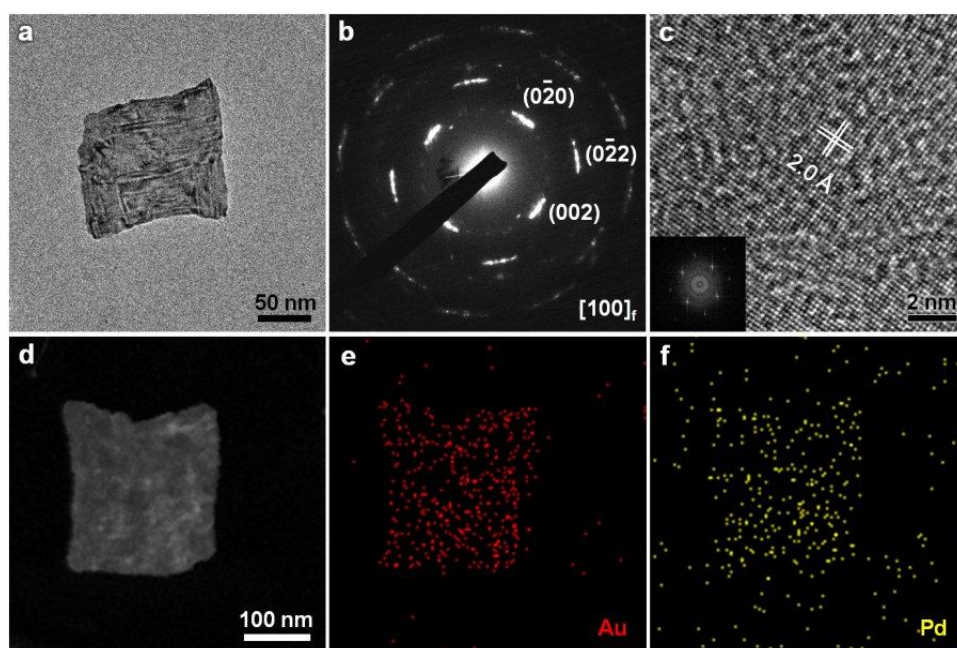


Figure 4-54. (a) TEM image, (b) SAED pattern, and (c) HRTEM image of an *fcc* Au@Pd square nanosheet. (d) HAADF-STEM image and (e,f) STEM-EDS element mappings of an *fcc* Au@Pd square nanosheet.

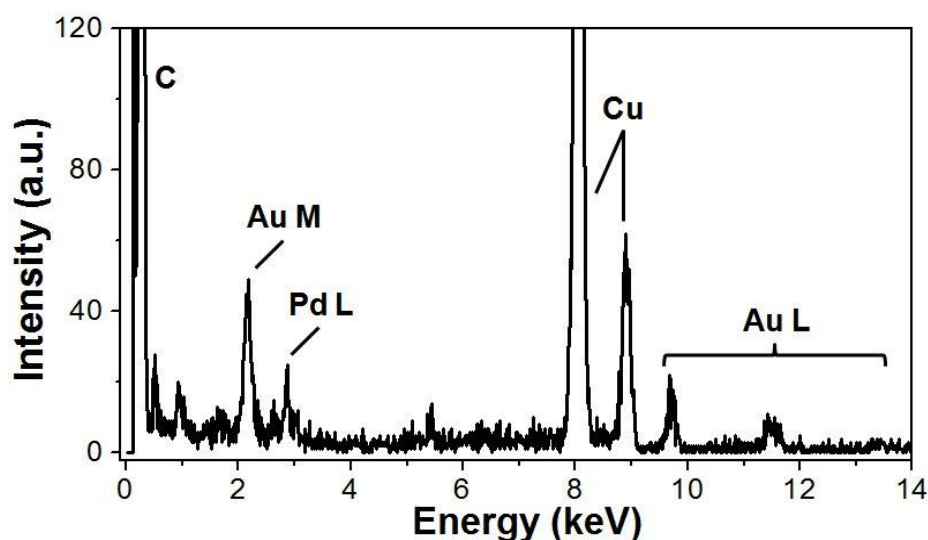


Figure 4-55. STEM-EDS spectrum of *fcc* Au@Pd square nanosheets. The average atomic ratio between Au and Pt is 1.0: 0.9.

4.1.7 Monochromated Electron Energy Loss Spectroscopy Measurement of Individual Face-Centered Cubic Au@Ag Square Sheets

The LSPR property of individual *fcc* Au@Ag square sheets on GO sheet was studied by the monochromated EELS in STEM. In a typical experiment, the EELS characterization of individual *fcc* Au@Ag square sheets was executed by positioning the focused electron beam next to (2–3 nm) edge or corner regions of *fcc* Au@Ag square sheet on GO sheet to excite its LSPR (see Figure 4-13a for details). A control EELS spectrum of GO sheet was also acquired at about 500 nm away from *fcc* Au@Ag square sheets, where merely GO sheet presents (Figure 4-56, the blue curve). Remarkably, EELS spectrum of the corner region of *fcc* Au@Ag square sheet demonstrates a strong LSPR absorption peak at 0.61 eV (or 2033 nm) (Figure 4-56, the red curve). EELS spectrum of the edge region of *fcc* Au@Ag square sheet on GO sheet demonstrates a similar LSPR absorption nature,

which further proves its LSPR absorption in infrared range (Figure 4-56, the green curve). Such a strong IR absorption is derived from the in-plane surface plasmon resonance of two-dimensional *fcc* Au@Ag square sheet with relatively large edge length-to-thickness aspect ratio^{6,120,121,123,124}.

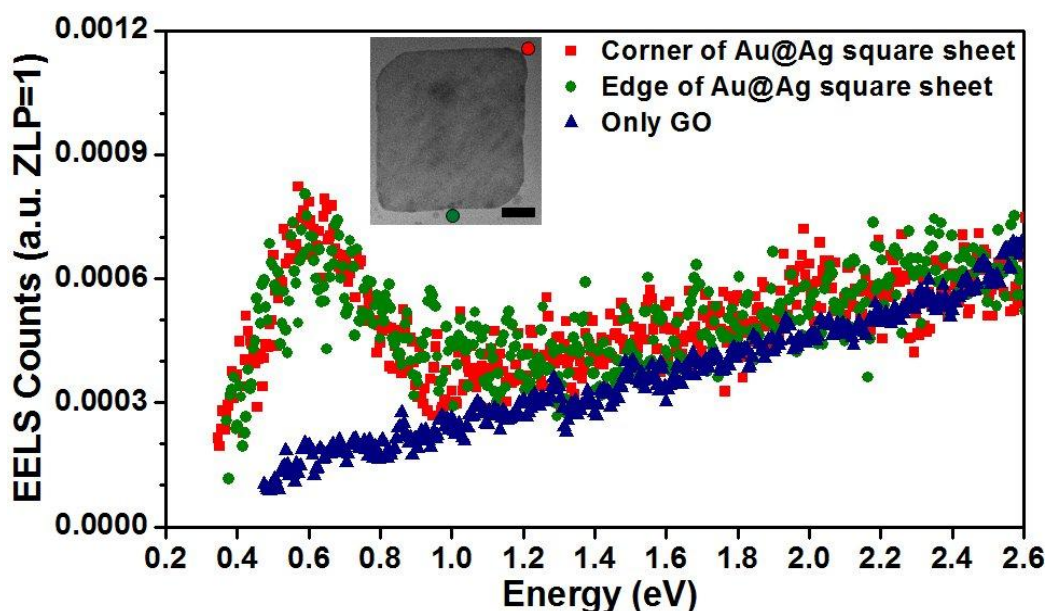


Figure 4-56. EELS spectra collected from an individual Au@Ag square sheet on the GO sheet (excited next to edge and corner of an *fcc* Au@Ag square sheet and the GO sheet. Inset: STEM image of a selected Au@Ag square sheet on the GO sheet (scale bar, 20 nm), in which positions of focused electron beam are indicated.

4.2.8 Short Summary

In this section, a simple metal coating method has been established to synthesize a series of unprecedented noble bimetallic nanosheets, i.e. (100)_f oriented *fcc* Au@Ag square sheets, (110)_h/(101)_f-oriented polytypic *hcp/fcc* Au@Ag square sheets, (101)_f-oriented *fcc* Au@Pt and Au@Pd rhombic nanosheets, (100)_f-oriented Au@Pt and Au@Pd square nanosheets from *hcp* AuSSs at ambient

condition. Monochromated EELS reveals the ultra-strong LSPR absorption of *fcc* Au@Ag square sheets in infrared range. This work indicates the wide possibilities in synthesis of bimetallic nanomaterials based on the structure change of inorganic nanomaterials with small dimensions.

4.3 Colloidal Synthesis of 4H Hexagonal Au Nanoribbons

4.3.1 Introduction

The control of crystal phases is one of the big challenges in the synthesis of advanced inorganic nanomaterials^{93,150,151}. Polymorphism phenomena are commonly observed in II-VI, IV, III-V and transition metal oxide semiconductor nanomaterials^{119,152-155}. The crystal phase of semiconductor nanomaterials is usually determined by experimental factors, e.g. the interaction between crystal nuclei and capping agents¹⁴⁰, the reaction temperature¹⁵² and pressure^{119,155}, crystal size^{152,154} and solvent system¹⁵⁶. Despite the polymorphs of a certain semiconductor nanostructure have an identical chemical composition, their physical and chemical properties may be greatly different from one to the other^{93,153}. For instance, the band gap of wurtzite SiC (3.33 eV) is much bigger than that of the zinc-blende counterpart (2.39 eV)¹⁵³. Different from the semiconductor nanomaterials, structure control over noble metals still remains a huge challenge, particularly for the noble metal nanostructures obtained using the wet-chemical synthetic methods.

Gold (Au) nanomaterials have attracted widely interest due to their unique physical and chemical properties for various applications, such as catalysis, bio-sensing, surface-enhanced Raman scattering (SERS), and biomedicine^{1,2,157}. Several decades ago, well-dispersed Au nanoparticles (NPs) were obtained via reduction of HAuCl_4 with the sodium citrate¹²⁵. After that, many methods, e.g. the porous aluminum anodic oxide-directed hard-template approach¹⁵⁸, surfactant-driven soft-template synthesis¹⁵⁹ and seed-mediated synthetic method¹⁶⁰, have been well developed for the synthesis of many anisotropic Au nanomaterials. As a result, well-defined Au nanomaterials with various shapes, such as nanorods^{159,160},

nanowires^{158,161-163}, nanoplates^{120,164}, nanoribbons¹⁶⁵, and nanopolyhedra^{11,166}, have been successfully achieved. While the shape- and size- controlled synthesis of Au nanomaterials can be easily realized, almost all of the Au nanomaterials reported to date usually crystallize in the face-centered cubic (*fcc*) phase. Recently, Huang *et al.* firstly reported the controlled synthesis of hexagonal close-packed (*hcp*, 2H type) Au square sheets¹⁹, which inspires the investigation of novel polytypes of Au and study of their structure manipulation.

In this section, the high-yield colloidal synthesis of hexagonal 4H Au nanoribbons (NRBs), a new metastable phase of Au, has been shown. We found that the 4H phase of Au NRBs can be changed to the *fcc* phase after ligand exchange under ambient conditions. Meanwhile, monochromated electron energy-loss spectroscopy (EELS) demonstrated the existence of well-defined localized surface plasmon resonance (LSPR) absorption on individual 4H Au NRBs. Moreover, it is shown that the 4H hexagonal structure of Pd, Ag, and Pt can also be easily obtained via the direct epitaxial growth of these noble metals onto the as-prepared 4H Au NRB surface.

4.3.2 Synthesis and Characterization of 4H Au Nanoribbons

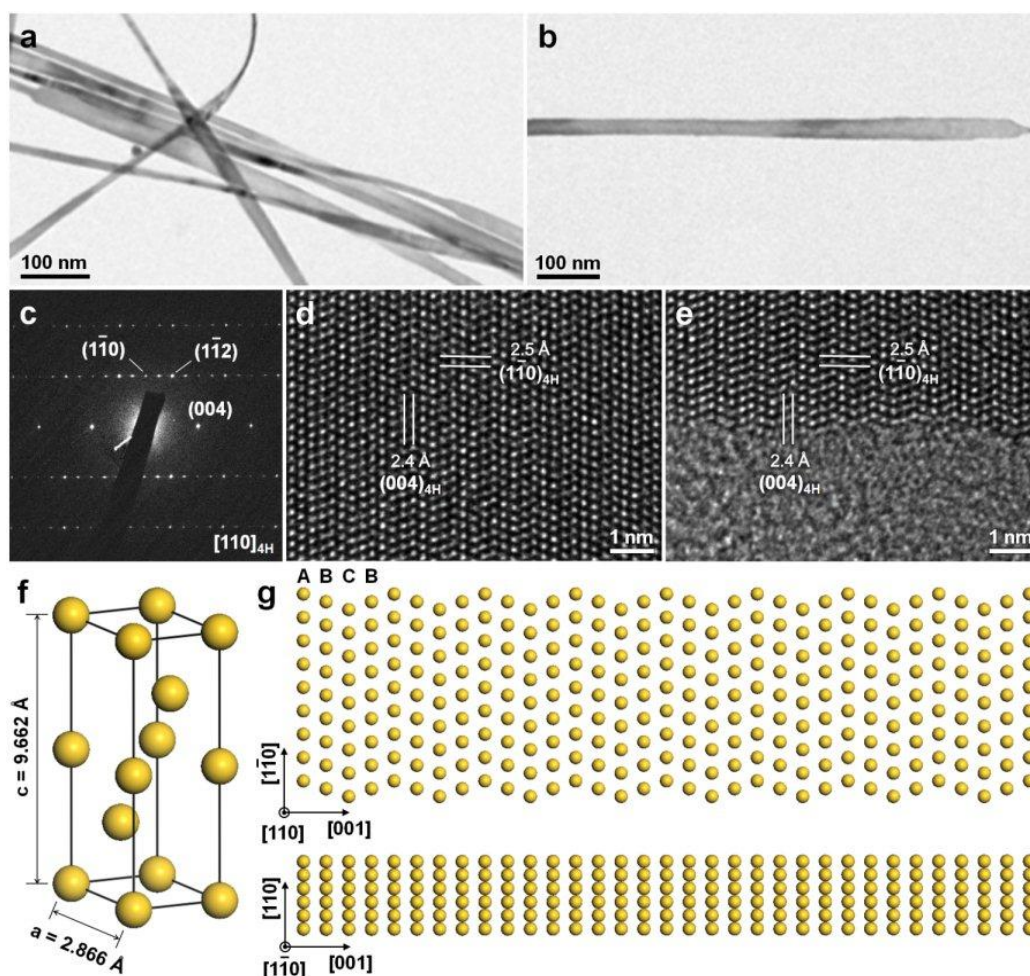


Figure 4-57. (a) TEM image of 4H Au NRs. (b,c) TEM image and SAED pattern collected along $[110]_{4H}$ zone axis of an Au NR. (d,e) Aberration-corrected HRTEM images collected from the center (d) and edge (e) regions of an Au NR, respectively. (f) Schematic illustration for the unit cell of 4H Au. (g) Crystallographic models showing the top (top panel) and side (bottom panel) views of a 4H Au NR.

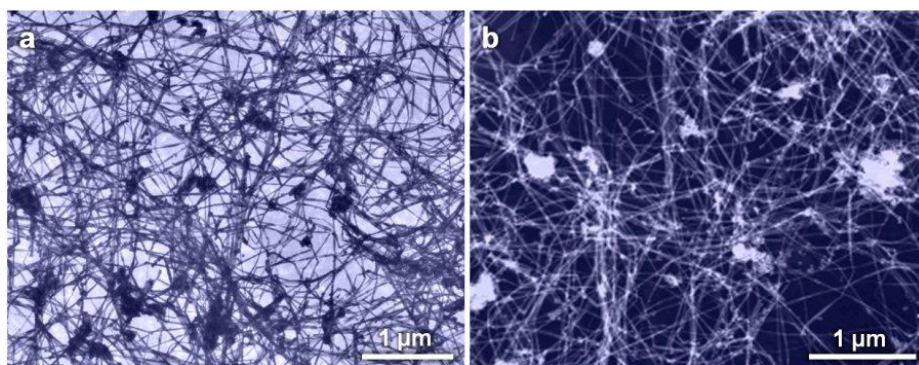


Figure 4-58. (a) TEM and (b) HAADF-STEM images of obtained 4H Au NRBs.

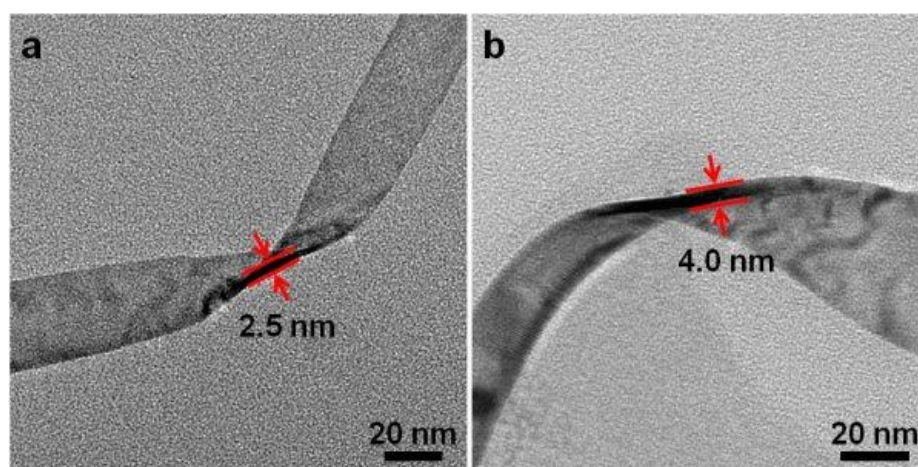


Figure 4-59. TEM images of two folded 4H Au NRBs, showing a thickness of 2.5 nm (a) and 4.0 nm (b), respectively.

The Au NRBs were synthesized by heating the mixture consisted of oleylamine, HAuCl_4 , 1,2-dichloropropane and hexane in a sealed glass vial at 58 °C for 16 h. The transmission electron microscope (TEM) images indicate the length and width of the as-prepared Au NRBs are 0.5–6.0 μm and 15–61 nm, respectively (Figure 4-57a,b and Figure 4-58). The thickness of the obtained Au NRBs is measured as 2–6 nm by TEM (Figure 4-59), which is further identified by atomic force microscopy (AFM) (Figure 4-60). The scanning TEM-energy dispersive X-ray spectrum (STEM-EDS) suggests that the chemical composition of the obtained

NRBs is pure of Au (Figure 4-61). The surface of Au NRBs is protected by the oleylamine, as revealed by X-ray photoelectron spectroscopy (XPS) investigation (Figure 4-62). It should be pointed out that the introduction of 1,2-dichloropropane is of paramount importance to the successful synthesis of Au NRBs. Without 1,2-dichloropropane, merely twinned *fcc* Au NPs and tiny amount of ultrathin Au nanowires (NWs) were attained (Figure 4-63).

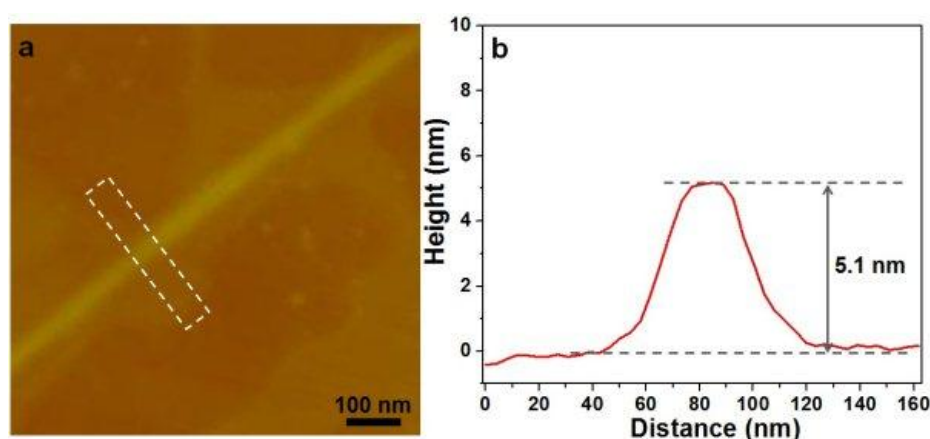


Figure 4-60. (a) AFM image and (b) height analysis of a 4H Au NRB deposited on the Si/SiO₂ substrate.

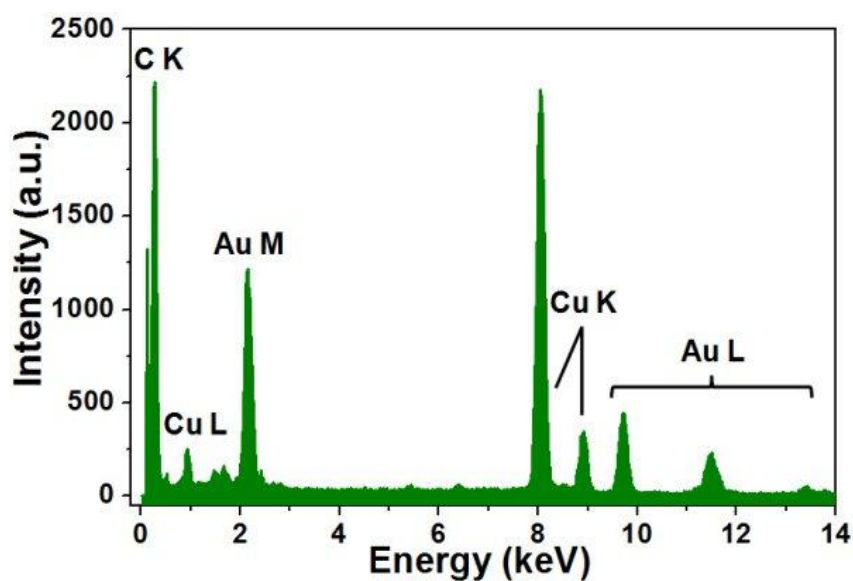


Figure 4-61. STEM-EDS spectrum of obtained 4H Au NRBs.

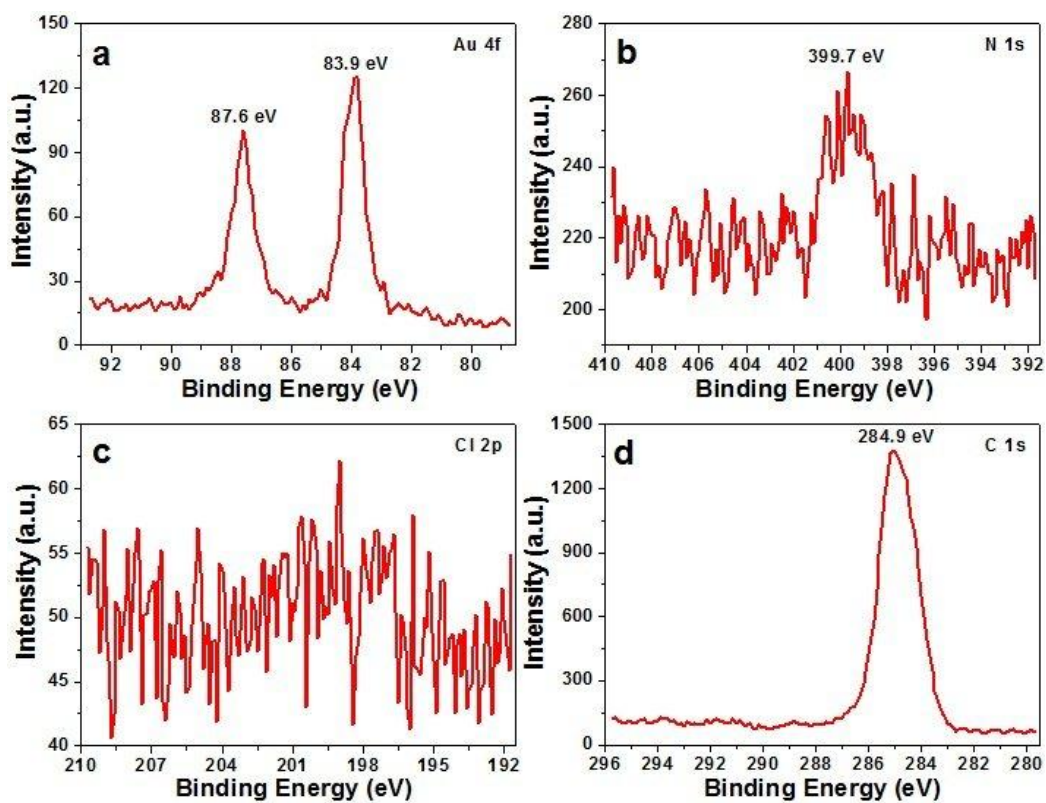


Figure 4-62. XPS spectra of 4H Au NRBs, demonstrating the core level peaks of (a) Au 4f, (b) N 1s, (c) Cl 2p and (d) C 1s.

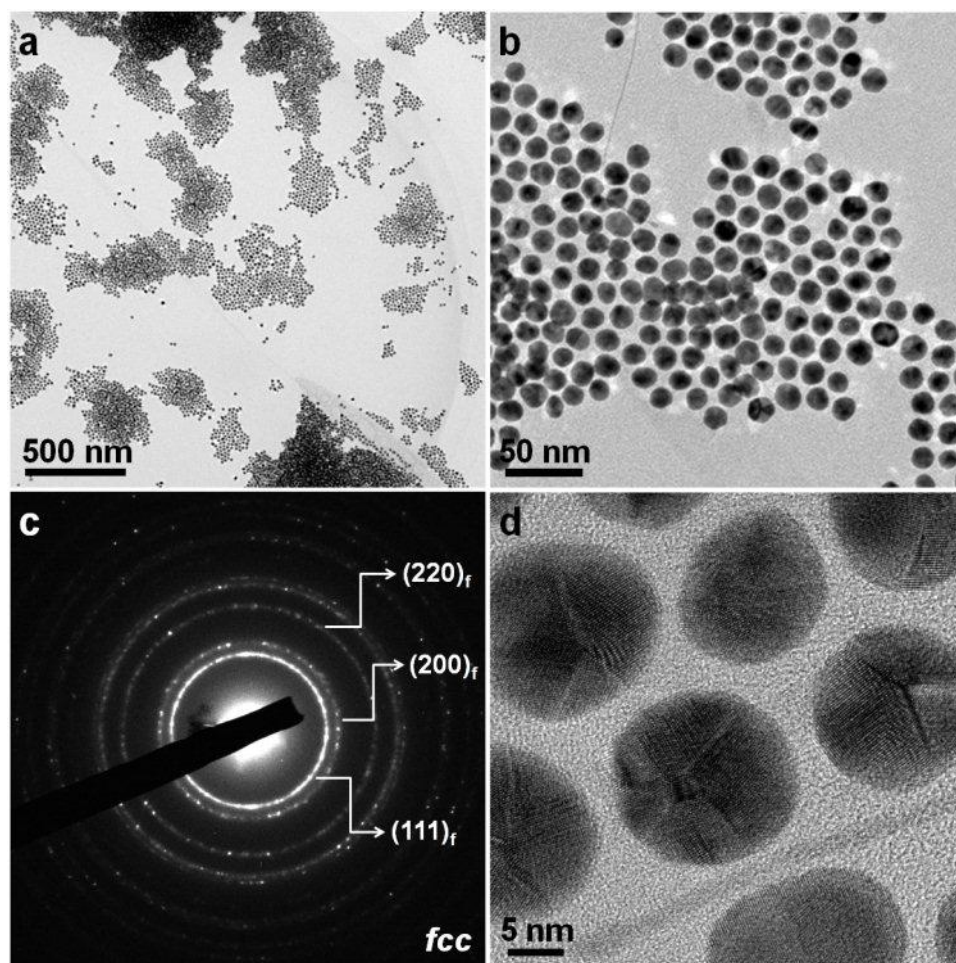


Figure 4-63. (a) Low-magnification and (b) high-magnification TEM images of as-prepared Au NPs together with tiny amount of Au NWs obtained in the absence of 1,2-dichloropropane. (c) SAED pattern and (d) HRTEM image of obtained Au NPs.

The obtained Au NRBs crystallize in an unprecedented 4H hexagonal phase (space group, $P6_3/mmc$), as proved by selected area electron diffraction (SAED) pattern collected along $[110]_{4H}$ zone axis (Figure 4-57c), which shows the diffraction spots assigned to the $(004)_{4H}$, $(1\bar{1}0)_{4H}$ and $(1\bar{1}2)_{4H}$ planes. The TEM image and the SAED pattern of a typical Au NRB suggest that it grows along the direction of $[001]_{4H}$ (Figure 4-57b,c). In order to further identify the 4H crystal structure of as-prepared Au NRBs, X-ray diffraction (XRD) pattern of obtained Au

nanostructures, deposited on a thin glass substrate, was also taken. The XRD pattern clearly demonstrates four strong peaks located at 36.2° , 37.4° , 40.9° , and 79.7° , which are attributed to the $(100)_{4H}$, $(101)_{4H}$, $(102)_{4H}$, and $(202)_{4H}$ planes of 4H Au, respectively (Figure 4-64). The simulated unit cell parameters of 4H Au NRBs are $a = 2.866 \text{ \AA}$ and $c = 9.662 \text{ \AA}$, respectively (Figure 4-57f). The other XRD peaks at 38.2° , 44.3° and 77.6° are derived from the coexisting by-products of *fcc* Au NPs (Figure 4-58). It should be pointed out that the peak located at 64.8° is assigned to both $(110)_{4H}$ and $(220)_f$ planes because their interplane lattice distances equal to each other. The aberration-corrected high-resolution TEM (HRTEM) images demonstrate that the 4H phase extends from the center to the edge regions of an Au NRB (Figure 4-57d,e), which has been further confirmed by the simulated HRTEM image (Figure 4-65). Based on the aforementioned observations, the crystallographic models (both top and side views) of a typical Au NRB are proposed, demonstrating a typical stacking sequence of “ABCB” along the close-packed direction of $[001]_{4H}$ (Figure 4-57g).

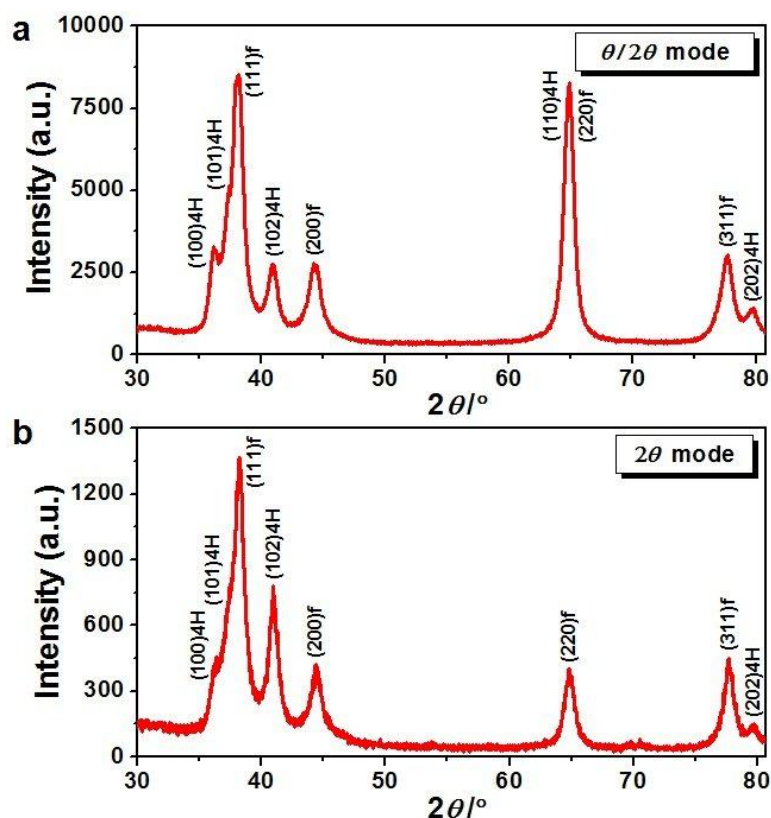


Figure 4-64. XRD pattern of 4H Au NRBs collected in the (a) $\theta/2\theta$ and (b) 2θ modes.

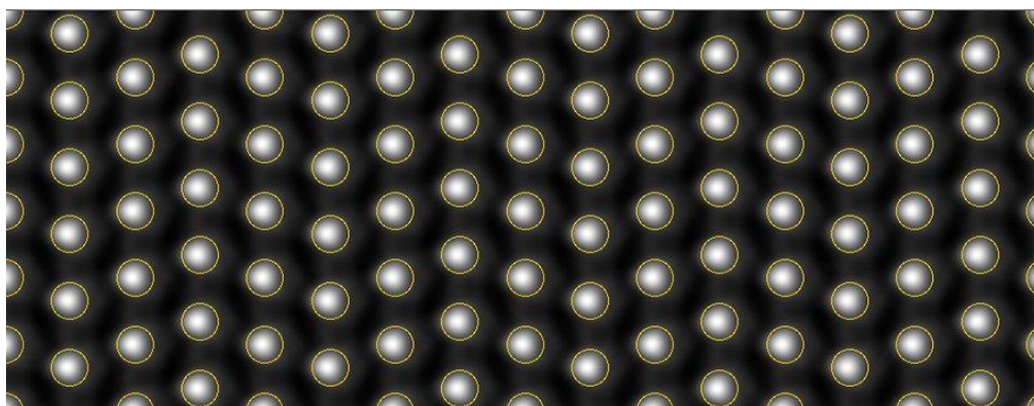


Figure 4-65. The simulated HRTEM image of 4H Au NRBs. The HRTEM image simulation was executed using the multislice method as implemented in the MacTempas software.

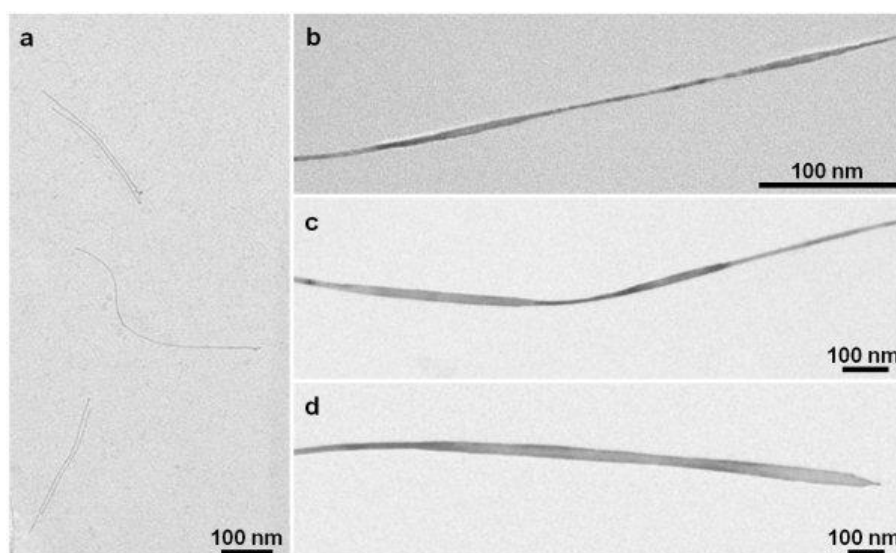


Figure 4-66. (a) At the reaction time of 4 h, ultrathin Au NWs (1.4–2.0 nm in diameter) were formed. The Au NWs gradually grew over time to form Au NRBs with the widths of (b) 2.8–5.2 nm at 8 h, (c) 8.0–20.0 nm at 12 h and (d) 15.0–61.0 nm at 16 h.

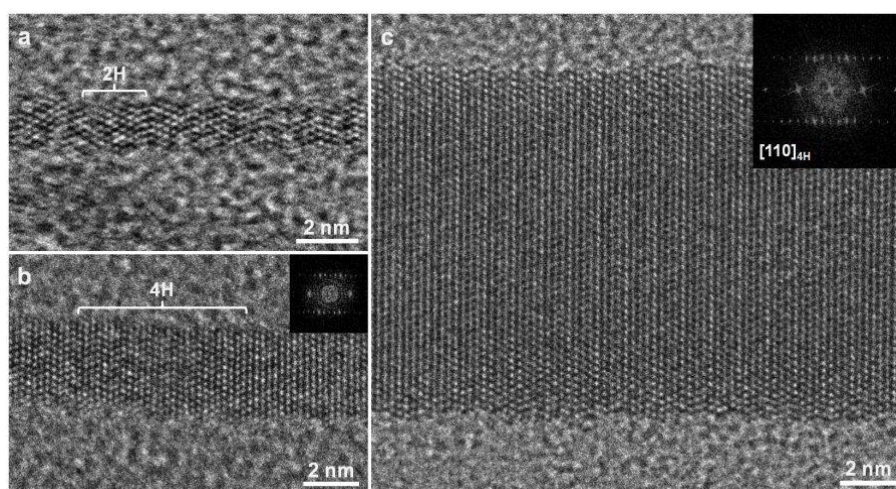


Figure 4-67. (a) At the reaction time of 4 h, the 2H phase and stacking faults were found in obtained ultrathin Au NWs. (b) The 4H phase appeared at the reaction time of 8 h. Inset: the FFT pattern of the selected 4H domain in (b). (c) Au NRBs with 4H phase were obtained at the reaction time of 12 h. Inset: FFT pattern of the HRTEM image in (c).

To reveal the formation mechanism of as-prepared 4H Au NRBs, the time-dependent experiments were executed at an interval of 4 h, and the intermediate products were characterized by TEM (Figures 4-66 and 4-67). At the reaction time of 4 h, ultrathin Au NW (1.4–2.0 nm in diameter) was formed (Figure 4-66a), which then evolved into the ribbon-like nanostructures along with the width increased to 2.8–5.2 nm at the reaction time of 8 h (Figure 4-66b). By further increasing the reaction time, the width of the Au NRBs increased to 8.0–20.0 nm (Figure 4-66c) and 15.0–61.0 nm (Figure 4-66d) at the reaction times of 12 h and 16 h, respectively. Previous investigations have revealed that the formation of ultrathin Au NWs can be driven by the soft-template effect of one-dimensional polymer structure, which was assembled from the (oleylamine)AuCl complexes with the aurophilic interaction^{161,163}. In the current work, the transition of ultrathin Au NWs to Au NRBs may also be driven by the aforementioned polymer template, since the (oleylamine)AuCl complexes were found to assemble into ribbon-like nanostructures in the final products (Figure 4-68). Besides the morphology transformation, that is, from the ultrathin NWs to NRBs, the evolution of the crystal phase is found, too. The ultrathin Au NWs, as revealed by the HRTEM image (Figure 4-67a), contain short-range hexagonal 2H domains along with randomly distributed stacking faults, which is consistent with the former study⁷¹. As the Au NWs grew and gradually adopted the ribbon-like morphology with a width of about 4 nm (Figure 4-66b), short range 4H domains started to appear (Figure 4-67b). When the width of Au NRBs increased to 8.0–20.0 nm (Figure 4-66c), Au NRBs with the 4H polytype were successfully synthesized (Figure 4-67c).

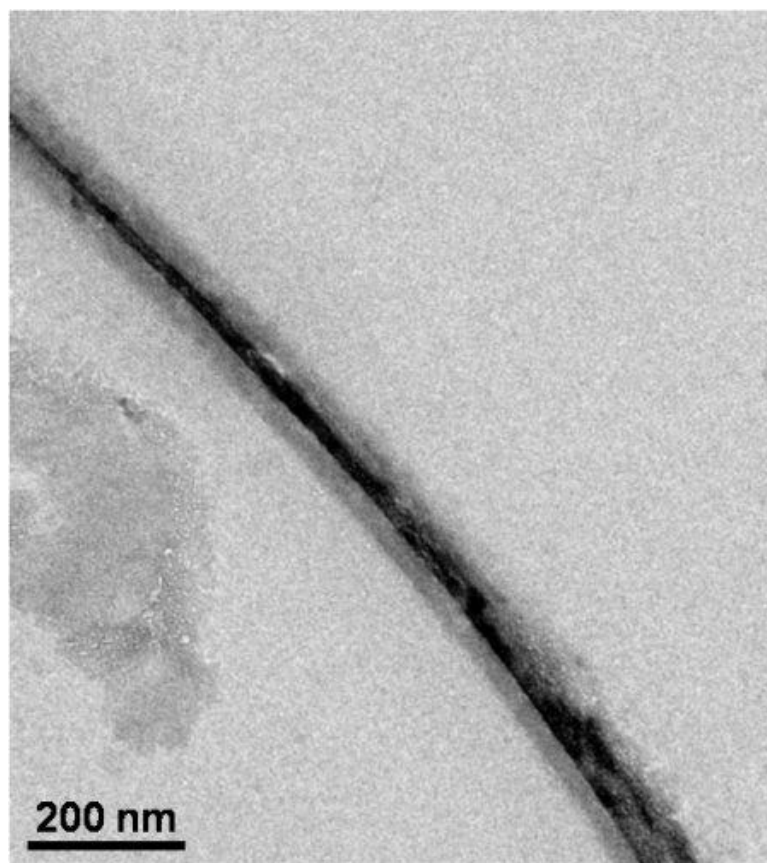


Figure 4-68. TEM image of a ribbon-like polymer structure, probably formed from the assembly of (oleylamine)AuCl complex molecules via aurophilic interaction.

The phase change from 2H (with a typical stacking sequence of AB) to 4H (with a typical stacking sequence of ABCB) polytypes has been found in alloy materials, e.g. TiCr_2 , by shear-induced formation of regular distributed stacking faults¹⁶⁷. Moreover, the 2H-to-4H phase transition caused by thermal annealing was also found in the transition of PbI_2 , whose 4H structure is much more stable than the 2H type at the transformation temperature¹⁶⁸. Similarly, the evolution from ultrathin 2H Au NWs to 4H Au NRBs may also be driven by their energy differences, as former theoretical calculations indicated that the 4H Au is much more stable than the 2H Au because of its much larger cohesive energy per atom⁶⁹.

4.3.3 Ligand Exchange Induced Phase Transformation of 4H Au Nanoribbons

The 4H crystal structure of as-prepared Au NRBs is metastable and can be changed to the common *fcc* phase after the ligand exchange of surface-capped oleylamine molecules with thiol molecules under ambient conditions (Figure 4-69). In a typical experiment, the ligand exchange was executed by vortexing the mixture of the 4H Au NRB and a freshly prepared 1-dodecanethiol solution for about 5 min. The STEM-EDS investigation of the thiol-treated Au NRBs indicates the presence of sulfur in the as-obtained final product, and hence identifies the occurrence of the oleylamine-to-thiol ligand exchange (Figure 4-70). Interestingly, the crystal structure of the thiol-treated Au NRBs is found to be *fcc* phase, which is confirmed by SAED pattern collected from the marked area in Figure 4-69a, displaying the typical square lattice pattern along zone axis of $[001]_f$ (Figure 4-69b). The $(001)_f$ oriented *fcc* structure is further proved by the SAED pattern collected along zone axis of $[013]_f$, realized by tilting the Au NRB around $[200]_f$ axis by about 18.2° , which is in good agreement with theoretical angle (18.4°) between $[001]_f$ and $[013]_f$ zone axes (Figure 4-69c).

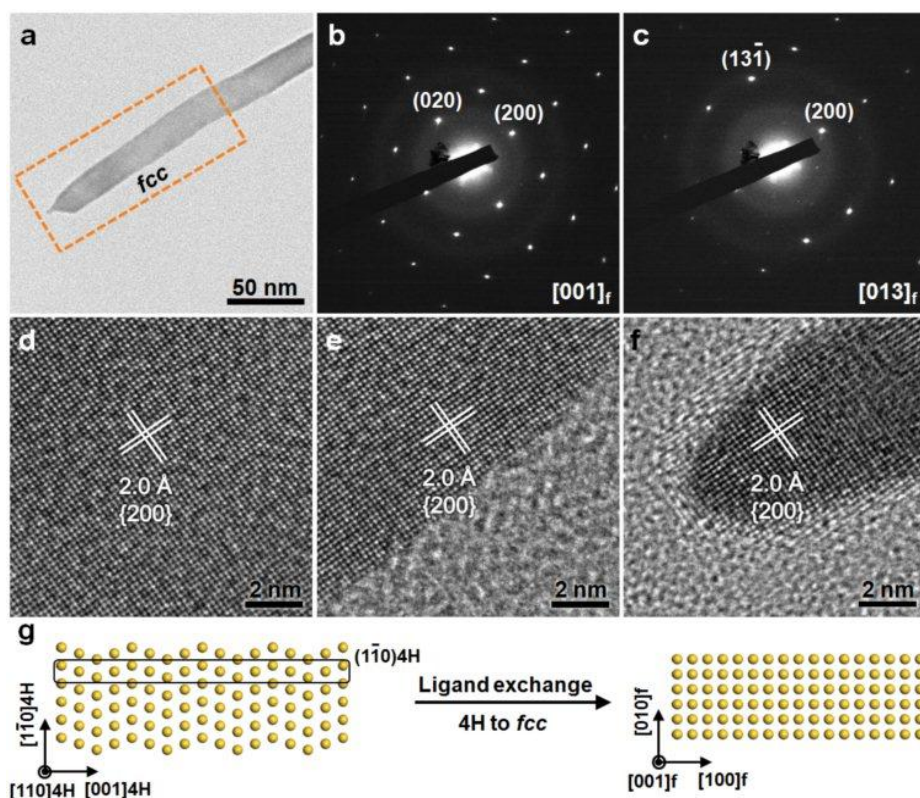


Figure 4-69. (a) TEM image of an Au NRB after ligand exchange. (b) SAED pattern of selected region by dashed rectangle in (a). (c) SAED pattern of $[013]_f$ zone axis was collected by tilting the Au NRB around $[200]_f$ zone axis for about 18.2° with respect to $[001]_f$ zone axis. (d-f) HRTEM images collected from the center (d), edge (e), and end (f) regions of the marked region in (a), respectively. (g) Schematic illustration for ligand-induced phase transition of an Au NRB.

The HRTEM images further indicate the $(001)_f$ oriented *fcc* phase with a lattice spacing of 2.0 \AA for the $\{200\}_f$ planes (Figure 4-69, d to f). Figure 4-69g and Figure 4-71 schematically show the thiol molecule-induced phase change of Au NRBs from the initial $(110)_{4H}$ -oriented 4H to the final $(001)_f$ -oriented *fcc* structures. Different to the normally observed *hcp*-to-*fcc* phase changes in metals and alloys which proceed by motion of the partial dislocations on close-packed planes and result in formation of twins/stacking faults¹⁰², the phase change of 4H Au NRBs

may arise from the flattening of $(1\bar{1}0)_{4H}$ planes (marked by rectangle in the left image of Figure 4-69g), which is quite similar to the phase transition of wurtzite-to-rock salt occurred in some semiconductor nanomaterials at high pressures, e.g. CdSe and GaN^{117,119}. Former studies indicated that thiol molecules and the other sulfur-containing compounds can cause surface reconstructions of metals, particularly, benefiting the formation of overlayers with large coordination numbers, e.g. *fcc*(100) surface that contains square hollow sites¹¹¹. Moreover, spherical Pt NPs were found to change to Pt nanocubes bound by $\{100\}_f$ facets in the presence of H_2S at 500 °C¹¹⁶. Thus the ligand-induced phase transition of Au NRBs under ambient conditions is most probably driven by the particularly unique and strong interaction between Au and S^{107,111}.

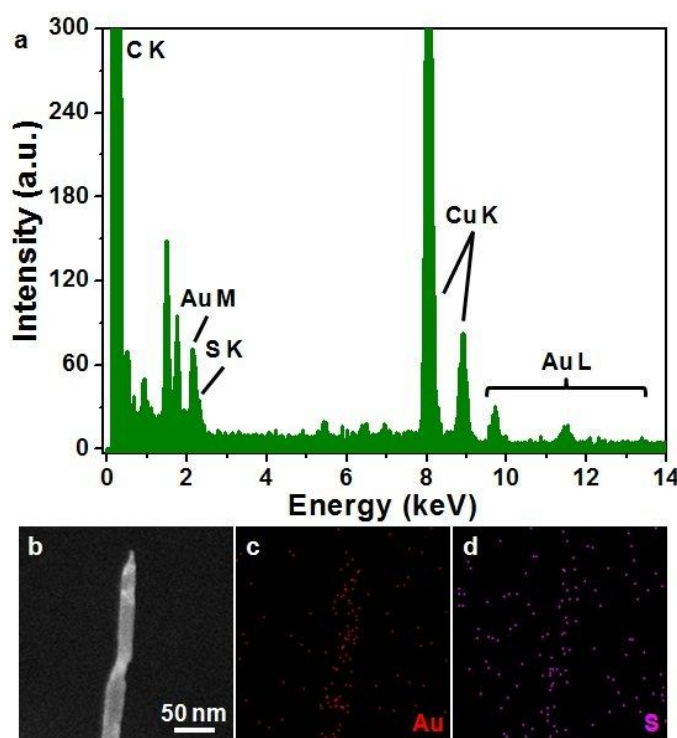


Figure 4-70. (a) STEM-EDS spectrum of Au NRBs after ligand exchange. (b) HAADF-STEM image, and (c,d) STEM-EDS element mappings of an Au NRB after ligand exchange.

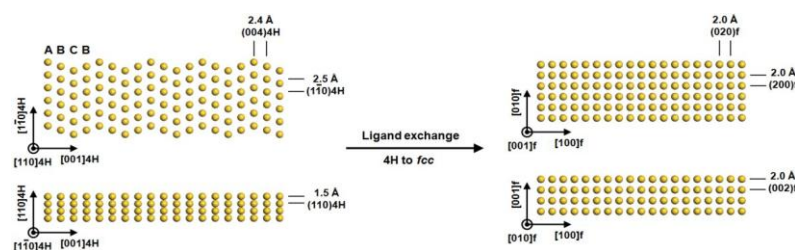


Figure 4-71. Schematic illustration for ligand exchange-induced phase change of Au NRB from 4H to *fcc* structures.

4.3.4 Monochromated Electron Energy Loss Spectroscopy Measurement of Individual 4H Au Nanoribbons

Individual 4H Au NRBs were characterized by the monochromated EELS in STEM (Figure 4-72a, see Methods for details). The monochromated EELS test was conducted by raster-scanning a focused-electron beam with a diameter of 1–2 nm in a rectangular area that included an individual 4H Au NRB. The interaction between electron beam and the conduction electrons in 4H Au NRBs generated the LSPR, which showed a fingerprint of the optoelectronic property of 4H Au NRBs. Figure 4-72b shows the monochromated EELS spectra of a single Au NRB taken at different positions (i.e. I, II, III and IV), several nanometers next to the Au NRB, as marked in Figure 4-72g. Two prominent LSPR peaks were observed in all the EELS spectra, that is, 0.82 eV and 1.75 eV at position “I”, 0.52 eV and 1.72 eV at position “II”, 0.36 eV and 1.93 eV at position “III”, 0.27 eV and 1.94 eV at position “IV”. The LSPR peaks of the Au NRB at different positions that appeared at low and high energy is induced by the eigen-modes longitudinally and transversely polarized with respect to the Au NRB geometry, respectively²⁰. Note that a remarkable red shift is observed for the dominant LSPR peaks from position “I” to position “IV”.

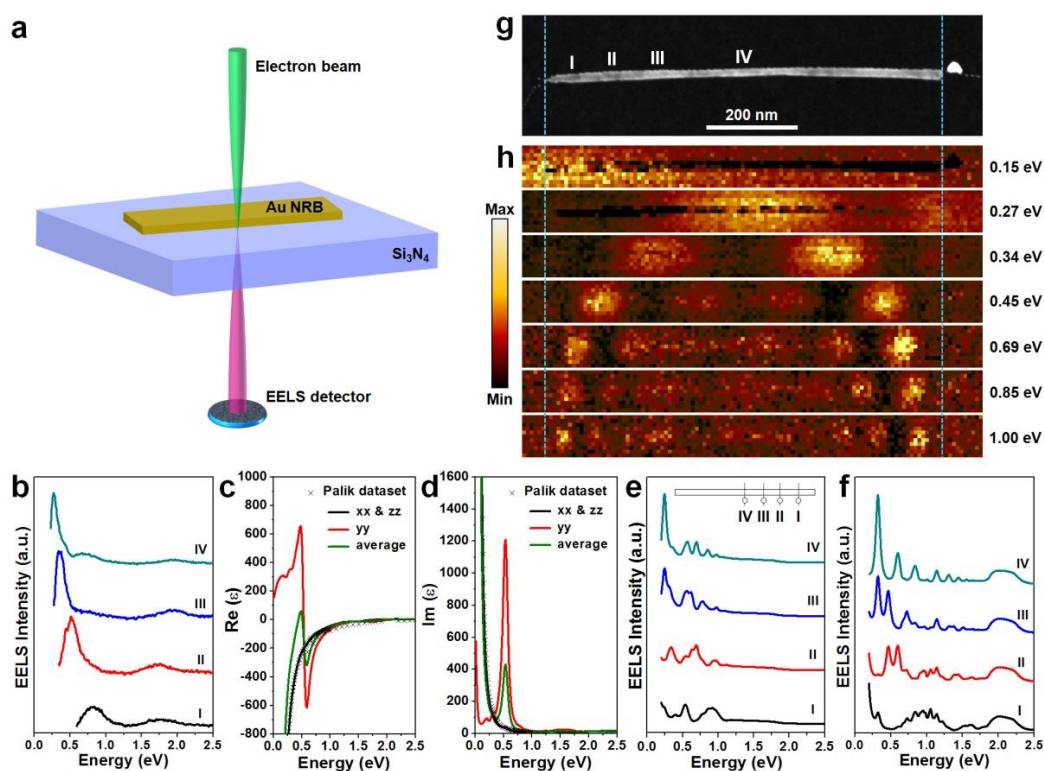


Figure 4-72. (a) Schematic illustration for monochromated EELS characterization of a single 4H Au NRB. The focused electron beam is located a few nanometers away from the Au NRB to excite and measure its LSPR. (b) Monochromated EELS spectra taken from individual Au NRBs excited at the different positions marked in (g). (c,d) DFT-calculated dielectric function of a 4H Au thin film with the limitation of 4 nm in the y direction. (e) Simulated EELS spectra of a 4H Au NRB based on the dielectric function in (c) and (d) using the FEM with an electron beam. Inset: the theoretical model of a single Au NRB, in which the excitation positions are indicated. (f) Simulated EELS spectra of an *fcc* Au NRB with dielectric function taken from Palik at the identical excitation positions as that in (e). (g,h) HAADF-STEM image of a single Au NRB and its EELS mappings at different energy losses.

As there is no optical data available for the 4H Au NRBs, density functional theory (DFT) calculations were applied to give the dielectric function of a 4H Au

thin film (Figure 4-72c,d). In the DFT model, the $[1\bar{1}0]_{4H}$, $[001]_{4H}$ and $[110]_{4H}$ is defined to be x -, y - and z -directions (Figure 4-57c,f). The 4H Au thin film is proposed to have 4 nm in its y -direction and stacks indefinitely in its x - and z -directions. The dielectric function of 4H Au thin films and that of fcc Au (obtained from literature, Palik⁸⁸) demonstrate quite different features in the perpendicular direction to the thin films (that is the yy direction). These differences arise from the surface atoms with the formation of plasma frequency at low frequency. The contribution of surface atoms to the dielectric function is much smaller with increasing the thickness of the thin film¹⁶⁹. A red shift for the primary LSPR peaks from excitation position “I” to position “IV” was also found in the finite-element-method (FEM) simulation of plasmon excitation with an electron beam (Figure 4-72e, see Methods for details), which is in good agreement with the aforementioned experimental results (Figure 4-72b). It should be pointed out that the Palik’s frequency-dependent dielectric function, derived from the fcc Au⁸⁸, was also applied in the FEM simulations to benchmark the differences of optical response between 4H Au and fcc Au (Figure 4-72f). In comparison with fcc Au (Figure 4-72f), the optical response of 4H Au thin film demonstrates a much smaller number of LSPR peaks in the range of 0–2.5 eV and red shift for all the LSPR peaks from excitation position “I” to position “IV” (Figure 4-72e). The experimental monochromated EELS mappings further indicate that low-order harmonic resonances were produced by the low-energy LSPR eigenmodes and the harmonic order increased with the LSPR energy (Figure 4-72h). The insight attained here is that the simulations with DFT-calculated optical constants of 4H Au followed much more closely to the trend of experiment results. The optical responses of 4H Au and fcc Au are quite different in terms of position and magnitude of the LSPR

peaks, it is thus reasonable to draw a conclusion that the structure modulation of Au nanomaterials can greatly change their optical properties.

4.3.5 Synthesis of Polytypic 4H/face-Centered Cubic Bimetallic Nanoribbons

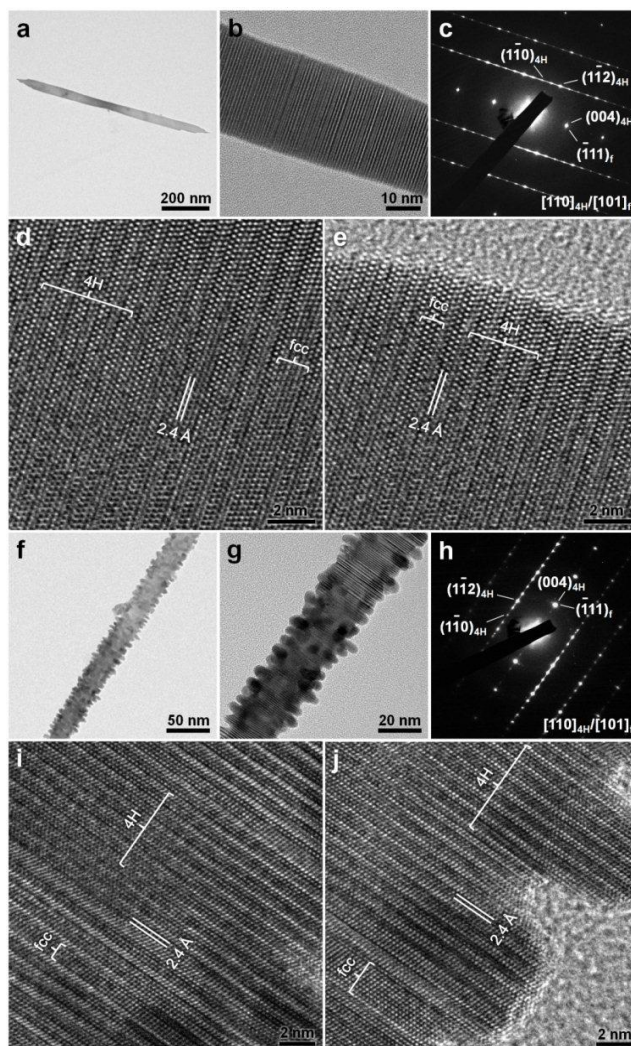


Figure 4-73. (a,b) TEM images of an Au@Ag NRB. (c) SAED pattern of an Au@Ag NRB collected along $[110]_{4H}/[101]_f$ zone axes. (d,e) HRTEM images of an Au@Ag NRB collected from the center (d) and edge (e) regions, respectively. (f,g) TEM images of an Au@Pd NRB. (h) SAED pattern of an Au@Pd NRB taken along $[110]_{4H}/[101]_f$ zone axes. (i,j) HRTEM images of an Au@Pd NRB taken from its center (i) and edge (j) areas, respectively.

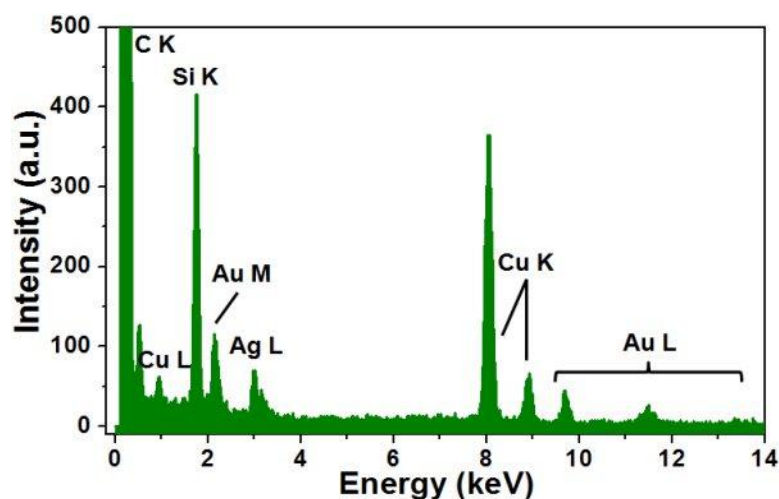


Figure 4-74. STEM-EDS spectrum of 4H/*fcc* Au@Ag NRBs with an average Au/Ag atomic ratio of 1.0/1.7.

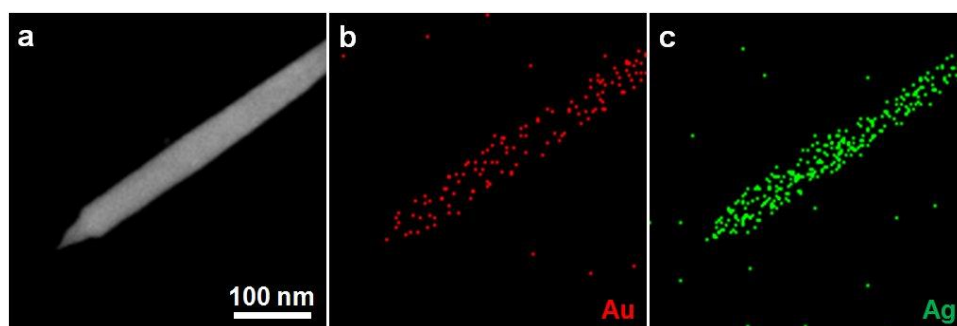


Figure 4-75. (a) HAADF-STEM image, and (b,c) STEM-EDS element mappings of a polytypic 4H/*fcc* Au@Ag NRB.

Importantly, the obtained 4H Au NRBs can be used as “seeds” for epitaxial growth of the other noble metals, resulting in formation of a new class of noble bimetallic Au@M (M = Ag, Pd, and Pt) core-shell nanostructures. For example, the Au@Ag NRBs were prepared via the reduction of AgNO₃ with oleylamine molecules in the presence of Au NRBs. The ribbon shape is well maintained after the epitaxial deposition of Ag on the surface of as-obtained 4H Au NRBs (Figure 4-73a,b). The chemical composition of as-prepared Au@Ag NRBs is characterized by STEM-EDS, showing an average Au/Ag atomic ratio of 1.0/1.7 (Figure 4-74).

The typical high-angle annular dark-field-STEM (HAADF-STEM) image of an Au@Ag NRB and STEM-EDS element mappings reveal the homogeneous distribution of Ag and Au (Figure 4-75), which is further identified by STEM-EDS line scanning profile (Figure 4-76). The typical SAED pattern of an Au@Ag NRB demonstrates the $[110]_{4H}$ zone pattern along with streaks along the direction of $[001]_{4H}$, indicating the coexisting of 4H and *fcc* phases together with lots of twins and stacking faults present along the $[001]_{4H}/[111]_f$ directions (Figure 4-73c). This suggests that the epitaxial deposition of Ag on the surface of Au NRBs led to the phase transformation of the initial 4H to 4H/*fcc* polytypic structures. Such a crystal structure was also identified by the selected-spot dark-field TEM study (Figure 4-77). The typical HRTEM images of an Au@Ag NRB further reveal the intergrowth of alternative 4H and *fcc* phases (Figure 4-73d,e), where the crystal lattice fringes coherently extend from the center to edge regions of the obtained 4H/*fcc* polytypic Au@Ag NRB, suggesting the epitaxial relationship between the inside Au core and outside Ag shell (Figure 4-73e).

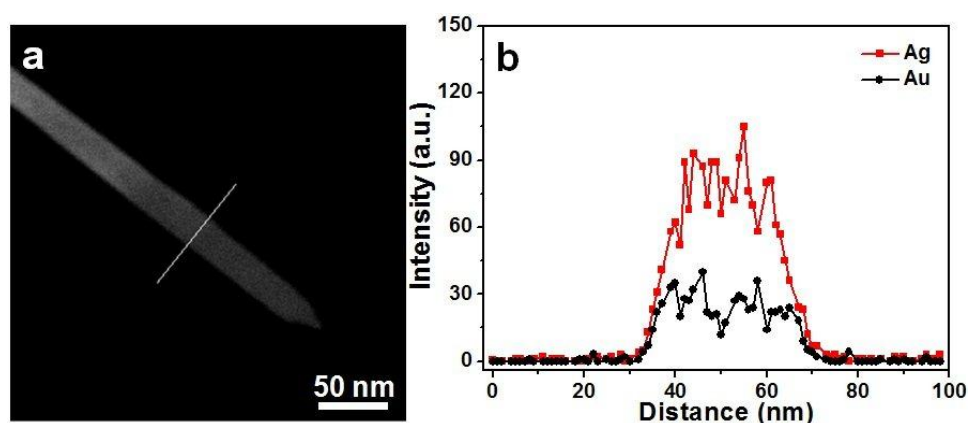


Figure 4-76. (a) HAADF-STEM image, and (b) STEM-EDS line scanning profile of a polytypic 4H/*fcc* Au@Ag NRB.

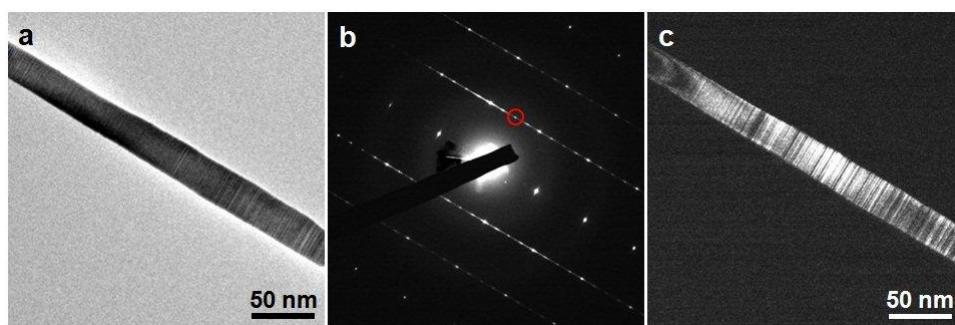


Figure 4-77. (a) TEM image and (b) SAED pattern of a polytypic 4H/*fcc* Au@Ag NRB. (c) The dark-field TEM image taken with $(1\bar{1}0)_{4H}$ diffraction spot indicated in (b).

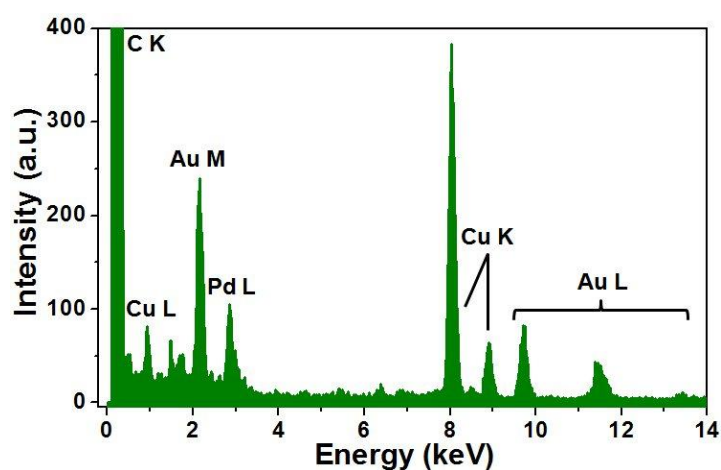


Figure 4-78. STEM-EDS spectrum of polytypic 4H/*fcc* Au@Pd NRBs with an average Au/Pd atomic ratio of 1.0/1.2.

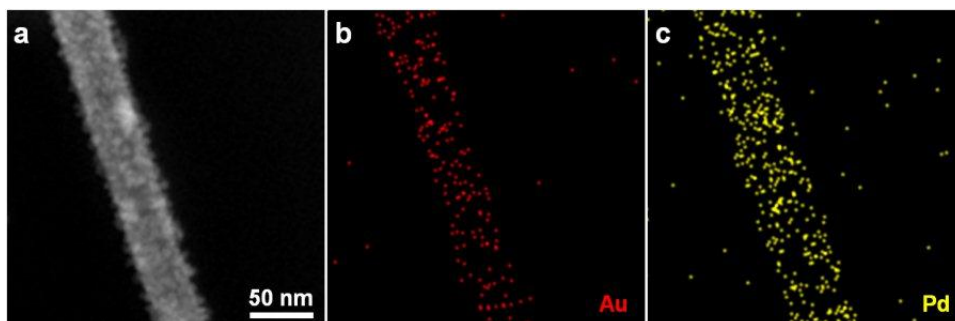


Figure 4-79. (a) HAADF-STEM image and (b,c) STEM-EDS element mappings of a polytypic 4H/*fcc* Au@Pd NRB.

In addition to Au@Ag NRBs, the Au@Pd NRBs were prepared via epitaxial growth of Pd on Au NRBs (Figure 4-73, f to j). The chemical composition of the Au@Pd NRBs is confirmed by STEM-EDS analysis showing an atomic ratio of 1.0/1.2 (Au/Pd) (Figure 4-78). The continuous distribution of Pd on Au is again indicated by STEM-EDS elemental map and line scanning of such Au@Pd NRBs (Figures 4-79 and 4-80). Similar to Au@Ag NRB, the Au@Pd NRB also shows the 4H/*fcc* polytypic structure with faulty stacking along the $[001]_{4H}/[111]_f$ direction (Figure 4-73, h to j). However, compared to the uniform Ag shell in Au@Ag NRBs (Figure 4-73a,b), the Pd shell in Au@Pd NRBs tends to grow in a Volmer-Weber (V-W) mode (i.e. island growth, Figure 4-73f,g) due to the much larger lattice mismatch between Au and Pd as compared to that between Au and Ag¹³². Importantly, it is worth mentioning that this is the first demonstration of 4H Pd structure (Fig. 4j), which has not been directly synthesized until now. Furthermore, the bimetallic 4H/*fcc* Au@Pt NRBs have also been synthesized via reduction of H_2PtCl_6 with $NaBH_4$ in the presence of 4H Au NRBs (Figures, 4-81 to 4-83).

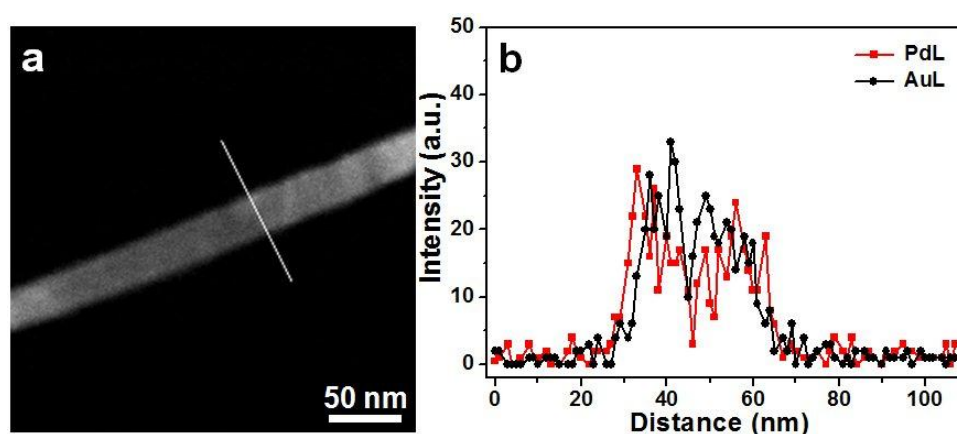


Figure 4-80. (a) HAADF-STEM image and (b) STEM-EDS line scanning profile of a polytypic 4H/*fcc* Au@Pd NRB.

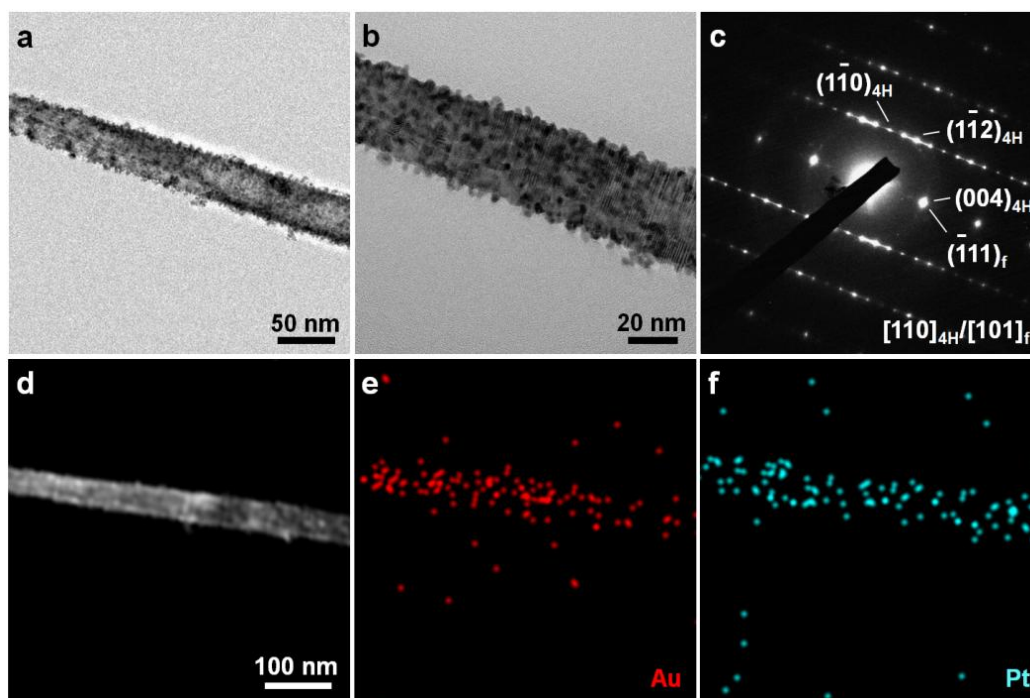


Figure 4-81. (a,b) TEM images and (c) SAED pattern of a polytypic 4H/fcc Au@Pt NRB. (d) HAADF-STEM image and (e,f) STEM-EDS element mappings of a polytypic 4H/fcc Au@Pt NRB.

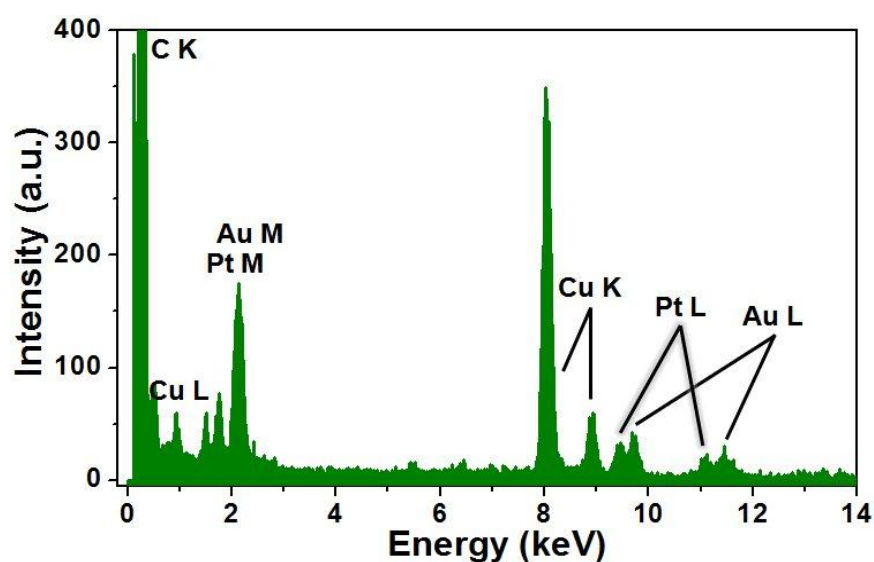


Figure 4-82. STEM-EDS spectrum of polytypic 4H/fcc Au@Pt NRBs with an average Au/Pt atomic ratio of 1.0/0.9.

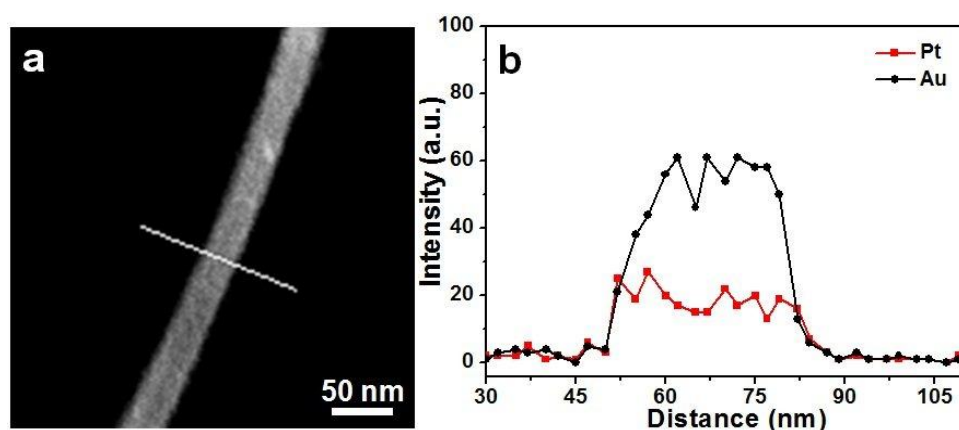


Figure 4-83. (a) HAADF-STEM image, and (b) STEM-EDS line scanning profile of a polytypic 4H/*fcc* Au@Pt NRB.

4.3.6 Short Summary

In this section, a new metastable phase of Au, that is, 4H structure, has been successfully synthesized in a high yield using a colloidal solution method. The ligand-induced phase change of the obtained Au NRBs from 4H to *fcc* structures has also been found under ambient conditions. The experimental and simulated EELS spectra of a single Au NRB suggest that the optical response between 4H and *fcc* Au is relatively different. Through the epitaxial growth of the other noble metals (e.g. Ag, Pt and Pd) on 4H Au NRBs, 4H metastable phases of these noble metals can be easily obtained. We believe that the systematic synthesis of novel noble metal nanomaterials here represents an important fundamental progress in material science and chemistry, and it will open up new opportunities for the controlled colloidal synthesis of advanced nanomaterials that have various promising catalytic and plasmonic applications.

CHAPTER 5 CONCLUSIONS AND RECOMMENDATIONS

5.1 Conclusions

In this thesis, surface modification methods, i.e. ligand exchange and metal coating, have been established to achieve the crystal phase controlled synthesis of new Au nanostructures and thin noble bimetallic nanosheets. Moreover, anisotropic Au nanomaterials with an unprecedented crystal structure have also been prepared by using a colloidal synthetic method under mild conditions. The following conclusions have been made from these works.

A ligand exchange method has been established to synthesize new Au nanomaterials with controlled structure, as well as shape. By simply shaking the mixture of hexagonal close-packed (*hcp*) Au square sheet (AuSS) and freshly prepared octadecanethiol (ODT) solutions, the oleylamine-to-ODT ligand exchange can be realized. The crystal structure of AuSSs has changed from *hcp* to face-centered cubic (*fcc*) phases after the ligand exchange. The as-prepared *fcc* AuSSs demonstrate a unique (100)_f orientation, which differs from the common (111)_f orientation observed from the existing noble metal nanoplates/nanosheets. Besides ODT, various kinds of other thiol molecules can also induce the formation of *fcc* AuSSs from *hcp* AuSSs. Furthermore, it is found that in this ligand exchange process, the crystallinity of the obtained *fcc* AuSSs can be finely modulated by changing the concentration of ODT, which suggests that the *hcp*-to-*fcc* phase transition of AuSSs is most probably a kinetically controlled process.

The metal coating approach has been used for the phase, shape and composition controlled synthesis of ultrathin noble bimetallic nanosheets with a thickness < 5 nm. The $(100)_f$ -oriented *fcc* Au@Ag square sheets can be synthesized via the epitaxial deposition of Ag on the *hcp* AuSSs in the absence of oleylamine. As the oleylamine may favor the formation of *hcp* structure, polytypic *hcp/fcc* Au@Ag square sheets with an orientation of $(110)_h/(101)_f$ is obtained through the epitaxial deposition of Ag on the *hcp* AuSSs in the presence of oleylamine. Remarkably, by changing the coating metal from Ag to Pt or Pd, $(101)_f$ oriented *fcc* Au@Pt or Au@Pd rhombic sheets with lots of defects (e.g. twins, stacking faults and dislocations) are obtained from *hcp* AuSSs, which is most likely caused by the much larger lattice mismatch between Au and Pt or Pd compared to that between Au and Ag. This work suggests that metal coating induced phase transformation can provide new opportunities for the controlled synthesis of unique noble bimetallic nanomaterials, which cannot be obtained by the conventional synthetic methods.

Ultrathin Au nanoribbons (NRBs) have been synthesized by heating a mixture consisting of HAuCl_4 and oleylamine in a binary solvent of hexane and 1,2-dichloropropane. The as-prepared Au NRBs, with a thickness of 2.0–6.0 nm, width of 15.0–61.0 nm and length of 0.5–6.0 μm , demonstrate an unprecedented 4H hexagonal structure. The formation of 4H Au NRBs is driven by the soft-template effect of one-dimensional polymer structure, which is assembled from (oleylamine)AuCl complex molecules by the aurophilic interaction. Interestingly, the 4H structure of Au NRBs can be transformed to *fcc* structure with the oleylamine-to-thiol ligand exchange under ambient conditions. Importantly, monochromated electron energy loss spectroscopy (EELS) study of individual 4H

Au NRBs reveals a strong plasmon absorption in a broad range of infrared region, i.e. from 1512 nm to 4592 nm. In addition, through the epitaxial growth of Ag, Pd and Pt on 4H Au NRBs, a novel class of polytypic 4H/*fcc* Au@M (M = Ag, Au and Pd) bimetallic NRBs can be readily prepared. It is worthy to mention that 4H hexagonal structures of both Pd and Pt have also been observed for the first time. This work opens up new opportunities for the phase, shape and composition controlled synthesis of advanced noble metal nanomaterials which may have promising applications in plasmonics and catalysis.

5.2 Recommendations for Future Work

The present work has achieved the phase, shape and composition controlled synthesis of noble metal nanomaterials via using the ligand exchange and metal coating methods, and the unprecedented formation of 4H hexagonal Au nanostructures via the colloidal synthetic method. These methods can be further improved and extended to the synthesis of other kinds of inorganic nanomaterials. Therefore, the following future works are recommended.

Firstly, although the (100)_F-oriented *fcc* AuSSs can be readily prepared from *hcp* AuSSs via the simple ligand exchange method, the underlying mechanism is still not fully understood. Due to the ultrafast (< 1 second) phase transformation of AuSSs from *hcp* to *fcc* upon ligand exchange, it is quite difficult to capture the transition states with common characterization instruments, making it hard to uncover the mechanism of this kind of phase transformation. Hence it is recommended that theoretical calculations, such as first-principle calculations and molecule dynamics, on the mechanism of the ligand exchange induced phase transformation of AuSSs are to be conducted in the future for a better understanding of this unusual *hcp*-to-*fcc* transformation pathway. Besides, as the

ligand exchange method is rapid and simple, it can be extended to the synthesis of other kinds of ultrathin inorganic nanomaterials via a phase transformation between different polytypes or crystal structures.

Secondly, the noble bimetallic nanosheets, i.e. Au@Pt and Au@Pd rhombic sheets, prepared from the metal coating approach are not pure. The as-prepared Au@Pt and Au@Pd rhombic sheets are coexisting with small amount of Au@Pt and Au@Pd square sheets, respectively. As the physical and chemical properties of noble metal nanomaterials are highly correlated with their morphology, it is recommended to further improve the current metal coating method in order to synthesize pure Au@Pt and Au@Pd rhombic sheets, or Au@Pt and Au@Pd square sheets in one batch, by finely tuning the experiment conditions (such as solvent polarity). In addition, noble bimetallic nanomaterials usually exhibit a higher chemical stability and superior catalytic properties in comparison with their mono-counterparts. It is hence recommended to explore the potential applications of the obtained noble bimetallic nanosheets in this work for plasmonics (for *fcc* and *hcp/fcc* Au@Ag square sheets) and electrocatalysis (for *fcc* Au@Pt and Au@Pd nanosheets).

Thirdly, although the 4H Au NRBs can be easily prepared via the current colloidal synthetic method with a relatively high yield, they are not pure, coexisting with some *fcc* Au NPs. As the purity of inorganic nanomaterial is of high importance for its potential applications, it is recommended to establish a simple colloidal synthetic method to give a much higher yield preparation of 4H Au NRBs, or establish a facile post-treatment method to separate the 4H Au NRBs from the by-products of *fcc* Au nanoparticles (NPs). Besides, because of the extremely strong infrared plasmonic absorption characteristic of 4H Au NRBs, it is

also recommended to investigate their potential applications in the infrared photothermal therapy.

Lastly, Au-semiconductor heteronanostructures have attracted increasing interests as Au nanostructure shows excellent chemical stability and strong localized surface plasmon resonance, which can significantly enhance the light absorption of semiconductor and even enable the electron transfer from Au to the semiconductor component through the so-called “hot-electron” effect, it is thus of great importance to fabricate novel Au-semiconductor heteronanostructures. As the Ag can be easily sulfurized under mild conditions, it is hence recommended to synthesize 4H/*fcc*-Au@Ag₂S NRB heterostructures from 4H/*fcc*-Au@Ag bimetallic NRBs. Meanwhile, cation exchange reaction has been demonstrated as a versatility way to modulate the chemical composition, structure and properties of ionic nanocrystals, especially transition metal chalcogenides. Therefore, it is also recommended to synthesize other kinds of NRB heterostructures, such as 4H/*fcc*-Au@MS (M = Cd, Pb and Zn) NRBs, from 4H/*fcc*-Au@Ag₂S NRB heterostructures via a simple process of cation exchange.

REFERENCES

- (1) Daniel, M.-C.; Astruc, D. (2004). Gold nanoparticles: assembly, supramolecular chemistry, quantum-size-related properties, and applications toward biology, catalysis, and nanotechnology. *Chem. Rev.*, 104 (1), 293-346.
- (2) Xia, Y.; Xiong, Y.; Lim, B.; Skrabalak, S. E. (2009). Shape-controlled synthesis of metal nanocrystals: simple chemistry meets complex physics? *Angew. Chem. Int. Ed.*, 48 (1), 60-103.
- (3) Lee, S.-W.; Lee, K.-S.; Ahn, J.; Lee, J.-J.; Kim, M.-G.; Shin, Y.-B. (2011). Highly sensitive biosensing using arrays of plasmonic Au nanodisks realized by nanoimprint lithography. *ACS Nano*, 5 (2), 897-904.
- (4) Lu, G.; Li, H.; Liusman, C.; Yin, Z.; Wu, S.; Zhang, H. (2011). Surface enhanced Raman scattering of Ag or Au nanoparticle-decorated reduced graphene oxide for detection of aromatic molecules. *Chem. Sci.*, 2 (9), 1817-1821.
- (5) Anker, J. N.; Hall, W. P.; Lyandres, O.; Shah, N. C.; Zhao, J.; Van Duyne, R. P. (2008). Biosensing with plasmonic nanosensors. *Nat. Mater.*, 7 (6), 442-453.
- (6) Huang, X.; Tang, S.; Mu, X.; Dai, Y.; Chen, G.; Zhou, Z.; Ruan, F.; Yang, Z.; Zheng, N. (2011). Freestanding palladium nanosheets with plasmonic and catalytic properties. *Nat. Nanotech.*, 6 (1), 28-32.
- (7) Jiang, R.; Li, B.; Fang, C.; Wang, J. (2014). Metal/semiconductor hybrid nanostructures for plasmon-enhanced applications. *Adv. Mater.*, 26 (31), 5274-5309.
- (8) Jiang, Y.; Horimoto, N. N.; Imura, K.; Okamoto, H.; Matsui, K.; Shigemoto, R. (2009). Bioimaging with two-photon-induced luminescence from triangular nanoplates and nanoparticle aggregates of gold. *Adv. Mater.*, 21 (22), 2309-2313.
- (9) Sun, S.; Murray, C. B.; Weller, D.; Folks, L.; Moser, A. (2000). Monodisperse FePt nanoparticles and ferromagnetic FePt nanocrystal superlattices. *Science*, 287 (5460), 1989-1992.

-
- (10) Niu, W.; Xu, G. (2011). Crystallographic control of noble metal nanocrystals. *Nano Today*, 6 (3), 265-285.
- (11) Sun, Y.; Xia, Y. (2002). Shape-controlled synthesis of gold and silver nanoparticles. *Science*, 298 (5601), 2176-2179.
- (12) Habas, S. E.; Lee, H.; Radmilovic, V.; Somorjai, G. A.; Yang, P. (2007). Shaping binary metal nanocrystals through epitaxial seeded growth. *Nat. Mater.*, 6 (9), 692-697.
- (13) Kim, J.; Lee, Y.; Sun, S. (2010). Structurally ordered FePt nanoparticles and their enhanced catalysis for oxygen reduction reaction. *J. Am. Chem. Soc.*, 132 (14), 4996-4997.
- (14) Chakraborty, I.; Shirodkar, N. S.; Gohil, S.; Waghmare, V. U.; Ayyub, P. (2014). A stable, quasi-2D modification of silver: optical, electronic, vibrational and mechanical properties, and first principles calculations. *J. Phys.: Condens. Matter*, 26 (2), 025402.
- (15) Guo, Q.; Zhao, Y.; Mao, W. L.; Wang, Z.; Xiong, Y.; Xia, Y. (2008). Cubic to tetragonal phase transformation in cold-compressed Pd nanocubes. *Nano Lett.*, 8 (3), 972-975.
- (16) Taneja, P.; Banerjee, R.; Ayyub, P.; Dey, G. K. (2001). Observation of a hexagonal (4H) phase in nanocrystalline silver. *Phys. Rev. B*, 64 (3), 033405.
- (17) Liu, X.; Luo, J.; Zhu, J. (2006). Size effect on the crystal structure of silver nanowires. *Nano Lett.*, 6 (3), 408-412.
- (18) Kusada, K.; Kobayashi, H.; Yamamoto, T.; Matsumura, S.; Sumi, N.; Sato, K.; Nagaoka, K.; Kubota, Y.; Kitagawa, H. (2013). Discovery of face-centered-cubic ruthenium nanoparticles: facile size-controlled synthesis using the chemical reduction method. *J. Am. Chem. Soc.*, 135 (15), 5493-5496.
- (19) Huang, X.; Li, S.; Huang, Y.; Wu, S.; Zhou, X.; Gan, C. L.; Boey, F.; Mirkin, C. A.; Zhang, H. (2011). Synthesis of hexagonal close-packed gold nanostructures. *Nat. Commun.*, 2, 292.
- (20) Bosman, M.; Zhang, L.; Duan, H.; Tan, S. F.; Nijhuis, C. A.; Qiu, C. W.; Yang, J. K. W. (2014). Encapsulated annealing: enhancing the plasmon quality factor in lithographically-defined nanostructures. *Sci. Rep.*, 4, 5537.

-
- (21) Bosman, M.; Keast, V. J. (2008). Optimizing EELS acquisition. *Ultramicroscopy*, 108 (9), 837-846.
- (22) Bosman, M.; J. Keast, V.; Watanabe, M.; I. Maarooft, A.; B. Cortie, M. (2007). Mapping surface plasmons at the nanometre scale with an electron beam. *Nanotechnology*, 18 (16), 165505.
- (23) El-Sayed, M. A. (2004). Small is different: shape-, size-, and composition-dependent properties of some colloidal semiconductor nanocrystals. *Acc. Chem. Res.*, 37 (5), 326-333.
- (24) Roduner, E. (2006). Size matters: why nanomaterials are different. *Chem. Soc. Rev.*, 35 (7), 583-592.
- (25) Zijlstra, P.; Chon, J. W. M.; Gu, M. (2009). Five-dimensional optical recording mediated by surface plasmons in gold nanorods. *Nature*, 459 (7245), 410-413.
- (26) Fan, Z.; Huang, X.; Tan, C.; Zhang, H. (2015). Thin metal nanostructures: synthesis, properties and applications. *Chem. Sci.*, 6 (1), 95-111.
- (27) Willets, K. A.; Van Duyne, R. P. (2007). Localized surface plasmon resonance spectroscopy and sensing. *Annu. Rev. Phys. Chem.*, 58 (1), 267-297.
- (28) Hutter, E.; Fendler, J. H. (2004). Exploitation of localized surface plasmon resonance. *Adv. Mater.*, 16 (19), 1685-1706.
- (29) Yao, K.; Salvador, M.; Chueh, C.-C.; Xin, X.-K.; Xu, Y.-X.; deQuilettes, D. W.; Hu, T.; Chen, Y.; Ginger, D. S.; Jen, A. K. Y. (2014). A general route to enhance polymer solar cell performance using plasmonic nanoprisms. *Adv. Energy Mater.*, 4 (9), 1400206.
- (30) Hsiao, V. K. S.; Zheng, Y. B.; Juluri, B. K.; Huang, T. J. (2008). Light-driven plasmonic switches based on Au nanodisk arrays and photoresponsive liquid crystals. *Adv. Mater.*, 20 (18), 3528-3532.
- (31) Huang, X.; Tang, S.; Yang, J.; Tan, Y.; Zheng, N. (2011). Etching growth under surface confinement: An effective strategy to prepare mesocrystalline Pd nanocorolla. *J. Am. Chem. Soc.*, 133 (40), 15946-15949.

- (32) Viarbitskaya, S.; Teulle, A.; Marty, R.; Sharma, J.; Girard, C.; Arbouet, A.; Dujardin, E. (2013). Tailoring and imaging the plasmonic local density of states in crystalline nanoprisms. *Nat. Mater.*, 12 (5), 426-432.
- (33) Huang, X.; Tang, S.; Liu, B.; Ren, B.; Zheng, N. (2011). Enhancing the photothermal stability of plasmonic metal nanoplates by a core-shell architecture. *Adv. Mater.*, 23 (30), 3420-3425.
- (34) Xiong, Y.; McLellan, J. M.; Chen, J.; Yin, Y.; Li, Z.-Y.; Xia, Y. (2005). Kinetically controlled synthesis of triangular and hexagonal nanoplates of palladium and their properties. *J. Am. Chem. Soc.*, 127 (48), 17118-17127.
- (35) Chen, J.; Wiley, B.; Li, Z. Y.; Campbell, D.; Saeki, F.; Cang, H.; Au, L.; Lee, J.; Li, X.; Xia, Y. (2005). Gold nanocages: Engineering their structure for biomedical applications. *Adv. Mater.*, 17 (18), 2255-2261.
- (36) Yavuz, M. S.; Cheng, Y.; Chen, J.; Cobley, C. M.; Zhang, Q.; Rycenga, M.; Xie, J.; Kim, C.; Song, K. H.; Schwartz, A. G.; Wang, L. V.; Xia, Y. (2009). Gold nanocages covered by smart polymers for controlled release with near-infrared light. *Nat. Mater.*, 8 (12), 935-939.
- (37) Pelaz, B.; Grazu, V.; Ibarra, A.; Magen, C.; del Pino, P.; de la Fuente, J. M. (2012). Tailoring the synthesis and heating ability of gold nanoprisms for bioapplications. *Langmuir*, 28 (24), 8965-8970.
- (38) Xue, C.; Li, Z.; Mirkin, C. A. (2005). Large-scale assembly of single-crystal silver nanoprism monolayers. *Small*, 1 (5), 513-516.
- (39) Beeram, S. R.; Zamborini, F. P. (2010). Purification of gold nanoplates grown directly on surfaces for enhanced localized surface plasmon resonance biosensing. *ACS Nano*, 4 (7), 3633-3646.
- (40) Charles, D. E.; Aherne, D.; Gara, M.; Ledwith, D. M.; Gun'ko, Y. K.; Kelly, J. M.; Blau, W. J.; Brennan-Fournet, M. E. (2009). Versatile solution phase triangular silver nanoplates for highly sensitive plasmon resonance sensing. *ACS Nano*, 4 (1), 55-64.
- (41) Huang, X.; Li, Y.; Chen, Y.; Zhou, H.; Duan, X.; Huang, Y. (2013). Plasmonic and catalytic AuPd nanowheels for the efficient conversion of light into chemical energy. *Angew. Chem. Int. Ed.*, 125 (23), 6179-6183.

- (42) Li, H.; Chen, G.; Yang, H.; Wang, X.; Liang, J.; Liu, P.; Chen, M.; Zheng, N. (2013). Shape-controlled synthesis of surface-clean ultrathin palladium nanosheets by simply mixing a dinuclear pdi carbonyl chloride complex with H_2O . *Angew. Chem. Int. Ed.*, 125 (32), 8526-8530.
- (43) Andoy, N. M.; Zhou, X.; Choudhary, E.; Shen, H.; Liu, G.; Chen, P. (2013). Single-molecule catalysis mapping quantifies site-specific activity and uncovers radial activity gradient on single 2d nanocrystals. *J. Am. Chem. Soc.*, 135 (5), 1845-1852.
- (44) Duan, H.; Yan, N.; Yu, R.; Chang, C.-R.; Zhou, G.; Hu, H.-S.; Rong, H.; Niu, Z.; Mao, J.; Asakura, H.; Tanaka, T.; Dyson, P. J.; Li, J.; Li, Y. (2014). Ultrathin rhodium nanosheets. *Nat. Commun.*, 5, 3093.
- (45) Zhou, X.; Andoy, N. M.; Liu, G.; Choudhary, E.; Han, K.-S.; Shen, H.; Chen, P. (2012). Quantitative super-resolution imaging uncovers reactivity patterns on single nanocatalysts. *Nat. Nanotech.*, 7 (4), 237-241.
- (46) Lim, B.; Jiang, M.; Camargo, P. H.; Cho, E. C.; Tao, J.; Lu, X.; Zhu, Y.; Xia, Y. (2009). Pd-Pt bimetallic nanodendrites with high activity for oxygen reduction. *Science*, 324 (5932), 1302-1305.
- (47) Zhang, J.; Sasaki, K.; Sutter, E.; Adzic, R. R. (2007). Stabilization of platinum oxygen-reduction electrocatalysts using gold clusters. *Science*, 315 (5809), 220-222.
- (48) Haruta, M. (1997). Size- and support-dependency in the catalysis of gold. *Catal. Today*, 36 (1), 153-166.
- (49) Gao, D.; Zhou, H.; Wang, J.; Miao, S.; Yang, F.; Wang, G.; Wang, J.; Bao, X. (2015). Size-dependent electrocatalytic reduction of CO_2 over Pd nanoparticles. *J. Am. Chem. Soc.*, 137 (13), 4288-4291.
- (50) Zaera, F. (2013). Shape-controlled nanostructures in heterogeneous catalysis. *ChemSusChem*, 6 (10), 1797-1820.
- (51) Haruta, M.; Yamada, N.; Kobayashi, T.; Iijima, S. (1989). Gold catalysts prepared by coprecipitation for low-temperature oxidation of hydrogen and of carbon monoxide. *J. Catal.*, 115 (2), 301-309.
- (52) Haruta, M. (2005). Catalysis: gold rush. *Nature*, 437 (7062), 1098-1099.

- (53) Tian, N.; Zhou, Z.-Y.; Sun, S.-G.; Ding, Y.; Wang, Z. L. (2007). Synthesis of tetrahedral platinum nanocrystals with high-index facets and high electro-oxidation activity. *Science*, 316 (5825), 732-735.
- (54) Narayanan, R.; El-Sayed, M. A. (2004). Shape-dependent catalytic activity of platinum nanoparticles in colloidal solution. *Nano Lett.*, 4 (7), 1343-1348.
- (55) Lee, I.; Delbecq, F.; Morales, R.; Albiter, M. A.; Zaera, F. (2009). Tuning selectivity in catalysis by controlling particle shape. *Nat. Mater.*, 8 (2), 132-138.
- (56) Lu, C.-L.; Prasad, K. S.; Wu, H.-L.; Ho, J.-A. A.; Huang, M. H. (2010). Au nanocube-directed fabrication of Au-Pd core-shell nanocrystals with tetrahedral, concave octahedral, and octahedral structures and their electrocatalytic activity. *J. Am. Chem. Soc.*, 132 (41), 14546-14553.
- (57) Wang, F.; Li, C.; Sun, L. D.; Wu, H.; Ming, T.; Wang, J.; Yu, J. C.; Yan, C. H. (2011). Heteroepitaxial growth of high-index-faceted palladium nanoshells and their catalytic performance. *J. Am. Chem. Soc.*, 133 (4), 1106-1111.
- (58) Quan, Z.; Wang, Y.; Fang, J. (2013). High-index faceted noble metal nanocrystals. *Acc. Chem. Res.*, 46 (2), 191-202.
- (59) Wang, D.; Yu, Y.; Xin, H. L.; Hovden, R.; Ercius, P.; Mundy, J. A.; Chen, H.; Richard, J. H.; Muller, D. A.; DiSalvo, F. J.; Abruña, H. D. (2012). Tuning oxygen reduction reaction activity via controllable dealloying: a model study of ordered Cu₃Pt/C intermetallic nanocatalysts. *Nano Lett.*, 12 (10), 5230-5238.
- (60) Wang, D.; Xin, H. L.; Hovden, R.; Wang, H.; Yu, Y.; Muller, D. A.; DiSalvo, F. J.; Abruña, H. D. (2013). Structurally ordered intermetallic platinum-cobalt core-shell nanoparticles with enhanced activity and stability as oxygen reduction electrocatalysts. *Nat. Mater.*, 12 (1), 81-87.
- (61) Dai, Z. R.; Sun, S.; Wang, Z. L. (2001). Phase transformation, coalescence, and twinning of monodisperse FePt nanocrystals. *Nano Lett.*, 1 (8), 443-447.
- (62) Kim, J.; Rong, C.; Lee, Y.; Liu, J. P.; Sun, S. (2008). From core/shell structured FePt/Fe₃O₄/MgO to ferromagnetic FePt nanoparticles. *Chem. Mater.*, 20 (23), 7242-7245.

- (63) Zhang, S.; Guo, S.; Zhu, H.; Su, D.; Sun, S. (2012). Structure-induced enhancement in electrooxidation of trimetallic FePtAu nanoparticles. *J. Am. Chem. Soc.*, 134 (11), 5060-5063.
- (64) Mukherjee, P.; Manchanda, P.; Kumar, P.; Zhou, L.; Kramer, M. J.; Kashyap, A.; Skomski, R.; Sellmyer, D.; Shield, J. E. (2014). Size-induced chemical and magnetic ordering in individual Fe–Au nanoparticles. *ACS Nano*, 8 (8), 8113-8120.
- (65) Sun, Y.; Yang, W.; Ren, Y.; Wang, L.; Lei, C. (2011). Multiple-step phase transformation in silver nanoplates under high pressure. *Small*, 7 (5), 606-611.
- (66) Koski, K. J.; Kamp, N. M.; Smith, R. K.; Kunz, M.; Knight, J. K.; Alivisatos, A. P. (2008). Structural distortions in 5-10 nm silver nanoparticles under high pressure. *Phys. Rev. B*, 78 (16), 165410.
- (67) Luo, J.; Zhang, L.; Zhang, Y.; Zhu, J. (2002). Controlled growth of one-dimensional metal–semiconductor and metal–carbon nanotube heterojunctions. *Adv. Mater.*, 14 (19), 1413-1414.
- (68) Ye, Z.; Guang Tao, F.; Ping, C.; Bing, W.; Biao, W.; Li De, Z. (2008). The fabrication and thermal expansion properties of 4H-Ag nanowire arrays in porous anodic alumina templates. *Nanotechnology*, 19 (28), 285711.
- (69) Chakraborty, I.; Carvalho, D.; Shirodkar, N. S.; Lahiri, S.; Bhattacharyya, S.; Banerjee, R.; Waghmare, U.; Ayyub, P. (2011). Novel hexagonal polytypes of silver: growth, characterization and first-principles calculations. *J. Phys.: Condens. Matter*, 23 (32), 325401.
- (70) Chakraborty, I.; Shirodkar, N. S.; Gohil, S.; Waghmare, V. U.; Ayyub, P. (2014). The nature of the structural phase transition from the hexagonal (4H) phase to the cubic (3C) phase of silver. *J. Phys.: Condens. Matter*, 26 (11), 115405.
- (71) Huang, X.; Li, S.; Wu, S.; Huang, Y.; Boey, F.; Gan, C. L.; Zhang, H. (2012). Graphene oxide-templated synthesis of ultrathin or tadpole-shaped Au nanowires with alternating *hcp* and *fcc* domains. *Adv. Mater.*, 24 (7), 979-983.
- (72) Singh, A.; Sai, T. P.; Ghosh, A. (2008). Electrochemical fabrication of ultralow noise metallic nanowires with *hcp* crystalline lattice. *Appl. Phys. Lett.*, 93 (10), 102107.

- (73) Zhang, S.; Zhang, X.; Jiang, G.; Zhu, H.; Guo, S.; Su, D.; Lu, G.; Sun, S. (2014). Tuning nanoparticle structure and surface strain for catalysis optimization. *J. Am. Chem. Soc.*, 136 (21), 7734-7739.
- (74) Li, Q.; Wu, L.; Wu, G.; Su, D.; Lv, H.; Zhang, S.; Zhu, W.; Casimir, A.; Zhu, H.; Mendoza-Garcia, A.; Sun, S. (2015). New approach to fully ordered fct-FePt nanoparticles for much enhanced electrocatalysis in acid. *Nano Lett.*, 15 (4), 2468-2473.
- (75) Xiaohua, L.; Jing, Z.; Chuanhong, J.; Lian-Mao, P.; Daiming, T.; Huiming, C. (2008). In situ electrical measurements of polytypic silver nanowires. *Nanotechnology*, 19 (8), 085711.
- (76) Kim, J.; Rong, C.; Liu, J. P.; Sun, S. (2009). Dispersible ferromagnetic FePt nanoparticles. *Adv. Mater.*, 21 (8), 906-909.
- (77) Liu, F.; Zhu, J.; Yang, W.; Dong, Y.; Hou, Y.; Zhang, C.; Yin, H.; Sun, S. (2014). Building nanocomposite magnets by coating a hard magnetic core with a soft magnetic shell. *Angew. Chem. Int. Ed.*, 53 (8), 2176-2180.
- (78) Scholl, J. A.; Koh, A. L.; Dionne, J. A. (2012). Quantum plasmon resonances of individual metallic nanoparticles. *Nature*, 483 (7390), 421-427.
- (79) García de Abajo, F. J. (2010). Optical excitations in electron microscopy. *Rev. Mod. Phys.*, 82 (1), 209-275.
- (80) Myroshnychenko, V.; Rodriguez-Fernandez, J.; Pastoriza-Santos, I.; Funston, A. M.; Novo, C.; Mulvaney, P.; Liz-Marzan, L. M.; Garcia de Abajo, F. J. (2008). Modelling the optical response of gold nanoparticles. *Chem. Soc. Rev.*, 37 (9), 1792-1805.
- (81) Liang, H.; Rossouw, D.; Zhao, H.; Cushing, S. K.; Shi, H.; Korinek, A.; Xu, H.; Rosei, F.; Wang, W.; Wu, N.; Botton, G. A.; Ma, D. (2013). Asymmetric silver “nanocarrot” structures: Solution synthesis and their asymmetric plasmonic resonances. *J. Am. Chem. Soc.*, 135 (26), 9616-9619.
- (82) N’Gom, M.; Ringnalda, J.; Mansfield, J. F.; Agarwal, A.; Kotov, N.; Zaluzec, N. J.; Norris, T. B. (2008). Single particle plasmon spectroscopy of silver nanowires and gold nanorods. *Nano Lett.*, 8 (10), 3200-3204.

- (83) Nelayah, J.; Kociak, M.; Stephan, O.; Garcia de Abajo, F. J.; Tence, M.; Henrard, L.; Taverna, D.; Pastoriza-Santos, I.; Liz-Marzan, L. M.; Colliex, C. (2007). Mapping surface plasmons on a single metallic nanoparticle. *Nat. Phys.*, 3 (5), 348-353.
- (84) Zhou, X.; Huang, X.; Qi, X.; Wu, S.; Xue, C.; Boey, F. Y. C.; Yan, Q.; Chen, P.; Zhang, H. (2009). In situ synthesis of metal nanoparticles on single-layer graphene oxide and reduced graphene oxide surfaces. *J. Phy. Chem. C*, 113 (25), 10842-10846.
- (85) Blaha, P.; Schwarz, K.; Madsen, G. K.; Kvasnicka, H. D.; Luitz, J.: WIEN2k, an augmented plane wave plus local orbitals program for calculating crystal properties. Vienna University of Technology, 2009; pp 258.
- (86) Abt, R.; Ambrosch-Draxl, C.; Knoll, P. (1994). Optical response of high temperature superconductors by full potential LAPW band structure calculations. *Physica B*, 194–196, 1451-1452.
- (87) Ambrosch-Draxl, C.; Sofo, J. O. (2006). Linear optical properties of solids within the full-potential linearized augmented planewave method. *Comp. Phys. Commun.*, 175 (1), 1-14.
- (88) Palik, E. D.: Handbook of optical constants of solids. Palik, E. D., Ed.; Academic Press: San Diego, California, 1997; pp 999.
- (89) Jackson, J. D.: Classical electrodynamics. J. Wiley & Sons: New York, 1999; pp 832.
- (90) Hochbaum, A. I.; Yang, P. (2009). Semiconductor nanowires for energy conversion. *Chem. Rev.*, 110 (1), 527-546.
- (91) Tolbert, S. H.; Alivisatos, A. P. (1994). Size dependence of a first order solid-solid phase transition: the wurtzite to rock salt transformation in CdSe nanocrystals. *Science*, 265 (5170), 373-376.
- (92) Han, M.; Liu, Q.; He, J.; Song, Y.; Xu, Z.; Zhu, J. M. (2007). Controllable synthesis and magnetic properties of cubic and hexagonal phase nickel nanocrystals. *Adv. Mater.*, 19 (8), 1096-1100.
- (93) Thelander, C.; Caroff, P.; Plissard, S.; Dey, A. W.; Dick, K. A. (2011). Effects of crystal phase mixing on the electrical properties of InAs nanowires. *Nano Lett.*, 11 (6), 2424-2429.

- (94) Alloyeau, D.; Ricolleau, C.; Mottet, C.; Oikawa, T.; Langlois, C.; Le Bouar, Y.; Braïdy, N.; Loiseau, A. (2009). Size and shape effects on the order-disorder phase transition in CoPt nanoparticles. *Nat. Mater.*, 8 (12), 940-946.
- (95) Jacobs, K.; Zaziski, D.; Scher, E. C.; Herhold, A. B.; Paul Alivisatos, A. (2001). Activation volumes for solid-solid transformations in nanocrystals. *Science*, 293 (5536), 1803-1806.
- (96) Zheng, H.; Rivest, J. B.; Miller, T. A.; Sadtler, B.; Lindenberg, A.; Toney, M. F.; Wang, L. W.; Kisielowski, C.; Alivisatos, A. P. (2011). Observation of transient structural-transformation dynamics in a Cu₂S nanorod. *Science*, 333 (6039), 206-209.
- (97) Son, D. H.; Hughes, S. M.; Yin, Y.; Paul Alivisatos, A. (2004). Cation exchange reactions in ionic nanocrystals. *Science*, 306 (5698), 1009-1012.
- (98) Zhang, J.; Tang, Y.; Lee, K.; Ouyang, M. (2010). Nonepitaxial growth of hybrid core-shell nanostructures with large lattice mismatches. *Science*, 327 (5973), 1634-1638.
- (99) White, S. L.; Smith, J. G.; Behl, M.; Jain, P. K. (2013). Co-operativity in a nanocrystalline solid-state transition. *Nat. Commun.*, 4, 2933.
- (100) Gao, Y.; Peng, X. (2014). Crystal structure control of CdSe nanocrystals in growth and nucleation: dominating effects of surface versus interior structure. *J. Am. Chem. Soc.*, 136 (18), 6724-6732.
- (101) Zhang, H.; Gilbert, B.; Huang, F.; Banfield, J. F. (2003). Water-driven structure transformation in nanoparticles at room temperature. *Nature*, 424 (6952), 1025-1029.
- (102) Bauer, R.; Jägle, E. A.; Baumann, W.; Mittemeijer, E. J. (2010). Kinetics of the allotropic hcp-fcc phase transformation in cobalt. *Phil. Mag.*, 91 (3), 437-457.
- (103) Tolédano, P.; Krexner, G.; Prem, M.; Weber, H. P.; Dmitriev, V. P. (2001). Theory of the martensitic transformation in cobalt. *Phys. Rev. B*, 64 (14), 144104.
- (104) Blaschko, O.; Krexner, G.; Pleschiutchnig, J.; Ernst, G.; Hitzenberger, C.; Karnthaler, H. P.; Korner, A. (1988). Coherent modulated structure during the Martensitic hcp-fcc phase transition in Co and in a CoNi alloy. *Phys. Rev. Lett.*, 60 (26), 2800-2803.

- (105) Kondo, Y.; Takayanagi, K. (1997). Gold nanobridge stabilized by surface structure. *Phys. Rev. Lett.*, 79 (18), 3455-3458.
- (106) McHale, J. M.; Auroux, A.; Perrotta, A. J.; Navrotsky, A. (1997). Surface energies and thermodynamic phase stability in nanocrystalline aluminas. *Science*, 277 (5327), 788-791.
- (107) Vericat, C.; Vela, M. E.; Benitez, G.; Carro, P.; Salvarezza, R. C. (2010). Self-assembled monolayers of thiols and dithiols on gold: new challenges for a well-known system. *Chem. Soc. Rev.*, 39 (5), 1805-1834.
- (108) Dubois, L. H.; Zegarski, B. R.; Nuzzo, R. G. (1993). Molecular ordering of organosulfur compounds on Au(111) and Au(100): Adsorption from solution and in ultrahigh vacuum. *J. Chem. Phys.*, 98 (1), 678.
- (109) Jefferson, D. A.; Harris, P. J. F. (1988). Direct imaging of an adsorbed layer by high-resolution electron microscopy. *Nature*, 332 (6165), 617-620.
- (110) Warburton, D. R.; Wincott, P. L.; Thornton, G.; Quinn, F. M.; Norman, D. (1989). Incorporation of sulphur into the (111) surface of nickel? *Surf. Sci.*, 211-212, 71-81.
- (111) Titmuss, S.; Wander, A.; King, D. A. (1996). Reconstruction of clean and adsorbate-covered metal surfaces. *Chem. Rev.*, 96 (4), 1291-1306.
- (112) Poirier, G. E. (1997). Characterization of organosulfur molecular monolayers on Au(111) using scanning tunneling microscopy. *Chem. Rev.*, 97 (4), 1117-1128.
- (113) Hakkinen, H. (2012). The gold-sulfur interface at the nanoscale. *Nat. Chem.*, 4 (6), 443-455.
- (114) Maksymovych, P.; Voznyy, O.; Dougherty, D. B.; Sorescu, D. C.; Yates Jr, J. T. (2010). Gold adatom as a key structural component in self-assembled monolayers of organosulfur molecules on Au(111). *Prog. Surf. Sci.*, 85 (5-8), 206-240.
- (115) McCarroll, J. J.; Edmonds, T.; Pitkethly, R. C. (1969). Interpretation of a complex low energy electron diffraction pattern: carbonaceous and sulphur-containing structures on Ni(111). *Nature*, 223 (5212), 1260-1262.

- (116) Harris, P. J. F. (1986). Sulphur-induced faceting of platinum catalyst particles. *Nature*, 323 (6091), 792-794.
- (117) Limpijumnong, S.; Lambrecht, W. R. L. (2001). Theoretical study of the relative stability of wurtzite and rocksalt phases in MgO and GaN. *Phys. Rev. B*, 63 (10), 104103.
- (118) Grünwald, M.; Rabani, E.; Dellago, C. (2006). Mechanisms of the wurtzite to rocksalt transformation in CdSe nanocrystals. *Phys. Rev. Lett.*, 96 (25), 255701.
- (119) Chen, C.-C.; Herhold, A. B.; Johnson, C. S.; Alivisatos, A. P. (1997). Size dependence of structural metastability in semiconductor nanocrystals. *Science*, 276 (5311), 398-401.
- (120) Millstone, J. E.; Park, S.; Shuford, K. L.; Qin, L.; Schatz, G. C.; Mirkin, C. A. (2005). Observation of a quadrupole plasmon mode for a colloidal solution of gold nanoprisms. *J. Am. Chem. Soc.*, 127 (15), 5312-5313.
- (121) Jin, R.; Charles Cao, Y.; Hao, E.; Metraux, G. S.; Schatz, G. C.; Mirkin, C. A. (2003). Controlling anisotropic nanoparticle growth through plasmon excitation. *Nature*, 425 (6957), 487-490.
- (122) Bosman, M.; Ye, E.; Tan, S. F.; Nijhuis, C. A.; Yang, J. K. W.; Marty, R.; Mlayah, A.; Arbouet, A.; Girard, C.; Han, M.-Y. (2013). Surface plasmon damping quantified with an electron nanoprobe. *Sci. Rep.*, 3, 1312.
- (123) Kelly, K. L.; Coronado, E.; Zhao, L. L.; Schatz, G. C. (2002). The optical properties of metal nanoparticles: the influence of size, shape, and dielectric environment. *J. Phy. Chem. B*, 107 (3), 668-677.
- (124) Jin, R.; Cao, Y.; Mirkin, C. A.; Kelly, K. L.; Schatz, G. C.; Zheng, J. G. (2001). Photoinduced conversion of silver nanospheres to nanoprisms. *Science*, 294 (5548), 1901-1903.
- (125) Turkevich, J.; Stevenson, P. C.; Hillier, J. (1951). A study of the nucleation and growth processes in the synthesis of colloidal gold. *Discuss. Faraday Soc.*, 11, 55-75.
- (126) Halas, N. J.; Lal, S.; Chang, W.-S.; Link, S.; Nordlander, P. (2011). Plasmons in strongly coupled metallic nanostructures. *Chem. Rev.*, 111 (6), 3913-3961.

- (127) Jones, M. R.; Osberg, K. D.; Macfarlane, R. J.; Langille, M. R.; Mirkin, C. A. (2011). Templated techniques for the synthesis and assembly of plasmonic nanostructures. *Chem. Rev.*, 111 (6), 3736-3827.
- (128) Wu, J.; Li, P.; Pan, Y.-T.; Warren, S.; Yin, X.; Yang, H. (2012). Surface lattice-engineered bimetallic nanoparticles and their catalytic properties. *Chem. Soc. Rev.*, 41 (24), 8066-8074.
- (129) Gu, J.; Zhang, Y.-W.; Tao, F. (2012). Shape control of bimetallic nanocatalysts through well-designed colloidal chemistry approaches. *Chem. Soc. Rev.*, 41 (24), 8050-8065.
- (130) Liu, X.; Wang, D.; Li, Y. (2012). Synthesis and catalytic properties of bimetallic nanomaterials with various architectures. *Nano Today*, 7 (5), 448-466.
- (131) Gao, C.; Lu, Z.; Liu, Y.; Zhang, Q.; Chi, M.; Cheng, Q.; Yin, Y. (2012). Highly stable silver nanoplates for surface plasmon resonance biosensing. *Angew. Chem. Int. Ed.*, 51 (23), 5629-5633.
- (132) Fan, F.-R.; Liu, D.-Y.; Wu, Y.-F.; Duan, S.; Xie, Z.-X.; Jiang, Z.-Y.; Tian, Z.-Q. (2008). Epitaxial growth of heterogeneous metal nanocrystals: from gold nano-octahedra to palladium and silver nanocubes. *J. Am. Chem. Soc.*, 130 (22), 6949-6951.
- (133) Zeng, J.; Zhu, C.; Tao, J.; Jin, M.; Zhang, H.; Li, Z. Y.; Zhu, Y.; Xia, Y. (2012). Controlling the nucleation and growth of silver on palladium nanocubes by manipulating the reaction kinetics. *Angew. Chem. Int. Ed.*, 51 (10), 2354-2358.
- (134) Camargo, P. H. C.; Xiong, Y.; Ji, L.; Zuo, J. M.; Xia, Y. (2007). Facile synthesis of tadpole-like nanostructures consisting of Au heads and Pd tails. *J. Am. Chem. Soc.*, 129 (50), 15452-15453.
- (135) Zhang, J.; Tang, Y.; Weng, L.; Ouyang, M. (2009). Versatile strategy for precisely tailored core@shell nanostructures with single shell layer accuracy: the case of metallic shell. *Nano Lett.*, 9 (12), 4061-4065.
- (136) Langille, M. R.; Zhang, J.; Personick, M. L.; Li, S.; Mirkin, C. A. (2012). Stepwise evolution of spherical seeds into 20-fold twinned icosahedra. *Science*, 337 (6097), 954-957.

- (137) Lim, B.; Wang, J.; Camargo, P. H. C.; Jiang, M.; Kim, M. J.; Xia, Y. (2008). Facile synthesis of bimetallic nanoplates consisting of Pd cores and Pt shells through seeded epitaxial growth. *Nano Lett.*, 8 (8), 2535-2540.
- (138) Hong, J. W.; Kim, D.; Lee, Y. W.; Kim, M.; Kang, S. W.; Han, S. W. (2011). Atomic-distribution-dependent electrocatalytic activity of Au-Pd bimetallic nanocrystals. *Angew. Chem. Int. Ed.*, 50 (38), 8876-8880.
- (139) Hsieh, Y.-C.; Zhang, Y.; Su, D.; Volkov, V.; Si, R.; Wu, L.; Zhu, Y.; An, W.; Liu, P.; He, P.; Ye, S.; Adzic, R. R.; Wang, J. X. (2013). Ordered bilayer ruthenium-platinum core-shell nanoparticles as carbon monoxide-tolerant fuel cell catalysts. *Nat. Commun.*, 4, 2466.
- (140) Kim, Y.-H.; Jun, Y.-w.; Jun, B.-H.; Lee, S.-M.; Cheon, J. (2002). Sterically induced shape and crystalline phase control of GaP nanocrystals. *J. Am. Chem. Soc.*, 124 (46), 13656-13657.
- (141) Wang, C.; Tian, W.; Ding, Y.; Ma, Y.-q.; Wang, Z. L.; Markovic, N. M.; Stamenkovic, V. R.; Daimon, H.; Sun, S. (2010). Rational synthesis of heterostructured nanoparticles with morphology control. *J. Am. Chem. Soc.*, 132 (18), 6524-6529.
- (142) Liu, Y.; Wang, C.; Wei, Y.; Zhu, L.; Li, D.; Jiang, J. S.; Markovic, N. M.; Stamenkovic, V. R.; Sun, S. (2011). Surfactant-induced postsynthetic modulation of Pd nanoparticle crystallinity. *Nano Lett.*, 11 (4), 1614-1617.
- (143) Sun, X.; Dong, S.; Wang, E. (2004). Large-scale synthesis of micrometer-scale single-crystalline Au plates of nanometer thickness by a wet-chemical route. *Angew. Chem. Int. Ed.*, 116 (46), 6520-6523.
- (144) Tian, W.; Sun, H. P.; Pan, X. Q.; Yu, J. H.; Yeadon, M.; Boothroyd, C. B.; Feng, Y. P.; Lukaszew, R. A.; Clarke, R. (2005). Hexagonal close-packed Ni nanostructures grown on the (001) surface of MgO. *Appl. Phys. Lett.*, 86 (13), 131915.
- (145) Huang, X.; Li, H.; Li, S.; Wu, S.; Boey, F.; Ma, J.; Zhang, H. (2011). Synthesis of gold square-like plates from ultrathin gold square sheets: the evolution of structure phase and shape. *Angew. Chem. Int. Ed.*, 50 (51), 12245-12248.
- (146) McHale, J. M. (1997). Surface energies and thermodynamic phase stability in nanocrystalline aluminas. *Science*, 277 (5327), 788-791.

- (147) Zeches, R. J.; Rossell, M. D.; Zhang, J. X.; Hatt, A. J.; He, Q.; Yang, C. H.; Kumar, A.; Wang, C. H.; Melville, A.; Adamo, C.; Sheng, G.; Chu, Y. H.; Ihlefeld, J. F.; Erni, R.; Ederer, C.; Gopalan, V.; Chen, L. Q.; Schlom, D. G.; Spaldin, N. A.; Martin, L. W.; Ramesh, R. (2009). A strain-driven morphotropic phase boundary in BiFeO₃. *Science*, 326 (5955), 977-980.
- (148) Ithurria, S.; Guyot-Sionnest, P.; Mahler, B.; Dubertret, B. (2007). Mn²⁺ as a radial pressure gauge in colloidal core/shell nanocrystals. *Phys. Rev. Lett.*, 99 (26), 265501.
- (149) Skriver, H. L. (1985). Crystal structure from one-electron theory. *Phys. Rev. B*, 31 (4), 1909-1923.
- (150) Voiry, D.; Yamaguchi, H.; Li, J.; Silva, R.; Alves, D. C. B.; Fujita, T.; Chen, M.; Asefa, T.; Shenoy, V. B.; Eda, G.; Chhowalla, M. (2013). Enhanced catalytic activity in strained chemically exfoliated WS₂ nanosheets for hydrogen evolution. *Nat. Mater.*, 12 (9), 850-855.
- (151) Zhang, J.; Xu, Q.; Feng, Z.; Li, M.; Li, C. (2008). Importance of the relationship between surface phases and photocatalytic activity of TiO₂. *Angew. Chem. Int. Ed.*, 47 (9), 1766-1769.
- (152) Caroff, P.; Dick, K. A.; Johansson, J.; Messing, M. E.; Deppert, K.; Samuelson, L. (2009). Controlled polytypic and twin-plane superlattices in III-V nanowires. *Nat. Nanotech.*, 4 (1), 50-55.
- (153) Park, C. H.; Cheong, B.-H.; Lee, K.-H.; Chang, K. J. (1994). Structural and electronic properties of cubic, 2H, 4H, and 6H SiC. *Phys. Rev. B*, 49 (7), 4485-4493.
- (154) Navrotsky, A.; Mazeina, L.; Majzlan, J. (2008). Size-driven structural and thermodynamic complexity in iron oxides. *Science*, 319 (5870), 1635-1638.
- (155) Wang, Z.; Daemen, L. L.; Zhao, Y.; Zha, C. S.; Downs, R. T.; Wang, X.; Wang, Z. L.; Hemley, R. J. (2005). Morphology-tuned wurtzite-type ZnS nanobelts. *Nat. Mater.*, 4 (12), 922-927.
- (156) Nam, K. M.; Shim, J. H.; Han, D.-W.; Kwon, H. S.; Kang, Y.-M.; Li, Y.; Song, H.; Seo, W. S.; Park, J. T. (2010). Syntheses and characterization of wurtzite CoO, rocksalt CoO, and spinel Co₃O₄ nanocrystals: their interconversion and tuning of phase and morphology. *Chem. Mater.*, 22 (15), 4446-4454.

- (157) Dreaden, E. C.; Alkilany, A. M.; Huang, X.; Murphy, C. J.; El-Sayed, M. A. (2012). The golden age: gold nanoparticles for biomedicine. *Chem. Soc. Rev.*, 41 (7), 2740-2779.
- (158) Masuda, H.; Fukuda, K. (1995). Ordered metal nanohole arrays made by a two-step replication of honeycomb structures of anodic alumina. *Science*, 268 (5216), 1466-1468.
- (159) Jana, N. R.; Gearheart, L.; Murphy, C. J. (2001). Wet chemical synthesis of high aspect ratio cylindrical gold nanorods. *J. Phys. Chem. B*, 105 (19), 4065-4067.
- (160) Nikoobakht, B.; El-Sayed, M. A. (2003). Preparation and growth mechanism of gold nanorods (NRs) using seed-mediated growth method. *Chem. Mater.*, 15 (10), 1957-1962.
- (161) Lu, X.; Yavuz, M. S.; Tuan, H.-Y.; Korgel, B. A.; Xia, Y. (2008). Ultrathin gold nanowires can be obtained by reducing polymeric strands of oleylamine–AuCl complexes formed via aurophilic interaction. *J. Am. Chem. Soc.*, 130 (28), 8900-8901.
- (162) Wang, C.; Hu, Y.; Lieber, C. M.; Sun, S. (2008). Ultrathin Au nanowires and their transport properties. *J. Am. Chem. Soc.*, 130 (28), 8902-8903.
- (163) Huo, Z.; Tsung, C.-k.; Huang, W.; Zhang, X.; Yang, P. (2008). Sub-two nanometer single crystal Au nanowires. *Nano Lett.*, 8 (7), 2041-2044.
- (164) Shankar, S. S.; Rai, A.; Ankamwar, B.; Singh, A.; Ahmad, A.; Sastry, M. (2004). Biological synthesis of triangular gold nanoprisms. *Nat. Mater.*, 3 (7), 482-488.
- (165) Zhang, J.; Du, J.; Han, B.; Liu, Z.; Jiang, T.; Zhang, Z. (2006). Sonochemical formation of single-crystalline gold nanobelts. *Angew. Chem. Int. Ed.*, 118 (7), 1134-1137.
- (166) Kim, F.; Connor, S.; Song, H.; Kuykendall, T.; Yang, P. (2004). Platonic gold nanocrystals. *Angew. Chem. Int. Ed.*, 116 (28), 3759-3763.
- (167) Sebastian, M. T. (1987). X-ray diffraction effects from 2H crystals undergoing transformation to the 4H structure by the shear mechanism. *Cryst. Res. Technol.*, 22 (3), 441-447.

(168) Palosz, B.; Steurer, W.; Schulz, H. (1990). The structure of PbI_2 polytypes 2H and 4H: a study of the 2H-4H transition. *J. Phys.: Condens. Matter*, 2 (24), 5285.

(169) Hövel, M.; Gompf, B.; Dressel, M. (2010). Dielectric properties of ultrathin metal films around the percolation threshold. *Phys. Rev. B*, 81 (3), 035402.

LIST OF PUBLICATIONS

1. **Fan, Z.**, Bosman M., Huang X., Huang D., Yu Y., Ong K. P., Akimov Y. A., Wu L., Li B., Wu J., Huang Y., Liu Q., Png C. E., Gan C. L., Yang P., Zhang H. (2015). Stabilization of 4H hexagonal phase in gold nanoribbons. *Nature Commun.*, 6, 7684.
2. **Fan, Z.**, Huang, X., Han, Y., Bosman, M., Wang, Q., Zhu, Y., Liu, Q., Li, B., Zeng, Z., Wu, J., Shi, W., Li, S., Gan, C. L., Zhang, H. (2015). Surface modification-induced phase transformation of hexagonal close-packed gold square sheets. *Nature Commun.*, 6, 6571.
3. **Fan, Z.**, Zhu, Y., Huang, X., Han, Y., Wang, Q., Liu, Q., Huang, Y., Gan, C. L., Zhang, H. (2015). Synthesis of ultrathin face-centered-cubic Au@Pt and Au@Pd core-shell nanoplates from hexagonal-close-packed Au square sheets. *Angew. Chem. Int. Ed.*, 54 (19), 5672-7676.
4. **Fan, Z.**, Huang, X., Tan, C., Zhang, H. (2015). Thin metal nanostructures: synthesis, properties and applications. *Chem. Sci.*, 6 (1), 95-111.
5. Huang, X., Zeng, Z., Bao, S., Wang, M., Qi, X., **Fan, Z.**, Zhang, H. (2013). Solution-phase epitaxial growth of noble metal nanostructures on dispersible single-layer molybdenum disulfide nanosheets. *Nature Commun.*, 4, 1444.
6. Huang, X., Zeng, Z., **Fan, Z.**, Liu, J., Zhang, H. (2012). Graphene-based electrodes. *Adv. Mater.*, 24 (45), 5979-6004.
7. Xia, X., Chao, D., **Fan, Z.**, Guan, C., Cao, X., Zhang, H., Fan, H. J. (2014). A new type of porous graphite foams and their integrated composites with oxide/polymer core/shell nanowires for supercapacitors: structural design, fabrication, and full supercapacitor demonstrations. *Nano Lett.*, 14 (3), 1651-1658.
8. Hong, X., Tan, C., Liu, J., Yang, J., Wu, X., **Fan, Z.**, Luo, Z., Chen, J., Zhang, X., Chen, B., Zhang, H. (2015). AuAg nanosheets assembled from ultrathin AuAg nanowires. *J. Am. Chem. Soc.*, 137 (4), 1444-1447.
9. Chen, J., Wu, X.-J., Yin, L., Li, B., Hong, X., **Fan, Z.**, Chen, B., Xue, C., Zhang, H. (2015). One-pot synthesis of CdS nanocrystals hybridized with single-layer transition-metal dichalcogenide nanosheets for efficient photocatalytic hydrogen evolution. *Angew. Chem. Int. Ed.*, 127 (4), 1226-1230.
10. Chao, D., Xia, X., Liu, J., **Fan, Z.**, Ng, C. F., Lin, J., Zhang, H., Shen, Z. X., Fan, H. J. (2014). A V₂O₅/conductive-polymer core/shell nanobelt array on three-dimensional graphite foam: a high-rate, ultrastable, and

- freestanding cathode for lithium-ion batteries. *Adv. Mater.*, 26 (33), 5794-5800.
11. Guan, C., Wang, X., Zhang, Q., **Fan, Z.**, Zhang, H., Fan, H. J. (2014). Highly stable and reversible lithium storage in SnO₂ nanowires surface coated with a uniform hollow shell by atomic layer deposition. *Nano Lett.*, 14 (8), 4852-4858.
 12. Cao, X., Zheng, B., Shi, W., Yang, J., **Fan, Z.**, Rui, X., Chen, B., Yan, Q., Zhang, H. (2015). Reduced graphene oxide-wrapped MoO₃ composites prepared by using metal-organic frameworks as precursor for all-solid-state flexible supercapacitors. *Adv. Mater.*, 27 (32), 4695-4701.
 13. Xia, X., Zhang, Y., **Fan, Z.**, Chao, D., Xiong, Q., Tu, J., Zhang, H., Fan, H. J. (2015). Novel metal@carbon spheres core-shell arrays by controlled self-assembly of carbon nanospheres: a stable and flexible supercapacitor electrode. *Adv. Energy Mater.*, 5 (6), 1401709.
 14. Jiang, J., Zhu, J., Ai, W., **Fan, Z.**, Shen, X., Zou, C., Liu, J., Zhang, H., Yu, T. (2014). Evolution of disposable bamboo chopsticks into uniform carbon fibers: a smart strategy to fabricate sustainable anodes for Li-ion batteries. *Energy Environ. Sci.*, 7 (8), 2670-2679.
 15. Ai, W., Jiang, J., Zhu, J., **Fan, Z.**, Wang, Y., Zhang, H., Huang, W., Yu, T. (2015). Supramolecular polymerization promoted in situ fabrication of nitrogen-doped porous graphene sheets as anode materials for li-ion batteries. *Adv. Energy Mater.*, 5 (15), 1500559.
 16. Hong, X., Yin, Z., **Fan, Z.**, Tay, Y.-Y., Chen, J., Du, Y., Xue, C., Chen, H., Zhang, H. (2014). Periodic AuAg-Ag₂S heterostructured nanowires. *Small*, 10 (3), 479-482.
 17. Guan, C., Liu, J., Wang, Y., Mao, L., **Fan, Z.**, Shen, Z., Zhang, H., Wang, J. (2015). Iron oxide-decorated carbon for supercapacitor anodes with ultrahigh energy density and outstanding cycling stability. *ACS Nano*, 9 (5), 5198-5207.
 18. Xia, X., Zhang, Y., Chao, D., Xiong, Q., **Fan, Z.**, Tong, X., Tu, J., Zhang, H., Fan, H. J. (2015). Tubular TiC fibre nanostructures as supercapacitor electrode material with stable cycling life and wide-temperature performance. *Energy Environ. Sci.*, 8 (5), 1559-1568.
 19. Zhu, C., Chao, D., Sun, J., Bacho, I. M., **Fan, Z.**, Ng, C. F., Xia, X., Huang, H., Zhang, H., Shen, Z. X., Ding, G., Fan, H. J. (2015). Enhanced lithium storage performance of CuO nanowires by coating of graphene quantum dots. *Adv. Mater. Interfaces*, 2 (2), 1400499.
 20. Xia, X., Chao, D., Ng, C. F., Lin, J., **Fan, Z.**, Zhang, H., Shen, Z. X., Fan, H. J. (2015). VO₂ nanoflake arrays for supercapacitor and Li-ion battery electrodes: performance enhancement by hydrogen molybdenum bronze as an efficient shell material. *Mater. Horiz.*, 2 (2), 237-244.

21. Xu, L., Luo, Z., **Fan, Z.**, Yu, S., Chen, J., Liao, Y., Xue, C. (2015). Controllable galvanic synthesis of triangular Ag–Pd alloy nanoframes for efficient electrocatalytic methanol oxidation. *Chem. Eur. J.*, 21 (24), 8691-8695.
22. He, J., Wang, Y., **Fan, Z.**, Lam, Z., Zhang, H., Liu, B., Chen, H. (2015). Substrate-bound growth of Au-Pd diblock nanowire and hybrid nanorod-plate. *Nanoscale*, 7 (17), 8115-8121.
23. Ai, W., Luo, Z., Jiang, J., Zhu, J., Du, Z., **Fan, Z.**, Xie, L., Zhang, H., Huang, W., Yu, T. (2014). Nitrogen and sulfur codoped graphene: multifunctional electrode materials for high-performance Li-ion batteries and oxygen reduction reaction. *Adv. Mater.*, 26 (35), 6186-6192.
24. Hong, X., Liu, J., Zheng, B., Huang, X., Zhang, X., Tan, C., Chen, J., **Fan, Z.**, Zhang, H. (2014). A universal method for preparation of noble metal nanoparticle-decorated transition metal dichalcogenide nanobelts. *Adv. Mater.*, 26 (36), 6250-6254.
25. Huang, X., Zheng, B., Liu, Z., Tan, C., Liu, J., Chen, B., Li, H., Chen, J., Zhang, X., **Fan, Z.**, Zhang, W., Guo, Z., Huo, F., Yang, Y., Xie, L.-H., Huang, W., Zhang, H. (2014). Coating two-dimensional nanomaterials with metal–organic frameworks. *ACS Nano*, 8 (8), 8695-8701.
26. Zhu, J., Jiang, J., Sun, Z., Luo, J., **Fan, Z.**, Huang, X., Zhang, H., Yu, T. (2014). 3D carbon/cobalt-nickel mixed-oxide hybrid nanostructured arrays for asymmetric supercapacitors. *Small*, 10 (14), 2937-2945.
27. Zhu, J., Jiang, J., Ai, W., **Fan, Z.**, Huang, X., Zhang, H., Yu, T. (2014). Encapsulation of nanoscale metal oxides into an ultra-thin Ni matrix for superior Li-ion batteries: a versatile strategy. *Nanoscale*, 6 (21), 12990-13000.
28. Zhu, C., Xia, X., Liu, J., **Fan, Z.**, Chao, D., Zhang, H., Fan, H. J. (2014). TiO₂ nanotube@SnO₂ nanoflake core–branch arrays for lithium-ion battery anode. *Nano Energy*, 4, 105-112.
29. Xu, L., Yin, Z., Cao, S.-W., **Fan, Z.**, Zhang, X., Zhang, H., Xue, C. (2014). Rational synthesis of triangular Au–Ag₂S hybrid nanoframes with effective photoresponses. *Chem. Eur. J.*, 20 (10), 2742-2745.
30. Xu, L., Luo, Z., **Fan, Z.**, Zhang, X., Tan, C., Li, H., Zhang, H., Xue, C. (2014). Triangular Ag-Pd alloy nanoprisms: rational synthesis with high-efficiency for electrocatalytic oxygen reduction. *Nanoscale*, 6 (20), 11738-11743.
31. Ai, W., Du, Z., **Fan, Z.**, Jiang, J., Wang, Y., Zhang, H., Xie, L., Huang, W., Yu, T. (2014). Chemically engineered graphene oxide as high performance cathode materials for Li-ion batteries. *Carbon*, 76, 148-154.
32. Zhou, W., Yin, Z., Du, Y., Huang, X., Zeng, Z., **Fan, Z.**, Liu, H., Wang, J., Zhang, H. (2013). Synthesis of few-layer MoS₂ nanosheet-coated TiO₂

- nanobelt heterostructures for enhanced photocatalytic activities. *Small*, 9 (1), 140-147.
33. Zeng, Z., Sun, T., Zhu, J., Huang, X., Yin, Z., Lu, G., **Fan, Z.**, Yan, Q., Hng, H. H., Zhang, H. (2012). An effective method for the fabrication of few-layer-thick inorganic nanosheets. *Angew. Chem. Int. Ed.*, 51 (36), 9052-9056.